Advancements in Biosensing Technology: Novel Strategies and Devices for Sensitive and Specific Detection of Relevant Biomolecules in Clinical Diagnostics and Personalized Medicine

by

Anil BOZDOGAN MSc, BSc

Doctoral Dissertation

Submitted to Faculty of Biology

Johannes Gutenberg University of Mainz

In Partial Fulfillment of the Requirements

For Doctor of Philosophy (PhD)

May 2023

Affidavits

I solemnly affirm that the creation of this thesis has been entirely my own effort, with the exception of permissible aid. The intellectual content found within is predominantly my work, unless explicitly mentioned otherwise. Ideas adapted either verbatim or conceptually from undisclosed resources or acknowledged publications have been properly referenced, with specific citations included. Any intellectual contribution from my peers is clearly acknowledged in the authorship section of the published papers.

Additionally, I confirm that this thesis has never been presented, wholly or partially, in its present form or any closely resembling version, to any other academic institution as part of the criteria for a scholastic degree.

Finally, I assert my familiarity with the tenets of Scientific Integrity and the guidelines for Good Scientific Practice, and pledge that this work strictly adheres to those principles and guidelines.

Vienna, June 2023

Anil Bozdogan

Abstract

Biosensors play a crucial role in various fields, including healthcare, environmental monitoring, and food safety, by providing rapid, accurate, and sensitive detection of target analytes. Advancements in biosensing technology have the potential to revolutionize diagnostics and personalized medicine, enabling better disease management and improved patient outcomes. This thesis explores novel strategies and devices for the development of highly sensitive and specific biosensors for the detection of essential biomolecules, such as cardiac biomarkers and protein isoforms.

The work includes an optimized deposition protocol for reduced graphene oxide (rGO) on silica-based substrates, enhancing the fabrication of electronic devices for various applications. A sensitive troponin cTnI immunoassay with a single monoclonal antibody and Surface Plasmon Fluorescence Spectroscopy (SPFS) detection is developed, enabling the analysis of cTnI at clinically relevant concentrations. The thesis also investigates the advantages of focused polyclonal aptamer libraries for increased performance and versatility in diagnostics and sensor technology. By functionalizing an rGO-FET device, selective discrimination between RBP4 isoforms at physiologically relevant concentrations is achieved, opening avenues for novel diagnostic markers. Finally, the thesis highlights the importance of considering additional factors in the development of cTnI biosensors to meet evolving clinical requirements. In conclusion, this thesis presents significant advancements in biosensing devices and strategies for the sensitive and specific detection of critical biomolecules, with promising implications for clinical diagnostics and personalized medicine.

Kurzfassung

Biosensoren spielen eine entscheidende Rolle in verschiedenen Bereichen, einschließlich Gesundheitswesen, Umweltüberwachung und Lebensmittelsicherheit, indem sie eine schnelle, genaue und empfindliche Erkennung von Zielanalyten ermöglichen. Fortschritte in der Biosensor-Technologie haben das Potenzial, Diagnostik und personalisierte Medizin zu revolutionieren und so eine bessere Krankheitsmanagement und verbesserte Patientenergebnisse zu ermöglichen. Diese Arbeit untersucht neue Strategien und Geräte für die Entwicklung von hochsensitiven und spezifischen Biosensoren für die Erkennung von essentiellen Biomolekülen, wie z. B. kardiale Biomarker und Protein-Isoformen.

Die Arbeit beinhaltet ein optimiertes Abscheidungsprotokoll für reduziertes Graphenoxid (rGO) auf silikabasierten Substraten, das die Herstellung von elektronischen Geräten für verschiedene Anwendungen verbessert. Ein empfindlicher Troponin-cTnI-Immunoassay mit einem einzigen monoklonalen Antikörper und Surface Plasmon Fluorescence Spectroscopy (SPFS) -Erkennung wird entwickelt, um die Analyse von cTnI in klinisch relevanten Konzentrationen zu ermöglichen. Die Arbeit untersucht auch die Vorteile von fokussierten polyklonalen Aptamerbibliotheken für eine erhöhte Leistung und Vielseitigkeit in der Diagnostik und Sensortechnologie. Durch die Funktionalisierung eines rGO-FET-Geräts wird eine selektive Diskriminierung zwischen RBP4-Isoformen bei physiologisch relevanten Konzentrationen erreicht, was neue Wege für neuartige diagnostische Marker eröffnet. Schließlich betont die Arbeit die Bedeutung der Berücksichtigung zusätzlicher Faktoren bei der Entwicklung von cTnI-Biosensoren, um sich weiter entwickelnde klinische Anforderungen zu erfüllen. Abschließend präsentiert diese Arbeit bedeutende Fortschritte in Biosensor-Geräten und -Strategien für die empfindliche und spezifische Erkennung von kritischen Biomolekülen, mit vielversprechenden Auswirkungen auf die klinische Diagnostik und personalisierte Medizin.

Figures

Table of Contents

1. Introduction

What is a sensor?

Sensors have emerged as one of the most significant technological advancements in recent times, playing a critical role in diverse fields and industries (*1*). These input devices convert various physical parameters into electrical signals, enabling us to measure and monitor an array of aspects in our surrounding environment (*2*).

The roots of sensor technology can be traced back to Warren S. Johnson, who invented the electric thermostat in 1883, a pioneering achievement that laid the foundation for modern sensors (*3*). Another notable breakthrough in the field of sensors occurred in the 1950s when Samuel Bagno created the first motion sensor for an alarm system (*4*). Bagno's innovative device utilized ultrasonic frequencies and the Doppler Effect, significantly expanding the range of applications for sensor technology.

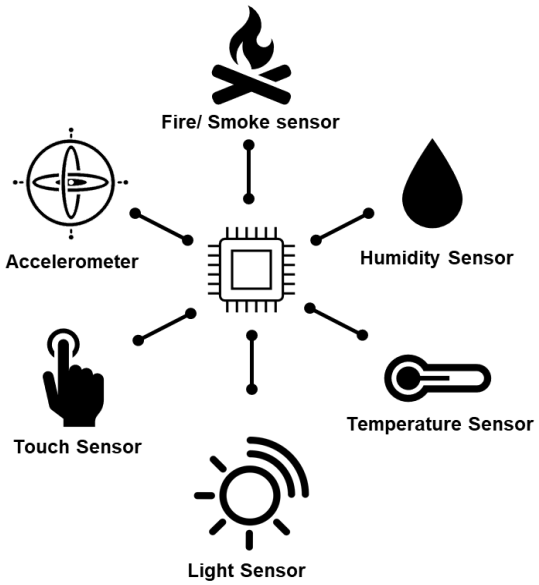

Figure 1-1 Schematic representation of Sensor types

Sensors are capable of detecting changes in a wide variety of physical parameters, including light (*5*), motion (*6*), gas (*7*), alcohol (*8*), and heart rate (*9*). These changes are converted into electrical signals, which can subsequently be used to monitor, control, and manipulate various systems. As a result, sensors provide valuable information about the physical world, offering insights that can enhance our understanding and management of the environment and the devices we use daily (*10*).

2. Biosensors

Biosensors are advanced analytical tools that enable the accurate detection of target molecules through the generation of electrical signals. They consist of three primary components: a recognition element that selectively binds to the target molecule, a detection probe that facilitates this interaction, and a transducer that converts the presence of the target molecule into an electrical signal. Biosensors have become indispensable in various industries, such as food safety, clinical and medical applications, process control, bioreactors, pharmaceutical production, wastewater control, and military defence, due to their ability to offer highly sensitive and specific detection of target molecules (*11–17*)

A biosensor is a system (Figure 2.1) that integrates biological sensing materials with a transducer to transform biological, chemical, or biochemical signals into quantifiable electrical signals (*18*). Biological sensing materials can vary from enzymes and antibodies to whole cells and tissues, while transducers can employ diverse technologies like electrochemistry (*15*), optical systems (*19*), chemical and biological luminescence (*20*), fluorescence, fibre optics (*21*), piezoelectricity, and magnetic principles (*22*). The adaptability of biosensors renders them invaluable tools for a broad array of applications across various fields. The combination of specific biological sensing materials with accurate transduction mechanisms allows biosensors to deliver highly sensitive and specific detection of target molecules. (*23*)

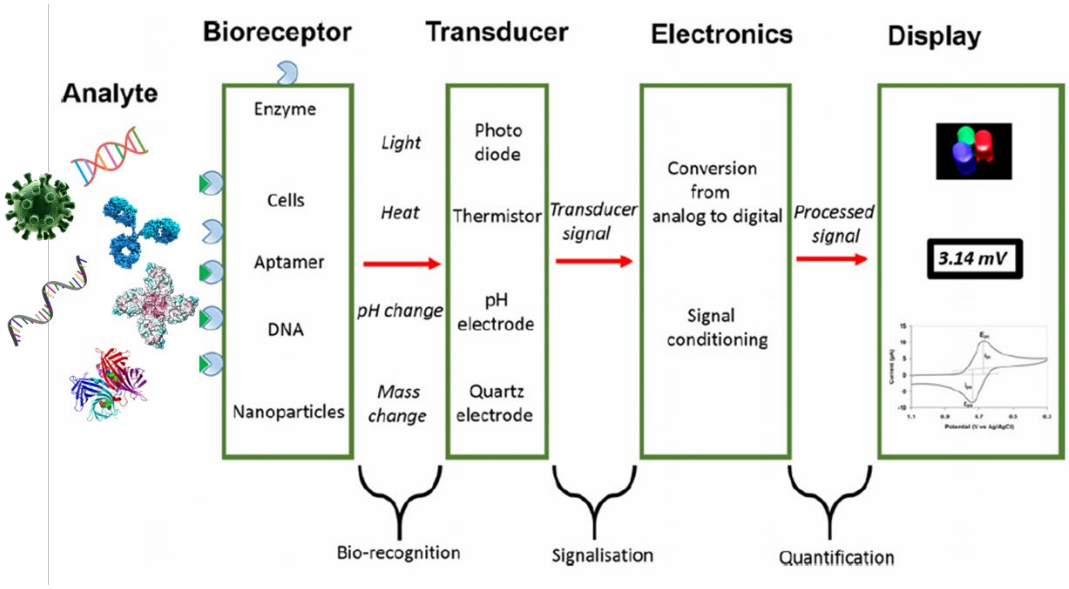

Figure 2-1 The mechanism of biosensors

The origins of biosensor technology date back to 1906 when Cremer first examined the correlation between electric potential and acid concentration in a liquid medium Subsequent researchers such as Sorensen, Hughes, Griffin, and Nelson advanced the field by measuring pH using electrodes, incorporating enzymes into their sensors, and uncovering new biosensors for a variety of applications (*24*, *25*). In 1956, Clark revolutionized the field by devising the first oxygen-detecting biosensor, known as the Clark electrode (*26*). his breakthrough was followed by Clark's development of the amperometric enzyme electrode for glucose detection and Guilbault and Montalvo's discovery of the first potentiometric biosensor for urea detection in 1962 and 1969, respectively. In 1975, Yellow Instruments made a significant stride by launching the first commercial biosensor. The subsequent development of the I-STAT sensor marked a major technological acceleration in the field of biosensors. Liedeberg utilized surface plasmon resonance (SPR) in biosensors for the first time in 1983, which was later refined into an SPR-based biosensor by Pharmacia Biacore in 1990. These advancements have continually shaped the biosensor field and contributed significantly to various industries. Today, biosensor technology is a dynamic, interdisciplinary domain that bridges multiple scientific disciplines, including physics, chemistry, biology, micro/nanotechnology, electronics, and medical sciences. The fusion of these areas has given rise to sophisticated technology with extensive practical applications in medicine, healthcare, food safety, environmental monitoring, and more. Consequently, biosensors have emerged as an essential tool in applied sciences (*12*).

To evaluate the effectiveness of a biosensor in analyzing a specific analyte, it must possess several key attributes. First, the biosensor must exhibit a high degree of precision in determining the analyte's concentration, with sensitivity being a critical indicator of the system's accuracy. Second, the biosensor must be selective, exhibiting a strong affinity for the target molecule being analyzed. A broad measurement range, indicating the system's measurement capacity, is also essential. Furthermore, the detection limit, or the lowest concentration of analyte detectable, should be minimized for optimal results. Additionally, the biosensor's reusability, or its ability to maintain performance without significant degradation, is an important consideration. To fulfil these criteria, it is crucial to select an appropriate bioreceptor for the target analyte and ensure effective immobilization of the biomolecules on the sensor surface. The transducer used to convert the sensor signal must also be suitable.

Portable design is another vital aspect, as on-site analysis is increasingly in demand (*11*, *18*, *23*, *27*).

Biosensors can be classified based on the sensing or recognizing component. In this context, this work will explore Surface Plasmon Resonance (SPR)-based sensors, optical sensors, and Graphene Field Effect Transistor (gFET)-based electrical sensors. These different types of biosensors offer unique advantages and challenges in terms of sensitivity, selectivity, measurement range, detection limits, and longevity. By understanding the principles and applications of each type of biosensor, researchers can optimize their design and performance for specific applications, ultimately contributing to the continued development and utility of biosensors in various industries.

2.1 Optical Biosensors

Optical transducers are widely employed in biosensor systems due to their diverse range of applications. Optical transduction involves converting a physical or chemical signal into an optical signal that can be detected, measured, and analyzed. This process is facilitated through various techniques, including fluorescence, luminescence, internal reflection, surface plasmon resonance, absorption spectroscopy, and light scattering spectroscopy(*13*, *19*, *28–30*).

Fluorescence is a prevalent technique that involves measuring light emission from a fluorescent molecule in a sample excited by a specific wavelength of light. This technique is useful for identifying the presence of specific molecules or chemicals in a sample (*31*).

Luminescence measures the emission of light from a molecule or material excited by an external energy source, such as chemiluminescence, bioluminescence, or photoluminescence (*32*).

Internal reflection is a technique based on the principle of total internal reflection, which occurs when light is reflected back into a material at an interface between two materials with different refractive indices. This technique can be used to measure the properties of a material on the surface or within it (*33*).

Surface plasmon resonance involves the interaction of light with the oscillations of electrons in a metal surface, enabling the detection of changes in the refractive index of a sample in contact with the metal surface. This technique is commonly used to measure the binding of molecules to a surface (*34*, *35*).

Absorption spectroscopy measures the amount of light absorbed by a sample at different wavelengths, which can be used to determine the concentration of a specific molecule in a sample (*36*).

Light scattering spectroscopy measures the scattering of light by particles in a sample, allowing for the determination of particle size, shape, and concentration. Optical biosensors can utilize various biological materials such as enzymes, antibodies, antigens, receptors, nucleic acids, cells, or tissues (*37*).

One of the main focuses of this thesis will be on the application of surface plasmon resonance spectroscopy. This technique offers numerous advantages for biosensing applications, including high sensitivity, label-free detection, real-time monitoring, and the ability to analyze various biomolecular interactions. By exploring and optimizing the use of surface plasmon resonance spectroscopy in biosensor development, this thesis aims to contribute to the advancement of biosensor technology and its potential applications across various industries.

2.1.1 Surface Plasmon Resonance

Surface plasmon resonance (SPR) biosensors employ optical evanescent wave sensing, utilizing light in total internal reflection to probe the properties of a solution adjacent to the sensor's surface. Surface plasma waves were first reported in 1902 by Wood , but it wasn't until the late 1960s that Otto and Kretschmann discovered the reflections induced by optical excitation of surface plasmons, leading to an understanding of surface plasmon resonance formation (*38–40*). Today, researchers continue to design highly selective sensors based on SPR theory (*13*, *19*, *41*).

Liedberg et al. developed the first SPR-based biosensor for gas detection in the 1980s (*42*). SPR sensors detect refractive index changes caused by surface plasmons, offering a simple and direct detection technique. These sensors typically employ a thin metal film, such as gold or silver, sandwiched between two permeable media with different refractive indices, like a glass prism and an analyte. Gold is favoured due to its resonance with light at the appropriate angle and its chemically modifiable surface (*43–47*) (Figure 2.1.1.1). When polarized light enters a higher refractive index medium, such as a glass prism, at an angle above the critical angle, it reflects and generates an evanescent wave that penetrates the metal film. At a specific refractive angle, the evanescent wave induces surface plasmons on the metal surface by mobilizing free electrons, resulting in a decrease in the reflected light's intensity, called surface plasmon resonance. This phenomenon is observed only at a particular angle, known as the resonance angle.

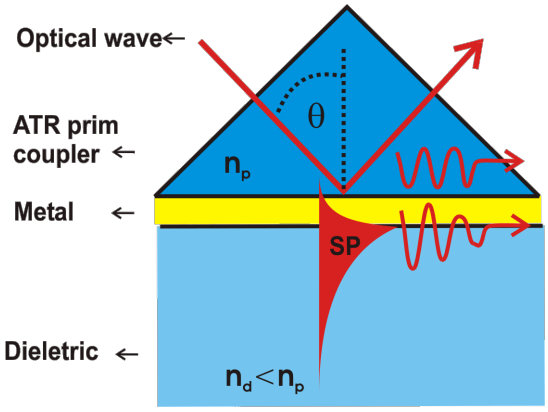

Figure 2.1.1 1 Schematic representation of prism coupled SPR system in Kretschmann configuration

EVANESCENT WAVE

The principles of surface plasmon resonance (SPR) elucidate the physical phenomena underlying the operation of SPR systems. By analyzing the behavior of surface plasmon waves and the reflection and interaction of incident light beams, we can gain a deeper understanding of these systems(*48*, *49*). A crucial aspect of SPR systems is the evanescent wave, which is essential to comprehend when studying their functionality.

Total internal reflection (TIR) is a concept that mathematically characterizes the evanescent wave and is based on the reflection of light from a boundary (*13*). The reflection of light at the interface between two media is governed by two fundamental principles: (1) the incident light must travel from a denser medium to a less dense medium, and (2) the angle of incidence must exceed a specific critical angle, beyond which reflection occurs (*38*, *49*). (Figure 2.1.1.1)

The propagation constant of the evanescent wave plays a decisive role in surface plasmon resonance systems. The electric field of an electromagnetic wave can be defined as follows:

$$E = E_0 \exp(i\omega t - ik_x x - ik_y y - ik_z z) \quad (1)$$

In this context, E represents the electric field, E_0 denotes the amplitude of the electric field, ω signifies the angular frequency, and k corresponds to the wave vector (*48*). The wave vector, which propagates parallel to the direction of the wave's propagation, can be calculated using the following equation (2):

$$k = \sqrt{k_x^2 + k_y^2 + k_z^2} = n\frac{2\pi}{\lambda} = n\frac{\omega}{c} \quad (2)$$

Where k is the wave vector, n is the refractive index, λ is the wavelength, c is the speed of light and ω is the angular frequency.

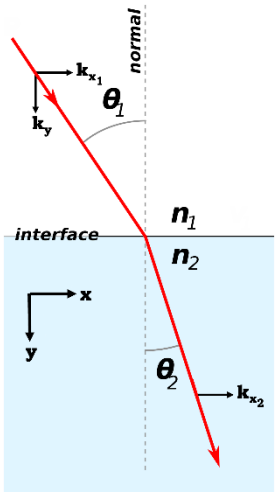

Figure 2.1.1 2 When a beam of light travels from one medium to another medium with a higher refractive index, the direction of the light changes due to refraction. The change in direction occurs because the speed of light is lower in the higher-index medium (v2 < v1), and this causes the light to bend towards the normal. This means that the angle of refraction (θ2) is less than the angle of incidence (θ1), and the ray in the higher-index medium is closer to the normal.

Snell's law, which is a fundamental principle of physics, allows us to study the behaviour of the incident beam on surfaces with different refractive indices in optical media (Figure 2.1.1.3)(*43*, *48*).

In a three-dimensional medium with x, y, and z vectors, taking the z component as zero makes our system two-dimensional. Thus, Snell's law can be used for this medium.

$$n_1 \sin\theta_1 = n_2 \sin\theta_2 \quad (3)$$

equation in terms of wave vectors;

$$k_{x_1} = k_{x_2} = k_x \quad (4)$$

is defined as. Using these two equations, the wave vector perpendicular to the surface ;

$$k_y^2 = n_1^2 \frac{(2\pi)^2}{\lambda^2}\left(\frac{n_2^2}{n_1^2} - (sin\alpha)^2\right) \quad (5)$$

is expressed as.

In the system we examined with total internal reflection rules, it is assumed that there is a ray transition from a very dense medium to a less dense medium. Accordingly, k_y takes an imaginary value (*50*). For k_y to be imaginary, it indicates the presence of a wave travelling parallel to the interface of the second surface of the beam. The wave travelling at this interface is called an evanescent wave and the second surface is called an evanescent field. The evanescent field is important for the excitation of surface plasmons. The propagation constant of the evanescent wave parallel to the surface is (*13*, *50*, *51*);

$$k_{ev} = \frac{\omega}{e} sin\Theta\sqrt{\varepsilon_p} \quad (6)$$

Kinetic analysis

SPR theory involves measuring the resonance angle shift caused by a change in the chemical composition of the environment within the plasmon field's range. This change in composition alters the angle of incidence of absorbed light, with the angle change magnitude directly correlating to the chemical change. Molecules specific to a particular analyte adsorb onto the metal film, which can include materials such as antibodies(*19*, *34*, *49*, *52*, *53*).

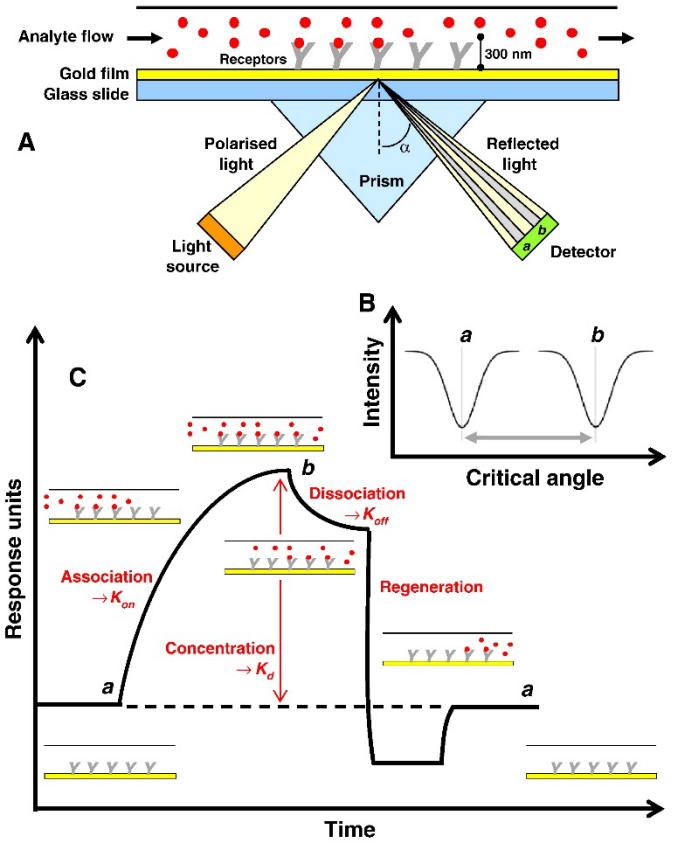

Figure 2.1.1 3 Illustration of the instrument setup for an SPR experiment. (B) Depiction of the change in the angle of incident light from a to b as a result of the binding of an analyte molecule to a bioreceptor molecule. (C) Sensogram response of the SPR experiment. Figures (A-C) were replicated from Patching (2014) with approval from Elsevier. Copyright 2014, Elsevier.

Figure 2.1.1.2 presents a schematic representation of a Surface Plasmon Resonance (SPR) experiment in BioNavis commercial device setting, a technique commonly utilized to assess the binding of an analyte molecule to a receptor molecule. The figure comprises three sections: A, B, and C. Section A depicts the instrument configuration for an SPR experiment. The technology employs an optical approach to determine the refractive index near a sensor surface. It takes advantage of total internal reflection of light at a surface-solution interface, generating an electromagnetic field or evanescent wave that extends a limited distance (up to 300 nm) into the solution. A thin gold film on a glass support serves as the surface, forming the base of a small-volume flow cell (less than 100 nl). An aqueous solution continuously flows through the cell. To detect the binding of an analyte to a receptor molecule, the receptor is typically immobilized on the sensor surface, while the analyte is introduced into the aqueous solution via the flow cell. A laser source emits polarized light, which is directed through a prism towards the gold film's underside, where surface plasmons are generated at a critical angle of incident light. Section

B illustrates the shift in the critical angle of incident light from angle a to angle b upon the binding of an analyte molecule to a receptor molecule. Section C displays the SPR experiment's response as a sensorgram. If an interaction occurs between the immobilized receptor and the analyte molecules, the refractive index at the gold film's surface changes, resulting in an increase in signal intensity. Resonance or response units (RU) describe the signal increase, with 1 RU corresponding to a critical angle shift of 10^{-4} deg. The figure also outlines the primary phases of an SPR experiment—the association phase, steady-state phase, and dissociation phase—and how these phases facilitate the measurement of association rate (k_{on}), dissociation rate (k_{off}), and binding affinity (K_D) between the immobilized receptor and the analyte molecule(*48*, *54*). Binding analysis will be explained detailed in Kinetic analysis section. When a sample containing analytes, such as bacterial cells, interacts with adsorbed molecules on the surface, it induces a change in the metal surface's component. The resonance angle shift of the incident light is measured, and the shift magnitude is directly proportional to the analyte concentration in the sample. The relationship between the molecules ensures minimal cross-reactivity, thereby reducing the detection of other molecules by the sensor.

The evanescent wave biosensors provide an opportunity to observe the kinetics of biomolecular interactions in a solution, specifically between a biomolecule in the solution and another biomolecule immobilized on a surface. This analysis begins with a straightforward 1:1 interaction model (*55*), which is grounded in the Langmuir adsorption isotherm (*56*). This isotherm relies on three fundamental assumptions:

1. A homogeneous monolayer covers the surface.
2. All binding sites are equivalent, and the surface is uniform.
3. The adsorption potential of a molecule at a specific site is unaffected by the occupancy of neighboring sites.

According to the assumptions, dynamic equilibrium would be:

$$A + B \underset{K_{on}}{\overset{K_{off}}{\leftrightarrows}} AB \qquad (7)$$

Where A and B are the molecules in solution and on the surface respectively. The forward and reverse rate are described by the adsorption or association rate constant (K_{on}) and desorption or dissociation rate constant K_{off}.

The association rate is;

$$\frac{d[AB]}{dt} = k_{on}[A][B] \quad (8)$$

And the dissociation rate is;

$$-\frac{d[AB]}{dt} = k_{off}[AB] \quad (9)$$

Because of the dynamic equilibrium of both processes, both rates are equal to each other;

$$k_{on}[A][B] = k_{off}[AB] \quad (10)$$

From this, the equilibrium constants can be expressed by two constants: The dissociation constant K_D;

$$K_D = \frac{[A][B]}{[AB]} = \frac{k_{off}}{k_{on}} \quad (11)$$

And the affinity constant K_A;

$$K_A = \frac{[AB]}{[A][B]} = \frac{k_{on}}{k_{off}} \quad (12)$$

2.2 Electrical biosensors

Electrical biosensors are forms of biosensors that detect and measure biological substances or events using electrical impulses. The idea behind these systems is to convert biological reactions into electrical signals. An antibody, enzyme, or nucleic acid that is specially made to bind to the target molecule is the usual biological detection element. In electrical biosensing systems, biological signals are converted into electrical signals by a transmitter. Field-effect transistors (FETs), electrodes, and nanowires are some examples of transducers. The electrical characteristics of the transducer, such as resistance, capacitance or current, change when biological recognition elements are linked to the target molecule. Electrochemical biosensors are a type of electrical biosensor technology that detects and measures biological substances

through electrochemical processes. Usually, they are composed of electrodes coated with biological identification elements, electrolyte solutions, and conductor materials.

When the target molecule binds to a recognition element, the current or current of the electrode changes. Field-effect transistor (FET) field-effect transistors are used to identify and quantify biological substances as another type of electrical biosensing technologies. The biological recognition element is attached to the FET gate electrode or on the channel; usually FETs are composed of the gate electrode, source, and drain electrode. The conductivity of the FET changes when the target molecule binds to the recognition element.

Impedance biosensors are a third type of electrical biosensing system that measures the impedance (i.e., resistance to alternating current) of a biological sample. They are typically composed of two electrodes, and a biological recognition element is attached to one of the electrodes. When the target molecule binds to the recognition element, it produces a change in impedance between the two electrodes.

A field effect transistor (FET) is a type of transistor that uses an electric field to control current flow. There are two main types of FETs: metal-oxide-semiconductor field-effect transistors (MOSFETs) and junction field-effect transistors (JFETs). MOSFETs are the most common type of FET in modern electronics. MOSFETs consist of a door, source, and drain. The door is separated from the source and discharged by a thin insulation layer, usually made of silicon dioxide. The gate is also connected to a metal or polysilicon electrode that is used to control the electric field in the channel region between the source and the drain. The electrical field created by the gate electrode induces a concentration of the charge carrier in the channel region, which controls the current between the source and the drain. The current of the MOSFET is described as follows:

$$I = C_{ox} \frac{W}{L} (V_{GS} - V_{Th}) V_{DS} \quad (13)$$

where I is the discharge current, is the electron movement, Cox is the oxide capacity of the unit area, W and L are the width and length of the channel region, Vgs is the gate-source voltage, Vth is the threshold voltage, and Vds is the discharge source voltage. The threshold voltage is the voltage at which the MOSFET starts to conduct current. It depends on the concentration of doping in the channel region and the difference in work function between the gate electrode and the channel region. The oxide capacity per unit area is proportional to

the thickness of the oxide layer, which can be controlled during the manufacturing process. MOSFETs can be used as transducers in electrical biosensors. In biological sensing applications, the gate electrode is generally functionalised with a biological recognition element, such as an antibody or DNA probe. When the target molecule binds to the recognition element, it produces a change in the concentration of the charger in the channel region that can be detected as a change in the discharge current.

2.2.1 Graphene

Graphene, a two-dimensional carbon allotrope, serves as the foundation for other carbon structures. By rolling single graphene layers, carbon nanotubes are formed, while stacking multiple layers results in graphite and aggregating the graphene results in fullerene. Despite its theoretical existence being known since the 1940s, graphene remains a unique form of carbon (*14*, *57*). In 2004, Andre Geim and Konstantin Novoselov proved the existence of graphene, a two-dimensional carbon allotrope, by successfully obtaining a single layer of graphite and transferring it to a silicon stamp. This ground-breaking discovery sparked an immense surge in research on graphene and gave rise to a new field of materials science, focussing on two-dimensional materials. Soon after the discovery of graphene, other two-dimensional materials, such as molybdenum disulphide and silicene, were also discovered. The demonstration of the field effect in graphene also marked the beginning of research on graphene field effect transistors, leading to the rapid development of graphene-based integrated circuits in just over a decade (*58*, *59*).

Graphene possesses exceptional characteristics that render it fit for a multitude of uses. Its thermal conductivity, for instance, stands at a remarkable 5,103 W/mK at room temperature, a value that is roughly thirty times greater than that of silicon (*60*). The thermal conductivity of a material is of utmost significance in electronic applications, and graphene boasts exceptional thermal conductivity compared to other materials. In addition to its remarkable thermal properties, graphene is extremely durable and optically almost transparent. Its mechanical properties are equally unique, with a fracture strength that surpasses that of steel and elastic properties that are comparable to those of diamond. Furthermore, when samples of graphene are kept incredibly clean, they display interesting phenomena such as Shubnikov-de Haas oscillations (*61*), minimum conductivity (*57*), and fractional quantum Hall effect (*62*).

Despite its outstanding material properties, graphene lacks an electronic band gap, which is necessary for low power consumption in many electronic applications. However, when two layers of graphene are combined to form bilayer graphene, a small but significant energy gap of around 300 meV can be generated when an electric field is applied perpendicular to the double layers.

Graphene Production Methods

Graphene can be produced through a variety of physical and chemical methods. Physical methods of obtaining graphene include micromechanical cleavage (exfoliation) of multilayer pyrolytic graphite crystals and epitaxial growth on silicon carbide. (*63*) Chemical methods, on the other hand, involve the use of chemical vapour deposition (CVD) on thin film nickel or copper metals. Another chemical process for obtaining graphene involves the reduction of graphene oxide, which is derived from graphite.

Exfoliation

Graphite is comprised of graphene sheets held together by van der Waals bonds. These bonds can be broken down to produce graphene, and there are various methods to achieve this. One such method is called exfoliation, in which graphite is combined with potassium in a specific ratio and heated to 200 degrees, allowing potassium to penetrate between the graphene layers. The resulting mixture is then placed in ethanol, leading to a reaction between ethanol and potassium that causes the graphene layers to separate from each other. The implementation of this method is depicted in Figure 2.2.1.1 (*64*).

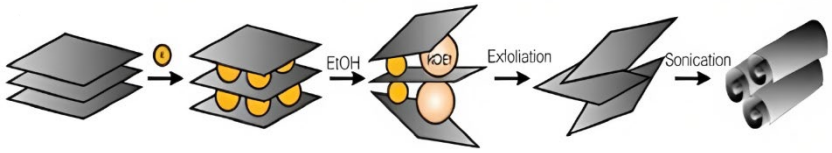

Figure 2.2.1 1 representation of Obtaining graphene through the exfoliation method

Epitaxial Growth

The epitaxial growth method entails the cultivation of graphene on silicon carbide. This process starts with the formation of a silicon carbide layer that undergoes growth conditions,

followed by heating to a temperature between 1000 and 2000 degrees. At this elevated temperature, silicon is released and the residual carbon atoms unite to form graphene. The graphene layers that are produced in this manner are seamlessly integrated with the silicon carbide substrate, as silicon carbide serves as the source of carbon.

The new graphene layers remain beneath the first layer, leading to the formation of multilayer graphene. However, the disadvantage of this method is that as each subsequent layer is produced, there is no escape for the silicon, ultimately causing the growth process to end. Figure 2.2.1.2 illustrates the production process.(*65*).

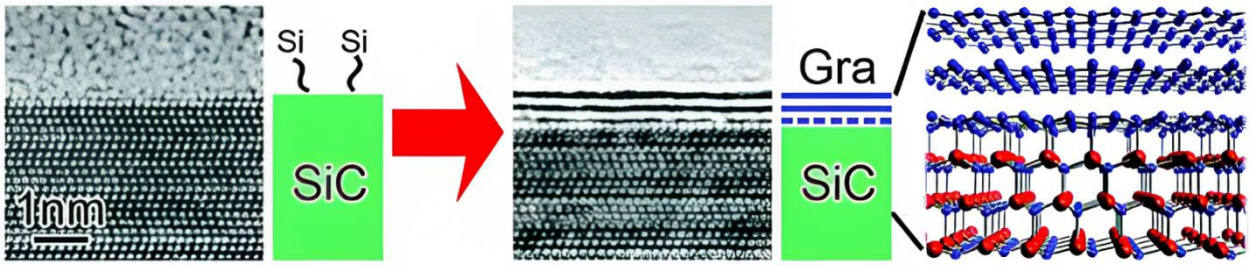

Figure 2.2.1 2 Obtaining graphene through the epitaxial growth method

Chemical Vapor Deposition

Chemical vapour deposition (CVD) is a widely used method to produce graphene. This method is carried out in a cleanroom environment using a specialised CVD device to produce graphene with the desired dimensions. The process involves heating a material in a closed container and exposing it to reactive gas molecules. As a result of this reaction, the material accumulates gas molecules on its surface. The method primarily relies on the deposition of carbon atoms in the vapor form onto transition metals, such as nickel, palladium, or copper. To transfer the graphene onto a desired substrate, a photoresist or similar chemical compound is applied on the transition metal. The photoresist is then heated to bond with the graphene. The transition metal is then etched away, leaving the graphene adhered to the photoresist. The photoresist is subsequently removed, leaving only the graphene. The carbon source used in this method is typically hydrocarbons, such as methane. The production process is depicted in Figure 2.2.1.4. (*66*)

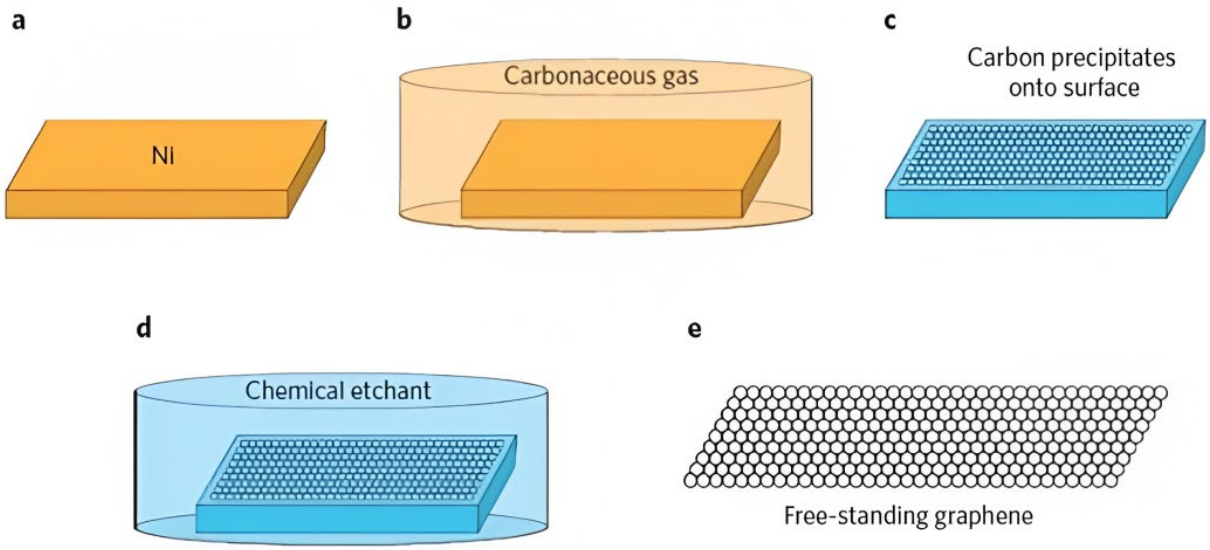

Figure 2.2.1 3 Schematic representation of large-scale graphene production via chemical vapor deposition (CVD): (a) Nickel layer deposition and crystallinity control, (b) Carbon atoms generation and diffusion at elevated temperature, (c) Graphene formation during cooling, (d) Detachment of graphene through chemical etching, and (e) Transfer of free-standing graphene to target substrates. Temperature and chemical gradients are depicted with color variations (orange for hot, blue for cold; orange for gas, blue for etchant).

Reduction of graphene oxide

Graphene oxide is obtained by oxidation of graphite, which results in the separation of its layers. The resulting graphene oxide has a C/O ratio that is approximately equal to 2. The next step in obtaining graphene is to reduce the graphene oxide. There are several methods to achieve this reduction, including thermal, chemical, and microwave techniques. (*67*). The advantage of this method is that it is relatively inexpensive and easy to carry out. However, the drawback is that the resulting graphene still contains oxygen atoms, which leads to defects in its structure. As a result, it is challenging to obtain pure graphene using this method. Figure 1.6 illustrates this, as the structure of the resulting graphene is not uniform. The presence of oxygen atoms and structural defects reduce the potential for using this graphene in applications where high performance and purity are required. (*65*)

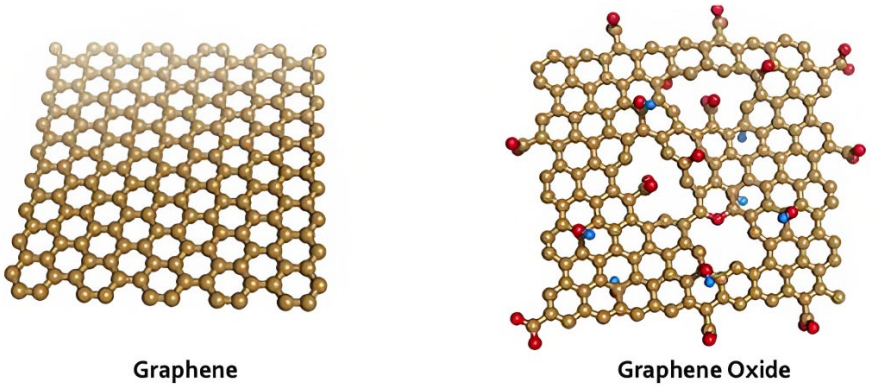

Figure 2.2.1 4 Representation of untreated Graphene Oxide (left) and Reduced Graphene Oxide (right)

Electrical Properties of Graphene

Graphene is known for its exceptional electronic properties, particularly its high carrier mobility. The mobility of exfoliated graphene has been measured to be around 10,000 to 15,000 cm2V/s and is estimated to have an upper limit of around 40,000 to 70,000 cm2V/s. (*68*) This high conductivity makes graphene the best conductor known to man and has led to numerous technological advances. However, its lack of a band gap, which is necessary for efficient switching in electronics, limits its use in applications such as transistors. To overcome this, a band gap can be induced in graphene by applying an electric field perpendicular to a

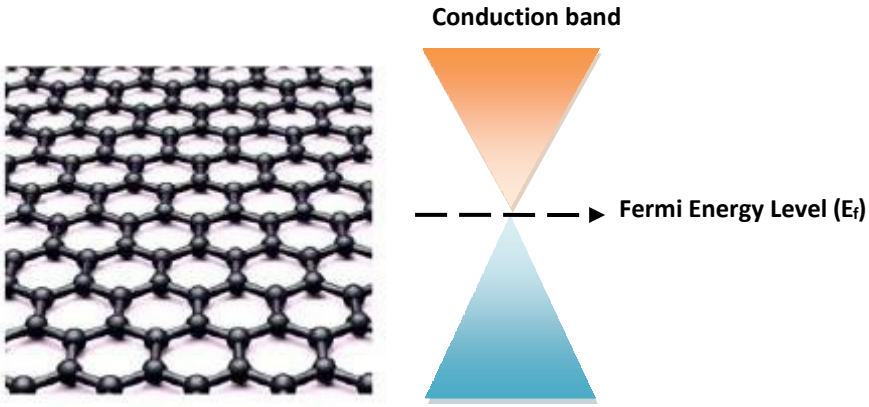

Figure 2.2.1 5 Graphene band structure

bilayer graphene, which has been shown to create a band gap of 130 meV. (*69*)Despite these limitations, graphene still has great potential and value in the commercial market, particularly in gated transistors.

2.2.2 Graphene Based Field Effect Transistor

The graphene field-effect transistor (GFET) biosensor design consists of three main components. These are; the transistor structure with three electrodes, the graphene responsible for current conduction and the transmission of biological events to the sensor located between the drain-source electrodes (drain-source channel), and the analyte-specific receptors on the graphene surface (Figure 2.2.1 6 a). There is an insulating layer on top of the substrate where graphene is transferred, preventing unwanted electrical conduction between different electrodes. In GFET structures, doped silicon is generally used as the semiconductor layer and SiO_2 as the insulating layer. The electrodes called source, drain, and gate in the GFET structure have the source and drain electrodes in direct contact with graphene, allowing current flow along the graphene (Figure 2.2.1 6 c). The source and drain electrodes are made of conductive materials like gold (Au), and a thin adhesive layer of chromium (Cr) or nickel (Ni) is used to adhere the Au electrodes to the oxide surface (*70*, *71*). The third electrode called the gate is not in direct contact with graphene, and its position changes depending on the selected experimental protocol for analyte detection. A back-gate measurement is generally taken if the sensor is in an air or gas environment (Figure 2.2.1 6 b). In this case, a material with lower conductivity separated from the drain and source electrodes by an insulating layer is used as the gate. Measurements are mostly taken over silicon, and the oxide thickness on the silicon determines the capacitance of the applied gate voltage. The capacitance of the oxide layer is inversely proportional to thickness $C_g \approx C_{ox} = \varepsilon_{ox}/t$, where ε_{ox} is defined as the dielectric permittivity.

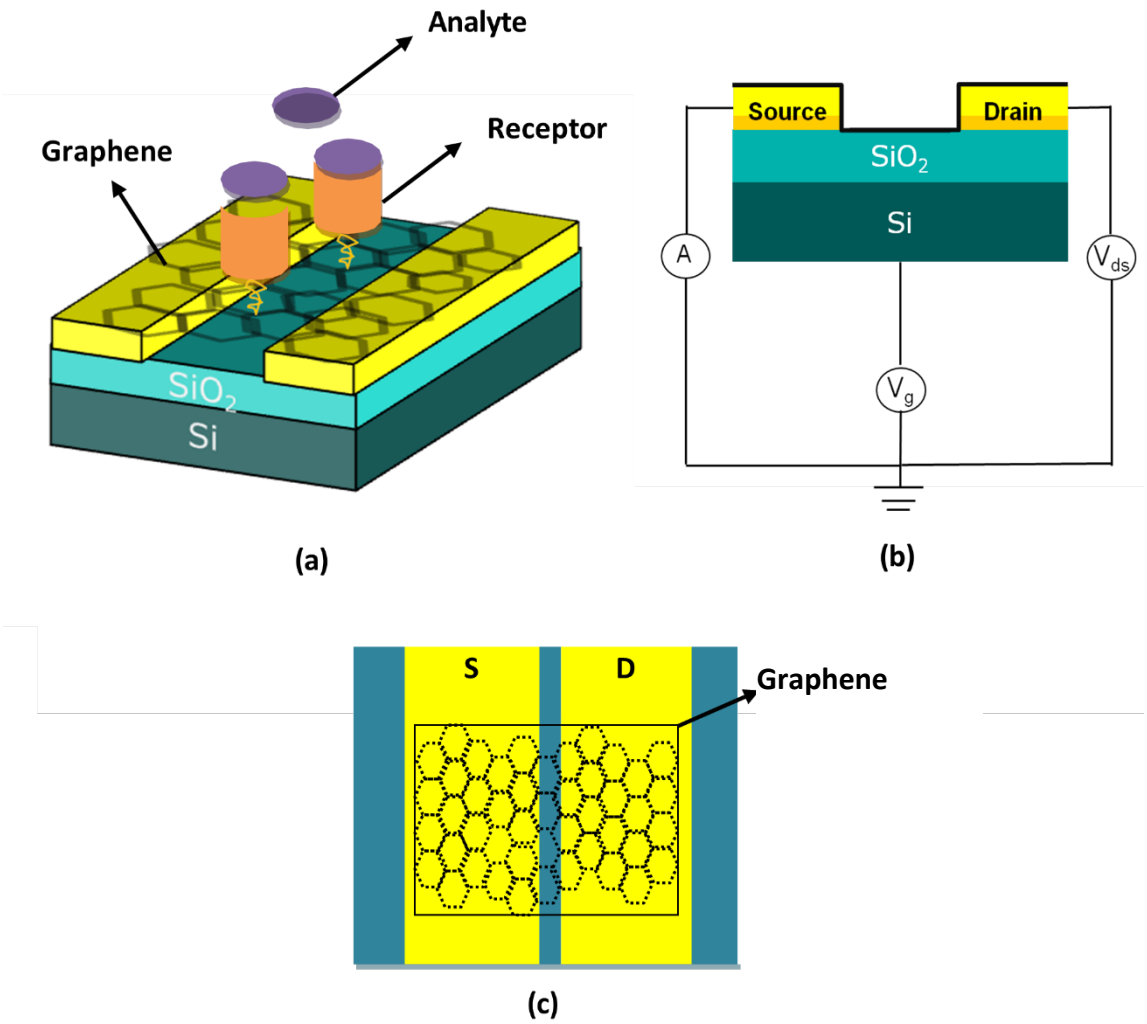

Figure 2.2.2 1 GFET biosensor design a) Interaction of receptor and analyte on functionalized graphene of GFET biosensor, b) Back-gate electrode arrangement, c) Interaction of graphene with source-drain electrodes

In biosensor applications using GFET, a solution is used, so in this case, the gate electrode is applied through the solution and is called top-gate or liquid-gate. Ag/AgCl or platinum (Pt) is used as the reference electrode where the gate potential is applied (*72*, *73*). The gate electrode connects to graphene through the electrical double layer (EDL) and, in this case, the capacitance is determined by the EDL formed by the ions in the solution on graphene. The EDL exhibits behaviour similar to an insulating layer with angstrom or nanometer (nm) thickness (*74*). The gate capacitance obtained in this form is much larger than the back-gate capacitance and can approach the quantum capacitance (C_q) level. In this case, capacitance is determined as $C_g = [C_q - 1 + C_{EDL} - 1] - 1$ (*75*). Conductivity and capacitance values are highly

dependent on the arrangement of the gate electrode. In GFETs, a reaction cell is often fixed to the GFET substrate during the process of holding the analyte on the graphene, allowing the sample to be held and controlled (*76*). Due to the small sensing area of GFETs, such cells are often designed to hold low sample volumes in the order of tens of microliters (*77–80*). Polydimethylsiloxane (PDMS) can be cited as a material suitable for producing the cell because of its flexibility, inertness as a non-reactive material, transparency, low cost, and easy production (*81–83*). PDMS is widely used in the fabrication of microfluidic devices and reaction cells for GFET biosensors. Its properties make it suitable for maintaining an enclosed environment for the sample during the detection process and ensuring proper interaction between the analyte and the graphene surface. Moreover, its transparency allows for real-time monitoring of the reaction process, if needed.

When designing and optimizing GFET biosensors, various factors need to be considered, such as the type of analyte-specific receptors on the graphene surface, the experimental conditions for the detection process, and the fabrication method of the GFET device (*41*, *84*). The choice of receptors is crucial, as they determine the selectivity and sensitivity of the sensor for the target analyte. The experimental conditions, such as temperature, pH, and buffer composition, can also affect the performance of the biosensor and should be optimized to achieve the best results (*21*). Finally, the fabrication method and quality of the GFET device can have a significant impact on the reproducibility, sensitivity, and overall performance of the biosensor.

Electrical Characterization of Graphene Field-Effect Transistors

The electrical characterization of GFETs is based on the measurement of current passing through the graphene located between the source-drain channels. The current can be controlled by the electric field, and the magnitude of the electric field is affected by the physical and chemical changes occurring on the channel. The sensitivity of single-atom-thick graphene to these physical and chemical changes is very high and provides a direct electrical response. The primary goal in FET biosensors is to capture the analyte, and the analyte arriving at the graphene surface causes changes in the existing current due to its charge, generating a high electrical signal response through graphene.

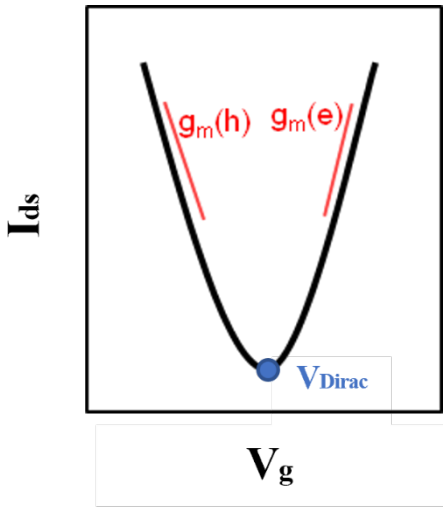

Figure 2.2.2 2 gFET Transfer characteristic (I_DV_G), showing ambipolar behavior of graphene layer with a charge neutrality point (CNP, DIRAC) showed as V_{CNP}

The flow of charge carriers provided by the potential applied between the drain-source electrodes along the channel can be changed by the potential applied from the gate electrode and can cause more charge carriers to flow in the channel. FET devices are characterized by three characteristic curves: transfer curves, output curves, and time series curves, based on the applied voltage and resulting current changes.

Transfer curves

The transfer curves of the transistor are generated by the drain-source current (I_{ds}) obtained by applying a gate voltage (V_g) at a constant drain-source voltage (V_{ds}). As a result, the obtained Ids (or resistance $R_{ds} = V_{ds}/I_{ds}$ or conductivity $G_{ds} = I_{ds}/V_{ds}$) is shown as a function of the gate potential on the graph. The commonly observed transfer curve for GFETs is shown in Figure 2.2.2.1. The applied gate potential leads to a change in the polarity of the majority charge carriers. The left side of the transfer curve represents the increase of positively charged carriers (holes) (p branch), while the right side represents the increase of negatively charged carriers (electrons) (n branch). The current formed between these two branches due to the density of charge carriers reaches a minimum at the gate voltage (V_{Dirac}) value called the threshold value or charge neutrality point (Dirac), and this value is equal for both branches.

Considering the change in carrier mobility, GFET behavior is defined by Equation (14) when a low V_{ds} potential is applied (*85*).

$$I_{ds} = \mu C_g W[(V_g - V_{th})V_{ds} - \frac{Vds^2}{2}] \quad (14)$$

The threshold value can linearly change on both branches according to Equation 15.

$$I_{ds} = g_m (V_g - V_{CNP}) \quad (15)$$

The resulting change in current relative to the input voltage is denoted as g_m (conductance) and depends on the width (W) and length (L) of the graphene. This value does not have to be equal for electrons and holes, and an asymmetric transfer curve can be observed in this case. μ in Equation 16 represents carrier mobility, and C_g represents gate capacitance (*86*).

$$g_m = \frac{W}{L} \mu C_g V_{ds} \quad (16)$$

In a biosensor, the change in conductance, $g_m = \frac{\partial I_{ds}}{\partial V_g}$, causes a change in the slope of the p and n branches of the transfer curve. Conductance is an important parameter for determining transistor performance, as a small change in voltage generates a high current change response. The conductance in a transistor is related to the electronic properties of graphene and its carrier mobility, which is an indicator of its structure. Therefore, carrier mobility can be defined using Equation 17 for the linear region of the transfer characteristic.

$$\mu = \frac{dI_{ds}}{dV_{gv}} \frac{L}{WC_g V_g} \quad (17)$$

V_{Dirac} change is used in GFET biosensors to detect the analyte. The change depends on the doping level of the graphene. For pristine graphene, V_{Dirac} is expected to be close to zero at a constant low drain-source voltage. For p-type doped graphene (where holes are the majority charge carriers), this value is more positive, and for n-type doped graphene (where electrons are the majority charge carriers), it is more negative. The doping level depends on the quality of graphene, the charge distribution on it, the underlying substrate, and the electrodes (*87*). In biosensor experiments, the change in the Dirac value is observed for each stage by applying a gate potential, and the analyte is detected through the change difference. When the analyte interacts with graphene, the charge of the analyte causes a change in the graphene's charge and doping, resulting in a change in the Dirac value (Figure 2.2.2 3 a). When a positively charged analyte arrives on the graphene, it attracts negative charge carriers, causing negative

doping in the graphene and a shift in the V_{Dirac} value in the negative direction. Conversely, when a negatively charged analyte arrives on the surface, it attracts positive charge carriers, causing positive doping in the graphene and a shift in the V_{DIRAC} value in the positive direction (*88*).

The carrier charge density (n) changes depending on the shift of the threshold value point towards positive or negative and is determined according to equation 18. In the equation, e represents the elementary charge, and d represents the distance between capacitors. For the gate voltage effect, charged proteins bound to the V_g surface are equivalent to positive or negative potential charge changes that cause a change in V_g carrier density; for the charge tunneling effect, the carrier density in V_g changes by loading electrons onto V_g or pulling electrons from charged proteins.

$$n = \frac{Q}{e.Volume} = \frac{C(Vg-Vth)}{eWLd} \quad (18)$$

Impurities in graphene are inversely proportional to conductivity (*60*, *87*, *88*). These impurities can cause electrical charge dispersion after the analyte is added to the biosensor, and therefore the noise in transistor conductivity may increase. This negative change in conductivity alters the slope of the p and n branches in the transfer curve. These electrical extra dispersions affecting the charge carriers often cause the slopes of the transfer curves to shift asymmetrically (Figure 2.2.2 3 b).

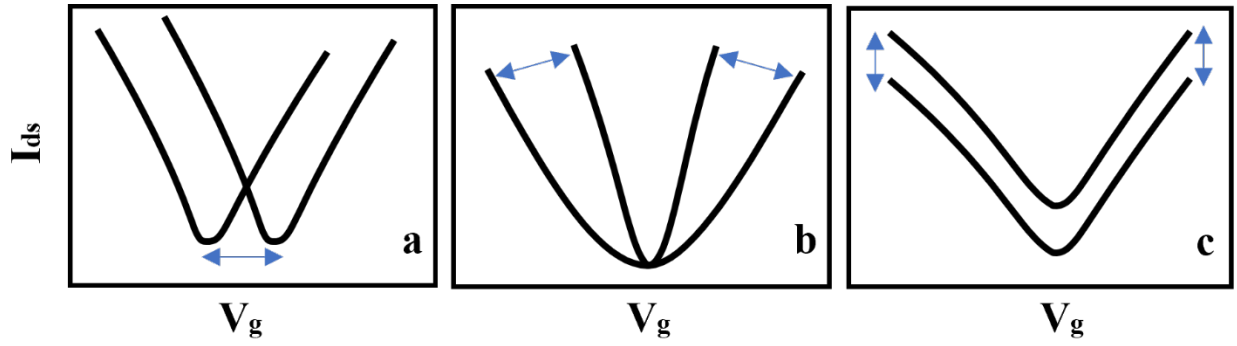

Figure 2.2.2 3 GFET transfer curves a) Change in Dirac point, b) Effect on the conductivity of electrons g_m(e) and holes g_m(h), c) Change in current intensity.

The intensity of the electrical current causes a change in the transfer curves. This change can occur not only in the p and n branches but also in the Dirac value (Figure 2.2.2 3c). The electrical current depends on the carrier charge density and speed. In biosensor applications,

when the analyte comes to the surface, it can vertically change the Dirac value depending on the carrier charge density, and this can also lead to asymmetric changes caused by conductivity (*80*).

In addition to transfer curves, GFET electrical characterization can be performed with output curves. In the output curves, the Ids current is obtained as a function of the drain-source voltage (V_{ds}) at a fixed Vg value. In this characterization response, as the applied potential

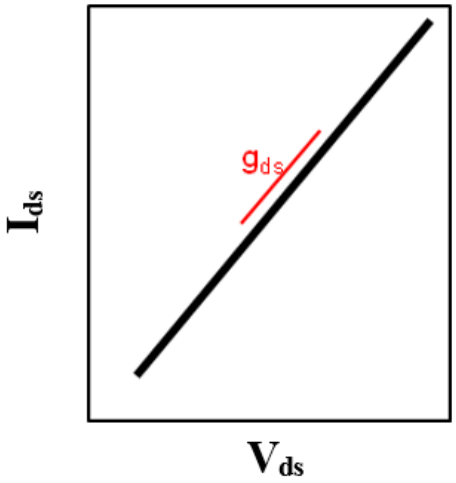

Figure 2.2.2 4 The graph of Drain-Source current versus Drain-Source Voltage displays the relationship between these two variables, with the slope of the curve representing the resulting conductance

increases, the current intensity also increases in the same polarity, as shown in Figure 2.2.2 4. The slope of these curves is generally a good indicator of the contact between graphene and source-drain electrodes and the amount of charge that can be carried along the graphene. Good-quality graphene and good contact between the electrodes are determined by the observation of ohmic behavior at low potential (*89*, *90*). In practice, a positive slope and linear regime can sometimes mean poor contact and the presence of defects (*86*, *91*). The conductivity provided in the output curves, g_{ds}, is determined by the slope of the curve. The current intensity is associated with the constant V_g that controls the carrier density (*21*, *41*, *92*, *93*). In GFET biosensor applications, the slope of the curve changes depending on the concentration of the analyte to be detected, which is related to its charge.

Time resolved measurement

Time-dependent current curves are determined at a constant V_g and V_{ds} value. Time curves are initiated before analyte binding in biosensor applications and continued after binding,

resulting in current changes in the time curves due to the change in carrier charge concentration depending on the charge carried by the analyte (Figure 2.2.2.5). The detection and amount of the analyte can be determined by the change in electrical current. These time curves are formed at a point in the transfer slope over time, as V_g is constant. The choice of constant gate voltage directly affects the signal's intensity and polarity (*94*). Generally, the gate voltage at which high current is obtained in the transfer curve is kept constant (*95*). Therefore, time curves operate as a mechanism dependent on transfer curves. Consequently, the transfer curve directs the current intensity in the time curves. The current change (ΔI_{ds}) can be related to the voltage change (Equation 19).

$$\Delta V_{Dirac} = \frac{\Delta I_{ds}}{g_m} \tag{19}$$

In summary, GFET biosensor applications involve various electrical characterizations, including transfer curves, output curves, and time curves. These characterizations help to understand the relationship between the carrier charge density, gate voltage effect, impurities in graphene, and the performance of the biosensor. By analyzing the slopes and changes in these curves, researchers can optimize the biosensor's sensitivity and specificity for detecting specific analytes. Additionally, the understanding of the underlying mechanisms, such as charge tunneling and ohmic behavior, can contribute to the development of more advanced and efficient biosensors in the future.

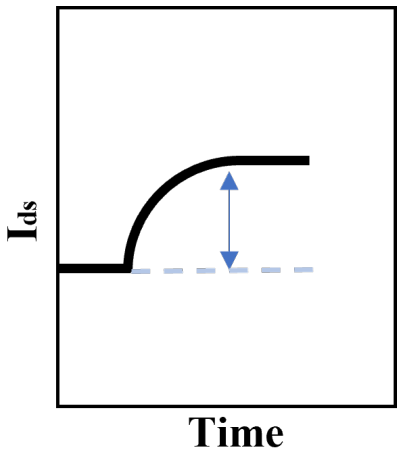

Figure 2.2.2 5 A schematic representation of a time-resolved curve at a fixed gate voltage shows how the current changes over time at a constant gate voltage.

Liquid-Solid Interface

The complex nature of electrodynamic behavior at the interface between a liquid and a solid has been a topic of investigation for centuries. Esteemed scientists, such as Helmholtz, Debye, and Stern, have made substantial contributions to this field. While an exhaustive discussion of this subject exceeds the scope of this thesis, a succinct introduction to the relevant phenomena will be offered in the following subsections. The Debye length (λ_D) quantifies the overall electrostatic impact of charge carriers in solutions and can be considered as the interaction radius of molecules within a solution, which pertains to electronic interaction. For example, a λ_D of 100 nm suggests that a molecule in the solution has a spherical radius (or Debye sphere) of 100 nm and is likely to interact (either attract or repel) with other molecules within this interactive volume. To compute λ_D for ionic liquids or electrolytes, the ion strength and properties of the present salts must be determined, as illustrated by the equation below:

$$\lambda_D = \sqrt{\frac{\varepsilon_r \varepsilon_0 k_B T}{2 N_a e^2 I}} \tag{20}$$

In this formula, *I* represents the total ion strength of the electrolyte, T indicates the temperature, ϵ_r is the dielectric constant of the electrolyte, ϵ_0 refers to the dielectric constant of a vacuum, e symbolizes the unity charge, N_A is Avogadro's constant, and k_B is Boltzmann's constant. It is crucial to recognize that ϵr decreases linearly with the increasing concentration of the electrolyte. As a result, ϵr should not always be assumed constant and depends on the ion strength (*96*–*98*) (for example, an ionic strength of 8.5 mM has ϵ_r = 80, while a 170 mM ion strength has ϵ_r = 70). Stern et al. (*99*) have also demonstrated the importance of the Debye screening length for field-effect transistors (FETs), emphasizing that the expected response signals of liquid-transistors are heavily influenced by this parameter.

Electrical Double Layer – Graham Equation

The electric double layer (EDL) formed at the rGO-liquid interface has a significant impact on the measurement setup, necessitating a more detailed analysis. The most fundamental theory concerning the behavior of ionic liquids at charged interfaces is the Helmholtz double layer theory (*100*), which describes the innermost layer of water molecules at the surface. This theory does not take into account diffusion, adsorption, or the solvent's dipole moments. The Gouy-Chapman model includes a diffuse model, which depicts the charge distribution according to the distance from the surface (*101*). The Stern model integrates both theories by introducing a Stern layer at the interface, providing greater accuracy for highly charged surfaces (*102*). A graphical illustration of the EDL and the theories of Stern and Gouy-Chapman is presented in Figure 2.2.2.6. The Gouy-Chapman theory for EDLs, incorporating optimizations proposed by Grahame (*103*), is the focus of the analysis here.

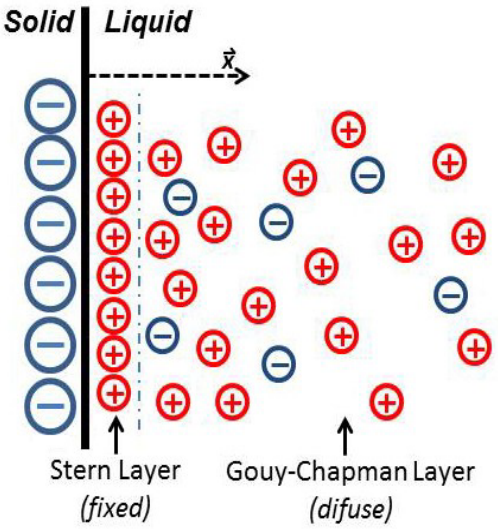

Figure 2.2.2 6 Schematic illustration of the liquid- solid interface, the fixed Stern layer and the diffuse Gouy-Chapman layer.

The theory discussed here can be applied to any electrically charged liquid-solid interface to describe surface phenomena, but it requires a relationship between the surface charge density (σ), the number of free charges ni(x), and the surface potential (Ψ(x)). The x-coordinate mentioned here is directed normal to the surface. To obtain a suitable dependency of the charge distribution along the liquid-solid interface, the one-dimensional Poisson equation must be established:

$$\nabla^2 \Psi = -\frac{\rho_e}{\varepsilon_r \varepsilon_0} \qquad (21)$$

Here, ε_r and ε_0 represent the electrolyte and vacuum permittivity, respectively, Ψ stands for the surface potential, and ρ_e denotes the surface charge at the interface. Additionally, the distribution of charge carriers must be considered, and the Boltzmann statistics for the distribution of ions in the electrolyte are applied, yielding the connection of charge to the surface potential:

$$n_i = n_i^0 e_i^{\frac{-W}{k_b T}} \quad (22)$$

In this equation, n_i is the average local concentration of i-ions at the observed point, n_i^0 the total number of ions present, k_B Boltzmann's constant, T the temperature and W_i is the work needed to move an ion in the field. This work can also be expressed as the charge movement in the potential for movements towards the surface:$W^+ = e\,\Psi(x)$; and away from the surface: $W^- = -e\Psi\,(x)$. Substituting these observations into the Poisson equation, the following results for movement towards or away from the charged surface are obtained:

$$\rho(x) = ze[n^+ - n^-] \quad (23)$$

$$n^+(x) = n(\infty)e^{(-\frac{z\Psi(x)}{k_B T})} \quad (24)$$

$$n^-(x) = n(\infty)e^{(\frac{z\Psi(x)}{k_B T})} \quad (25)$$

Where n(∞) is the number of ions at infinite distance from the surface, z is the valency of the observed ions and e the unity charge. Since the rGO-FET system for which these calculations are performed in this work can be assumed as a low potential case, a suitable approximation for the surface potential can be applied $e\Psi_0 = e\Psi(x = 0) \ll k_B T$, yielding the simplified from of the Poisson-Boltzmann equation:

$$\Psi = \Psi_0 e^{-z/\lambda_D} \quad (26)$$

Calculating the surface charge from these observations, the Grahame equation for the distribution of charges in an electrolyte at a charged liquid-solid interface can be obtained:

$$\sigma = \sqrt{8n(\infty)\varepsilon_r \varepsilon_0 k_B T}\,\sinh(\frac{ze\psi_0}{zk_B T}) \quad (27)$$

This result reveals the dependency of the EDL decay along the direction perpendicular to a solid with surface charge σ on the ion concentration of the electrolyte. It can be used for calculations of the EDL thickness. When λD and the topography of the biological materials on the surface are known, this method enables the study of the charge distribution around

binding events. Consequently, it allows the optimization of working parameters, such as ion concentration and applied potentials, for the detection of biomolecules in liquids.

3 Assay Implementation

The design of biosensors involves combining inorganic materials on a substrate with organic layers to create a functional bio interface. This requires careful consideration of the immobilization strategy to be used, which is dependent on the application, size, and characteristics of the analyte, and the type of biomolecular recognition element (BRE) being employed(*15*, *104*, *105*). Key factors to be considered in the immobilization process include preserving the structure and functionality of the BRE, orienting it in a favorable direction, ensuring a high density on the surface, and minimizing non-specific binding to the surface.

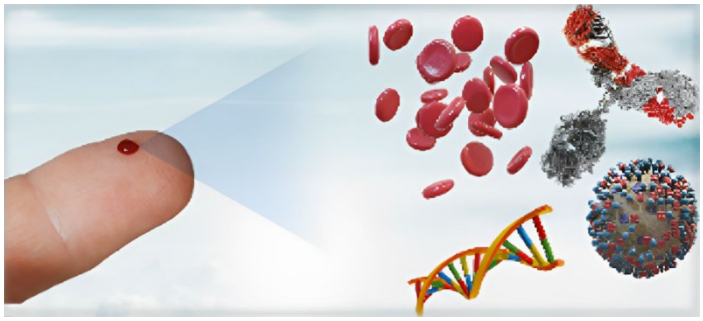

Figure 3 1 Representative picture of what human blood contains. Such as blood cells, Immunoglobin G (IgG), Immunoglobin M (IgM), DNA helixes, viruses, bacteria, etc.

Gold is the most commonly used metal for biosensing due to its chemical inertness and stability, and various modification protocols have been developed for its use(*15*, *105*). The simplest approach involves physically adsorbing the BRE to the metal surface, but this method is limited by low surface coverage, random orientation, and the tendency for molecules to rearrange over time, affecting assay reliability and reproducibility. More advanced architectures have been developed to overcome these limitations, involving the controlled introduction of functional groups on the surface to allow for covalent coupling of the BRE (*104*, *105*).

Covalent coupling involves activating the surface with functional groups that can couple with reactive nucleophiles on the BRE. Carboxylic groups are commonly used for this purpose, and the carbodiimide reagent EDC is often utilized to create a reactive O-acylisourea group that can couple with amine groups. NHS is used as an ester-forming compound to stabilize the O-acylisourea intermediate before forming the covalent bond, and excess ethanolamine is added to block any remaining activated groups. Copper(I)-catalyzed 1,3-dipolar cycloaddition of azide and alkynes is another covalent coupling technique that is highly selective, fast, irreversible and provides a high yield. Other covalent coupling techniques involve coupling thiol groups to reactive groups like pyridyl disulfides, maleimide, and acyl halide derivates, or coupling aldehyde groups to amines and hydrazines (*15*, *104–106*).

Affinity interactions are commonly used in the immobilization of biosensing recognition elements (BREs). One popular method is the specific interaction between the Fc region of immunoglobulin (Ig)G antibodies and protein G or A, which allows the Fab variable regions to remain accessible for the efficient capturing of analytes(*15*, *107*). Avidin-biotin coupling is another widespread method that exhibits a non-covalent but high-affinity interaction, providing an oriented immobilization and high stability in harsh conditions (*108*).

This thesis concerns affinity biosensors, which rely on the ligand-binding interaction between the BRE and the analyte in an assay(*109*). Immunoassays, which are based on the unique properties of antibodies to bind to many natural and synthetic analytes with high specificity and strength, are the oldest type of assays(*110*). Antibodies can be classified into five main isotypes and can exist as monomers, dimers, and pentamers. B cell-derived polyclonal antibodies are a mixture of antibodies with different affinities and epitope binding sites, while monoclonal antibodies (MAbs) derived from a single parent cell have identical specificity (*109–111*).

In SPR biosensors with a direct assay format, the analyte is detected through a change of mass on the probed surface without further amplification steps(*112*). The signal generated by the transducer is directly proportional to the amount of analyte in the sample. However, in many instances, the signal generated through the mass change is not measurable, and the detection of the target analyte requires an additional enhancement step. This can be achieved through competitive, inhibition, or sandwich assay formats, based on the same analytical principles as enzyme-linked immunosorbent assay (ELISA) routinely used in labs(*15*, *105*, *110*, *113*, *114*). In

a sandwich format, the secondary molecule, such as an additional antibody, is bound to the analyte, which is captured by the BRE with another epitope(*109*, *113*). This additional mass change can lead to a stronger sensor signal than the analyte on its own. To further enhance the signal, the secondary molecule can be labeled with nanoparticles for even bigger mass changes or fluorophores for detection independently of mass changes on the surface (*15*, *110*, *113*).

The assay schemes of immunoassays can also be readily converted to other types of BREs. Not only monoclonal or polyclonal antibodies, but antibody fragments (Fc fragments, nanobodies), as well as whole (modified) cells, receptors, proteins, or nucleic acids, can serve as BREs (*105*, *109*). Biomolecules can be engineered to perform recognition does not present in nature, such as (oligo-) peptides, oligonucleotides, or aptamers, and synthetic materials can be used to mimic biorecognition, such as molecularly imprinted polymers (MIPs)(*109*, *115*, *116*).

In addition to SPR biosensors, graphene-based field-effect transistor (gFET) biosensors have also attracted significant attention in recent years (*117*, *118*). gFET biosensors offer high sensitivity, low limit of detection, and fast response times, making them suitable for a wide range of applications. Similar to SPR biosensors, the immobilization of BREs is critical for the performance of gFET biosensors. Various immobilization strategies have been developed for gFET biosensors, including non-covalent and covalent immobilization methods (*117*, *119*, *120*). Non-covalent methods such as electrostatic adsorption and π-π stacking are simple and easy to perform but can suffer from weak binding strength and loss of activity due to the random orientation of the immobilized molecules(*14*, *121*). Covalent methods such as amide bond formation, diazonium coupling, and thiol-ene click chemistry offer stable and permanent covalent linkages between the immobilized molecule and the graphene surface, leading to improved sensitivity and specificity(*86*, *121–123*). These strategies have been used to immobilize a variety of biomolecules, including proteins, DNA, and aptamers, onto the graphene surface of gFET biosensors. The choice of immobilization strategy depends on

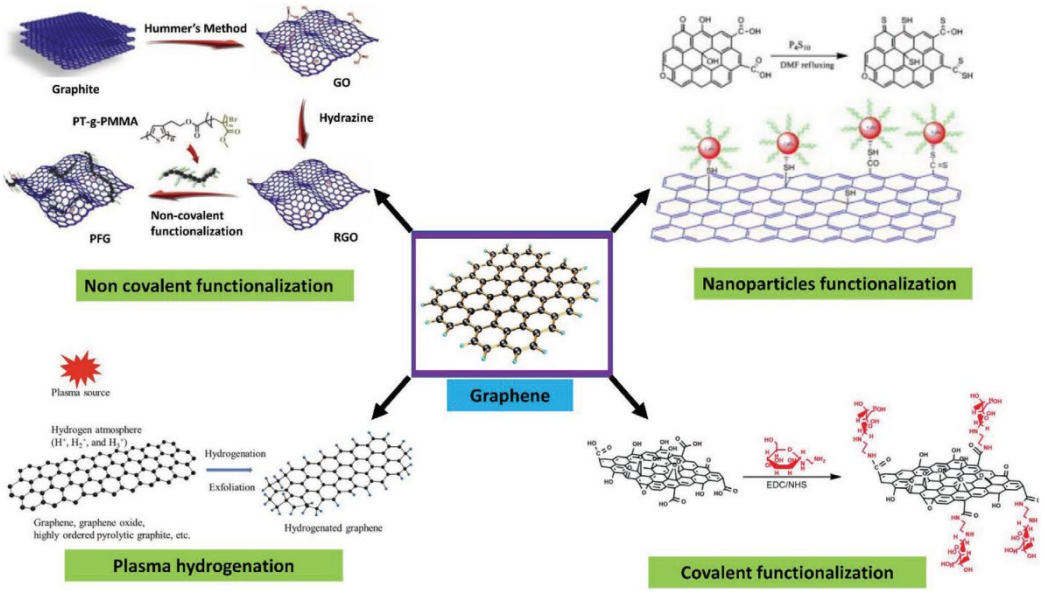

Figure 3 2 Schematic representation of functionalization strategies for graphene-coated surfaces. *(*124*)*

factors such as the type of biomolecule, the desired sensitivity and limit of detection, and the intended application of the biosensor.

Biosensors have emerged as powerful tools for a wide range of applications, from healthcare and environmental monitoring to food safety and biodefense (*125*). Continued development of new immobilization strategies, transducer materials, and BREs is likely to further enhance the performance and versatility of biosensors in the future. Advancements in biosensors have been driven by a number of factors, including the need for more sensitive and specific detection methods, the increasing demand for point-of-care diagnostics, and the growing interest in personalized medicine (*109*, *125*). Recent developments in nanotechnology, microfabrication, and biotechnology have created new biosensors with improved performance characteristics and expanded capabilities. For example, lab-on-a-chip technologies have been developed that enable multiple biosensors to be integrated onto a single chip, allowing for high-throughput and parallel analysis of multiple analytes(*125*, *126*).

One of the key challenges in the development of biosensors is the need to ensure their accuracy and reliability in real-world applications. Factors such as sample matrix effects, interference from other components in the sample, and non-specific binding can all impact the performance of biosensors(*18*). To overcome these challenges, a number of strategies have been developed, including the use of pre-treatment steps to remove interfering components, the use of control experiments to account for non-specific binding, and the use

of statistical analysis to determine the limit of detection and limit of quantification of the biosensor (*18*). The design and development of biosensors require careful consideration of the immobilization strategy, the choice of transducer material, and the selection of the appropriate biomolecular recognition element. With continued advancements in these areas, biosensors are likely to play an increasingly important role in healthcare, environmental monitoring, and other areas of research and development

4 Discussion

The collective body of work presented in this thesis provides substantial advancements in the realm of biosensor technology, with a particular emphasis on their applications within clinical diagnostics. Each paper within this thesis offers distinct, yet interconnected insights, methodologies, and findings, contributing to a holistic understanding of the potential and limitations of current biosensor technology.

The first study sets the stage by addressing a crucial component in biosensor technology—the substrate material. Here, the focus is on the use of reduced graphene oxide (rGO), a versatile material with exceptional electronic properties, making it an excellent candidate for biosensing applications. However, to fully leverage the unique properties of graphene, a robust and repeatable deposition method is needed. In this study, an optimized protocol for the deposition of rGO on silica-based substrates is presented. This method, which involves spin coating with a 214 µg/mL GO solution at 1800 rpm, was meticulously developed, considering the effects of graphitic structures and intercalation on surface morphology.

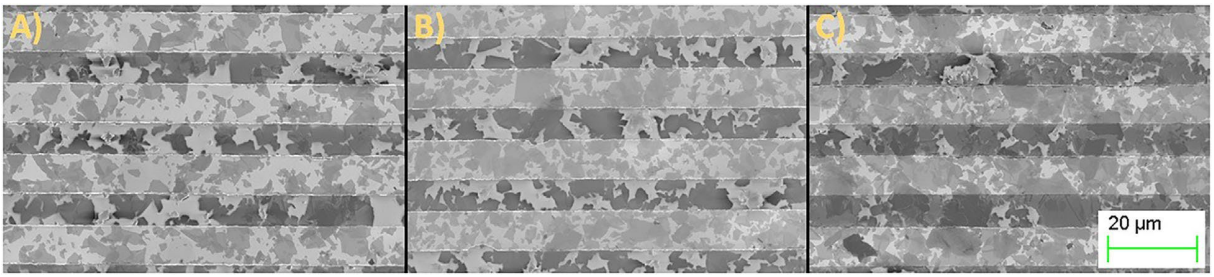

Figure 4 1 SEM image comparison of three different spin coating speeds for a 214 µg/mL GO solution. A) 2100 rpm B) 1800 rpm C) 1500 rpm. All images were recorded at 1000× magnification

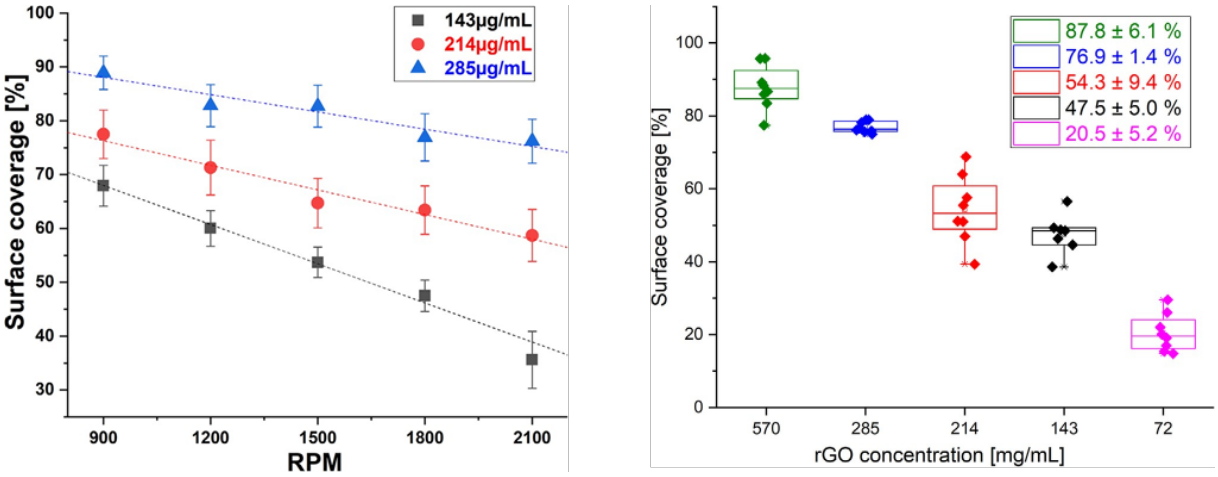

Figure 4 2 A) Dependence of the fabricated device surface coverage on the spin coating rpm for different GO concentrations, B) Reproducibility of surface coverage for 8 fabricated devices for different GO concentrations with a spin coating speed of 1800 rpm

In the initial study, Scanning Electron Microscope (SEM) images of a surface deposited with a spin coating of 214 µg/mL at 1800 rpm revealed the presence of approximately 105 parallel connections across the entirety of the fabricated Field-Effect Transistor (FET). It was inferred that the total resistance of the FET would be lower than the resistance of the most conductive connection, thereby indicating that the majority of current flow would be observed at that connection. This is a pivotal observation for many applications, emphasizing the importance of fabricating devices where the least resistant connection is composed of the material of interest - in this case, reduced Graphene Oxide (rGO). Consequently, it became critical to minimize the number of graphitic structures. This was achieved in the study through a carefully tailored process involving centrifugation and the selection of appropriate spin-coating parameters. The implemented modifications significantly bolstered the reproducibility and stability of electronic devices, including biosensors, thereby setting a new industry standard for the fabrication of GO or rGO-based devices. These advancements not only contribute to the existing body of knowledge but also lay a robust foundation for future exploration and development in the realm of biosensor technology, especially those utilizing graphene substrates.

The second paper advances this narrative by developing a novel immunoassay that leverages a single monoclonal antibody in conjunction with surface plasmon field-enhanced

fluorescence spectroscopy (SPFS) for the sensitive detection of cardiac troponin I (cTnI). cTnI, a pivotal biomarker in cardiovascular disease diagnosis, can indicate conditions like myocardial infarction if detected early. However, the regular SPR biosensor principle didn't offer sufficient sensitivity for cTnI analysis at clinically relevant concentrations. By implementing the SPFS mode in the same instrument, the sensitivity of the detection process saw significant improvement. This innovative approach allowed for the successful development of an assay with a limit of detection (LoD) of 19 pM within a 45-minute detection timeframe, presenting a reliable and efficient diagnostic tool for detecting cTnI at clinically relevant concentrations.

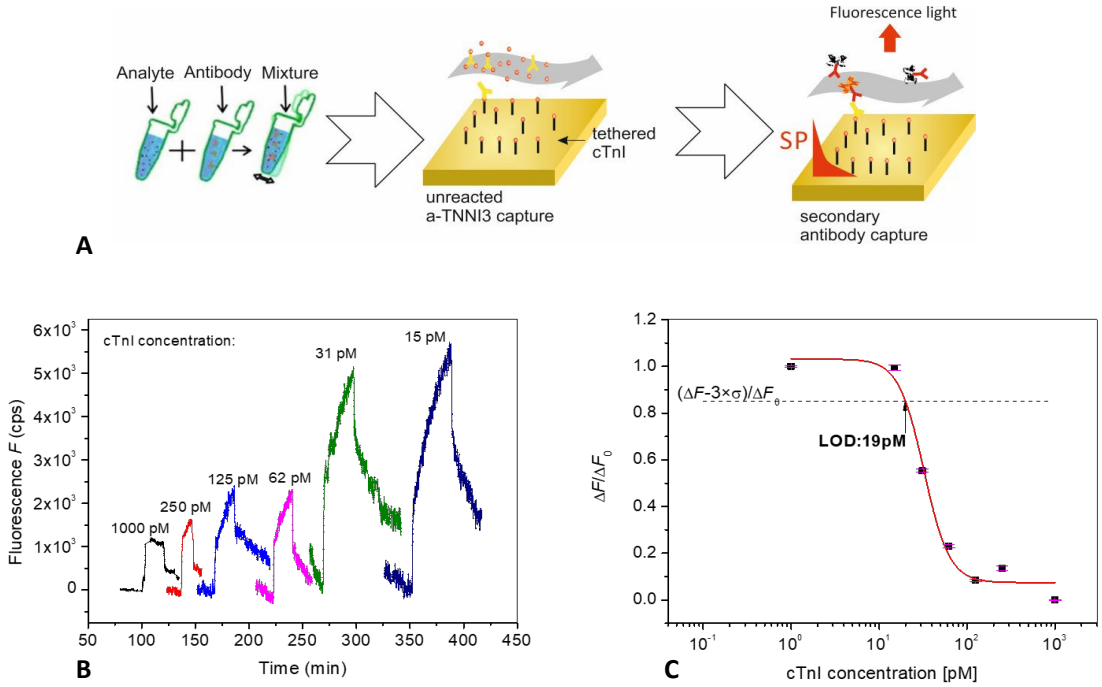

Figure 4 3 (A) A schematic of the inhibition-competitive assay steps, (B) fluorescence signal kinetics measured upon the binding of the secondary antibody conjugated with Alexa Fluor 647 and varied concentrations of cTnI, and (C) normalized calibration curve of the SPFS biosensor with an indicated LoD of 19 pM

The third paper leverages cTnI as a reference system, extending the application of this key biomarker beyond the realm of cardiovascular disease diagnosis. The objective was to calibrate a broad range of transducer concepts and experimental setups, an endeavor aimed at improving the versatility of biosensor technology. In order to explain why it is so important to generate this model- based understanding of the molecular interactions on the sensor surface, we refer to our own work and summarize in the following experimental binding data that were collected by i) surface plasmon fluorescence spectroscopy, by ii) an electrochemical

technique, i.e., differential pulse voltammetry, and by the most recent methodological developed in our laboratories, i.e., iii) an electronic read-out concept based on graphene field-effect transistors (gFETs). This study reinforces the importance of considering factors beyond simple detection limits, such as operational simplicity, robustness of test kits, and cost-effectiveness, for real-world applicability.

One of the example we presented that was using differential pulse voltammetry and [Fe(CN)6]4- as a redox mediator, an aptamer was employed as a receptor for cTnI binding. The key discovery was that electron transfer, crucial in electrochemical systems, is hindered upon interaction between cTnI and the aptamer due to probable diffusion restriction. With a detection limit as low as 0.88 pg mL-1 in PBS and 1 pg mL-1 in saliva, this technique presents a compelling alternative to other methods. Its simplicity and portability make it an attractive option for point-of-care testing (POCT).

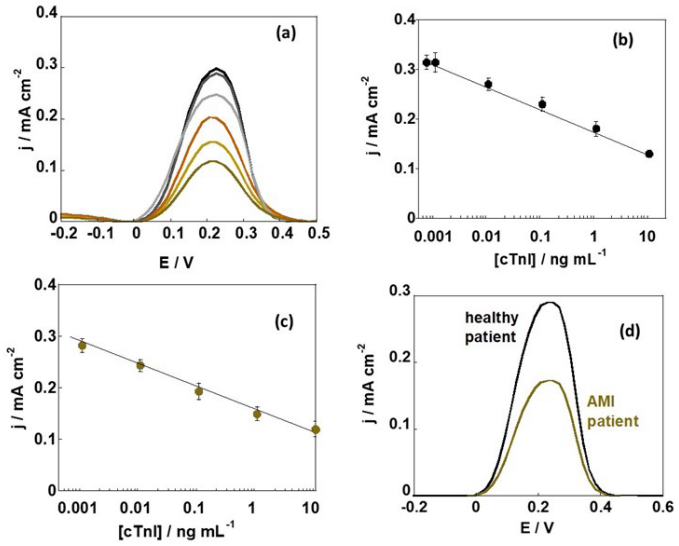

Figure 4 4 (a) Differential pulse voltammograms at various cTnI concentrations (0, 0.001, 0.01, 0.1, 1 and 10 ng mL-1) in PBS ×1 (pH 7.4). (b) Calibration curve in PBS ×1 (pH 7.4). (c) Calibration curve for cTnI in human saliva samples spiked with different concentrations of cTnI. (d) DPV curves in saliva of patient samples with chest pain and diagnosed AMI and healthy ones as controls.

Last example of this study was conveyed in analyzing the shift in the source-drain current, IDS, held at a constant gate voltage of VG = 350 mV as correlated with the variable concentration of cTnI, a pattern suggestive of traditional binding behaviors was detected. At low cTnI concentrations, a linear growth of current with concentration was observed, which eventually

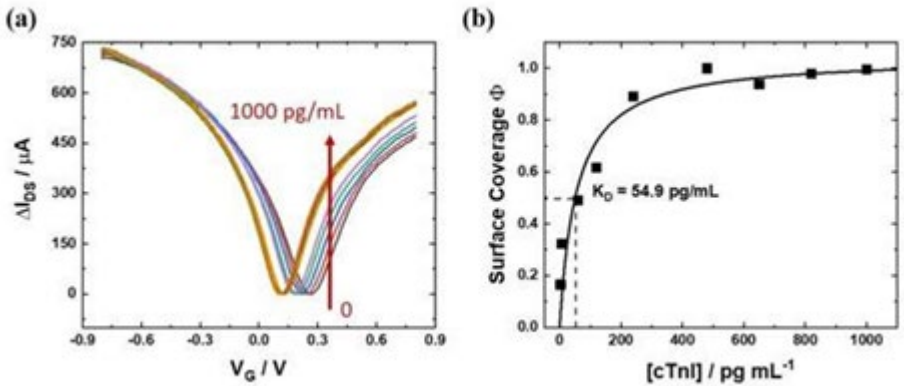

Figure 4 5 (a) Graphene transfer characteristics (ΔIDS-vs-VG curves) after stabilization with each cTnI concentration (0, 3, 6, 60, 120, 240, 480, 650, 820 and 1000 pg mL-1) in 0.01x PBS (pH 7.4) without washing steps. (b) ΔIDS, converted according to the Langmuir model to the corresponding surface coverage, Φ, as a function of the analyte concentration of the solution running through the flow cell.

transitioned into a saturation phase when the cTnI concentrations rose higher (as depicted in Figure 4 4(b)). Postulating a Langmuir binding model to explain these observations, the data points could be accommodated by fine-tuning the dissociation constant, which was determined to be Kd = 55 pg mL^{-1}, equivalent to approximately 2.5 pM. This denoted an impressively high affinity of the aptamer, functioning as a receptor in the bio-affinity reaction, and lays a solid foundation for designing an incredibly sensitive assay for use in medical diagnostic applications.

Lastly, the use of covalent surface modification strategies in Graphene Field-Effect Transistors (gFETs) with nanoscale affinity entities such as aptamers has recently emerged as an nnovative approach, proving to be notably superior to noncovalent functionalization techniques. The covalent grafting of specific binding molecules produces surfaces that are both stable and robust, establishing the potential for versatile and cost-effective biosensing devices. In this fourth study, we demonstrate the application of polyclonal aptamer libraries targeting the two isoforms of retinol-binding protein 4 (RBP4) for the functionalization of gFETs, effectively discerning retinol-loaded or unloaded RBP4. It is notable that unloaded RBP4 is an underutilized marker in the progression of diabetes, and hence, the biosensor developed in this work not only presents a valuable tool for early diabetes diagnostics but also exemplifies

the potency of aptamers as highly sensitive sensing interfaces for GFET-based sensors in prospective sensing diagnostic platforms, including clinical settings.

The straightforward nature of library evolution and the efficiency of covalent chemical grafting onto graphene layers, in conjunction with GFETs, pave the way for these electronic devices to become standard sensors for an extensive array of applications. This includes critical areas like medical diagnostics and environmental health monitoring, thereby transforming the landscape of biosensing technologies. the study was able to discriminate between RBP4 isoforms at physiologically relevant concentrations ranging from 0.3 to 30 nM. The use of polyclonal aptamer libraries enables a diverse and specialized range of binding aptamers, adding an extra layer of specificity and versatility to the sensing and quantification of target

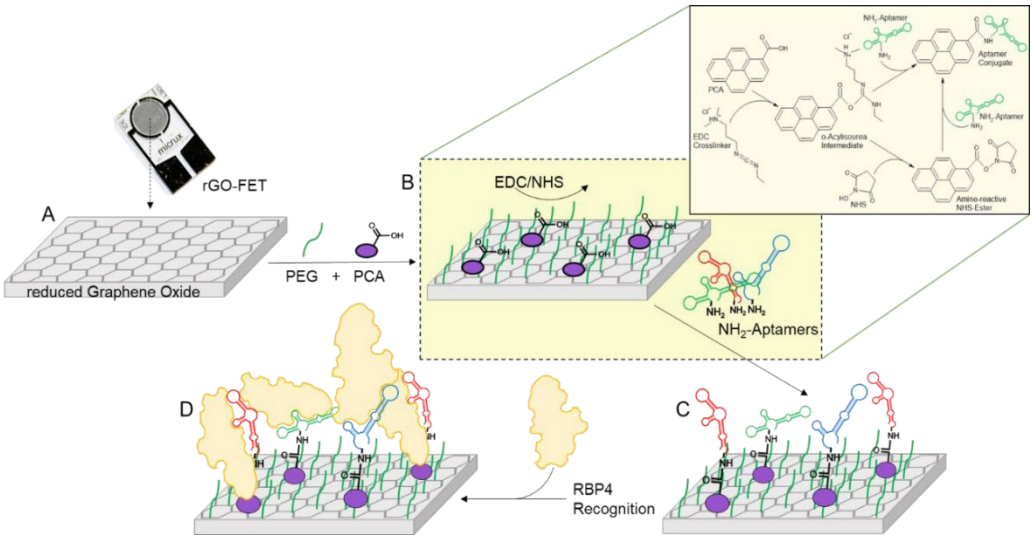

Figure 4 4 Functionalization of rGO-FETs with polyclonal ssDNA aptamer libraries and specific apo- or holo-RBP4 detection. A) The rGO-FET were immersed into a mixture of PyPEG (PEG pre-conjugated with a PBSE) (500 µM) and 1-pyrenecarboxylic acid (PCA, 50 µM, linker) in DMSO for 12 h at room temperature to obtain a 10:1 ratio of blocking and linking agents on the biosensor's surface. B/C) Apo- or holo-RBP4 aptamer library immobilization by first activating the carboxyl groups by immersion into a solution of EDC (15 mM)/NHS (15 mM) in 150 mM PBS solution for 30 min, followed by covalent coupling of the 5'-NH2- modified aptamer (100 nM in milliQ grade water for 40 min at 25 °C).D) Specific affinity recognition of either apo- or holo-RBP4 by the on rGO-FET immobilized polyclonal ssDNA aptamer libraries in electrical measurements.

molecules. This paper shines a spotlight on the possibility of developing novel, highly specific electronic sensors, providing a promising avenue for research in clinical diagnostics.

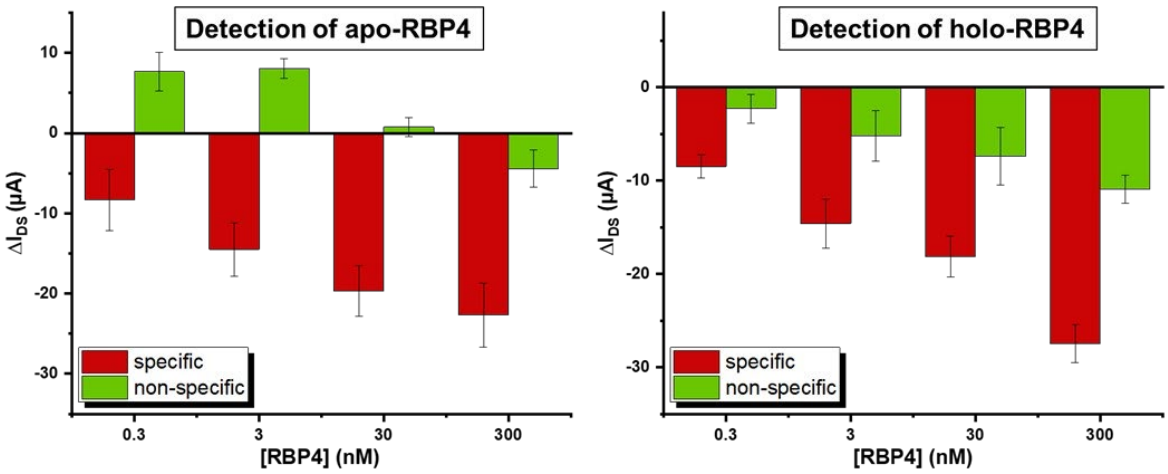

Figure 4 5 Average difference in current at -0.4 V upon addition of increasing concentrations of RBP4. Δ-values shown are averages of a minimum of three independent experiments on different devices. Error bars show the standard deviation

The thematic interconnectedness of these studies demonstrates the intricate nature of biosensor research, addressing the multifaceted challenges of the field, from the intricacies of materials science and deposition techniques to the nuanced utilization of antibodies and transducer concept calibration. It emphasizes the potential for a truly interdisciplinary approach to advance the field of biosensor technology. The conclusion drawn from these collective works is the potential and need for continuous innovation in biosensor technology, with the ultimate aim of enhancing clinical diagnostics and patient outcomes. Thus, this thesis serves as both an exploration and a catalyst for further research, underscoring the potential of biosensor technology in the realm of disease diagnosis and management.

5 Research Aims

The principal aim of this study is to underscore and substantiate the criticality of assay development in the context of biosensor technology, with an end goal of achieving superior sensitivity and selectivity in the diagnostics process. With an estimated 17.9 million deaths each year, cardiovascular diseases (CVD) are the leading cause of death worldwide, according to the World Health Organization. In order to improve patient outcomes, early CVD diagnosis and treatment are essential, and biosensors can significantly contribute to this effort. Similarly, to obesity, which affects an estimated 463 million individuals around the world, diabetes is a significant public health issue. To avoid complications such as kidney failure, which is the leading cause of end-stage renal disease in the world, early diagnosis and

management of diabetes are crucial. To improve the diagnosis and treatment of these disorders, it is crucial to develop biosensors for the detection of biomarkers such as cTnI and RBP4.

The development and use of various sensing technologies for the detection of biomarkers are discussed in the four papers that follow, with a particular emphasis on cardiac troponin I (cTnI) as an example. The first paper describes the quick detection of cTnI, a crucial biomarker for the diagnosis of myocardial infarction, using an immunoassay in conjunction with surface plasmon fluorescence spectroscopy (SPFS). The second paper describes the use of oligonucleotide DNA aptamers for the detection of loaded and unloaded retinol binding protein 4 (RBP4), which is an essential biomarker for the prediction of diabetes and kidney disease. The third study examines the use of antibodies and DNA aptamers as receptors and provides a comprehensive list of examples from the literature of several sensing approaches for cTnI detection, including surface-plasmon optics, electrochemical assays, and gFETs. The fourth paper addresses the production of electronic devices, including biosensors and electrical circuits, using reduced graphene oxide (rGO).

The creation of sensitive and focused biomarker detection technologies is the unifying objective of the four investigations. These research uses various receptors, such as antibodies and DNA aptamers, as well as various sensing technologies, such as surface-plasmon optics, electrochemical assays, and graphene field-effect transistors. The investigations also use several sample types, such as PBS buffer and clinical saliva samples, as well as various substrate materials, such as gold, graphene, and reduced graphene oxide. The research underscores the necessity of developing sensitive and selective detection methods for biomarkers, as these can provide valuable diagnostic information for different diseases, including myocardial infarction, diabetes, and renal disease. Many detection techniques that can be adapted to particular applications and sample types have been developed, thanks to the use of various sensing technologies and receptors. In addition, the utilisation of different substrate materials and sample types allows the evaluation and comparison of different detection methods under varied circumstances. To continue to improve the sensitivity, selectivity, and adaptability of biomarker detection methods, more research is necessary in this field. The development of such approaches can have a substantial impact on the diagnosis and treatment of diseases.

6 Individual Studies

In recent years, biosensors have made significant advancements in clinical diagnostics due to their sensitivity, specificity, and ease of use. Four studies contribute to this progress: (1) an optimized deposition protocol for rGO on silica-based substrates, improving reproducibility and stability in electronic devices; (2) a troponin cTnI immunoassay using a single monoclonal antibody and surface plasmon field-enhanced spectroscopy (SPFS) detection, providing a reliable diagnostic tool for detecting cTnI at clinically relevant concentrations; (3) the recognition that the limit of detection (LoD) is not the only factor to consider when selecting detection concepts for clinical applications, emphasizing the importance of ease of operation, test kit robustness, and cost; (4) the use of focused polyclonal aptamer libraries for improved performance in sensing and quantification of target molecules, enabling rapid, cost-effective development of highly specific electronic sensors for clinical diagnostics. These studies offer promising avenues for further research and development in the field of biosensors for clinical diagnostics, ultimately contributing to improved patient care and outcomes.

6.1 Top performer: Towards optimized parameters for reduced graphene oxide uniformity by spin coating

Ciril Reiner-Rozman, Roger Hasler, Jakob Andersson, Teresa Rodrigues, **Anil Bozdogan**, Johannes Bintinger and Patrik Aspermair. The top performer: towards optimized parameters for Reduced graphene oxide uniformity by Spin coating. *Micro Nano Lett.* 16, 436– 442 (2021). https://doi.org/10.1049/mna2.12070

Co-authorship paper:

I conducted experiments for optimisation of the produced graphene coated chip, did data analysis, and was involved in the discussion, manuscript preparation, and SEM image design. CRR was responsible for concept and manuscript preparation and was involved in imaging, data analysis and experimental design. RH, TR were involved in experimental design, production, data analysis and manuscript preparation. JA, JB and PA were responsible for project design, discussion, and manuscript preparation.

Reduced graphene oxide enables simple deposition techniques for electronic device fabrication, such as biosensors and electric circuits. Optimal film characteristics and electronic properties are achieved using 214 µg/mL graphene oxide concentration, applied via spin coating at 1800 rpm after surface modification with an adhesive layer.

Received: 17 August 2020 | Revised: 3 March 2021 | Accepted: 10 March 2021

Micro & Nano Letters

DOI: 10.1049/mna2.12070

The Institution of Engineering and Technology WILEY

ORIGINAL RESEARCH PAPER

The top performer: Towards optimized parameters for reduced graphene oxide uniformity by spin coating

Ciril Reiner-Rozman[1,2] | **Roger Hasler**[1] | **Jakob Andersson**[1] | **Teresa Rodrigues**[1] | **Anil Bozdogan**[3] | **Johannes Bintinger**[1,2] | **Patrik Aspermair**[1]

[1] Biosensor Technologies, Austrian Institute of Technology, Konrad-Lorenz Strasse 24, Tulln an der Donau 3420, Austria

[2] Danube Private University, Steiner Landstraße 124, 3500 Krems an der Donau

[3] CEST Kompetenzzentrum für elektrochemische Oberflächentechnologie GmbH, Viktor Kaplan Straße 2, Wiener Neustadt 2700, Austria

Correspondence
Ciril Reiner-Rozman, Biosensor Technologies, Austrian Institute of Technology, Konrad-Lorenz Strasse 24, Tulln an der Donau 3420, Austria.
Email: Ciril.Reiner-Rozman@ait.ac.at

Funding information
H2020 Marie Skłodowska-Curie Actions, Grant/Award Number: 813863; Österreichische Forschungsförderungsgesellschaft, Grant/Award Numbers: 870025, 873541

Reduced graphene oxide has shown great potential for the fabrication of different electronic devices, especially biosensors and electric circuits. It allows the usage of simple deposition techniques such as drop casting or spin coating of graphene oxide solutions with a subsequent chemical, electrochemical, and/or thermal reduction to reduced graphene oxide. However, the utilized deposition strategy requires a defined protocol that ensures reproducibility. A study on a range of concentrations of GO and spin coating parameters is presented, aiming at the most uniform layers consisting of only single and double sheets for the application in electronic devices. The effect of film deposition on morphological parameters like the number of layers, overlaps, and surface coverage as well as the influence on electronic properties such as baseline stability and the transfer characteristics for the application as an electrolyte gated field-effect transistor (EG-FET) are shown. Best film characteristics and electronic properties are achieved by using a GO concentration of 214 μg/mL applied via spin coating with 1800 rpm, after surface modification with adhesive layer.

1 | INTRODUCTION

Since its first isolation by mechanical exfoliation in 2004, graphene has increasingly captured attention as a novel nanomaterial [1]. It has become a crucial component in a variety of electronic applications [2] due to its unique properties. Several methods have been developed that can produce high-quality graphene, however 'chemical vapour deposition (CVD)' and reduction of graphene oxide are considered the most suitable to obtain graphene with high carrier mobility and low defect density. While graphene produced via CVD typically has large area uniformity with high electric and morphological reproducibility [3, 4], the production is very time and energy consuming and has low yields [5] compared to graphene obtained via reduction of graphene oxide. This method produces high yields but is generally perceived by the research community to produce graphene with less favourable properties for most applications and inferior homogeneity when compared to the pristine, CVD-grown material. 'Reduced graphene oxide (rGO)' is prepared via the reduction of graphene oxide by thermal, chemical or electrical treatments. Even after reduction, it retains some oxygen functional groups (hydroxyl, epoxide, carbonyl and carboxyl groups) on the rGO surface. Different carbon to oxygen ratios and chemical compositions are obtained depending on the reducing agent. This can be exploited since rGO can be modified depending on the functional groups it contains, whereas CVD graphene cannot. Moreover, despite CVD resulting in self-limiting graphene formation on top of a metal surface with excellent step coverage [3], graphene deposition is followed by a transfer process to the desired substrate and removal of the metal by an etching agent which is a crucial step that is susceptible to human error. As such, despite the uniformity, the transfer process is a major disadvantage when using CVD-grown graphene. On the other hand, graphene oxide (GO) is directly deposited on the desired substrate and then reduced, which simplifies device production and eliminates a significant source of error. The use of reduced graphene oxide (rGO) simplifies device fabrication and can be used for bulk manufacturing but allows lower control over flake morphology and defect distribution as well as the chemical properties since the reduction

cannot remove all structural defects introduced by the oxidation process. A further issue is the coagulation of rGO in solution, which leads to graphitic structures. As a result, the reproducibility during the fabrication of electronic devices will be compromised. In literature, GO is most commonly deposited on the substrate by drop casting, resulting in low reproducibility of surface morphology. On the other hand, spin-coating of GO offers a cost- and time-efficient alternative for the fabrication of uniform films; it is a less prominent but nevertheless established method for the fabrication of electronic devices [6, 7] including solar cells [8], electrodes [9], transistors [10], memory devices [11], membranes [12] and biosensors [13, 14]. Although this method has been widely used since the development of graphene films, only few publications investigate the outcomes of GO concentration and spin coating parameters on the electrical and morphological properties of the resulting devices. In this communication, we demonstrate significantly improved reproducibility of graphene film morphology and electrical properties using an optimized spin-coating deposition and handling strategy. We present a study on a range of concentrations of GO and spin coating parameters to produce uniform layers consisting of only single and double sheets for the application in electronic devices. We show the effect of film deposition on morphological parameters like number of layers, overlaps and surface coverage as well as the influence on electrical properties such as baseline stability and the transfer characteristics for the application as an 'electrolyte gated field-effect transistor (EG-FET)' based on rGO.

2 | MATERIALS AND METHODS

ED-IDE1-Au (w/o SU8) with interdigitated electrodes (split with 10 μm, channel length 490 mm) were purchased by Micrux Technologies and used as substrates. The substrates were cleaned with a 1% Hellmanex II aqueous solution in an ultrasonication bath for 15 min, rinsed with Milli-Q grade DI-H_2O and sonicated for 15 min in DI-H_2O, rinsed with ethanol and sonicated for 15 min in ethanol. '(3-Aminopropyl)triethoxysilane (APTES)' was obtained from Sigma-Aldrich and used as adhesive layer for GO deposition. The clean substrates in ethanol were directly transferred and submerged for 1 h at room temperature in a 1% APTES solution, prepared in HPLC grade ethanol, covered for protection against UV-light. The substrates were then thoroughly rinsed with HPLC grade ethanol and dried with N_2 gas until complete dryness. The substrates were then heated to 120 °C for 1 h and left to cool down to room-temperature. Highly concentrated GO was purchased from Graphenea (0.4 wt%) and dilutions were prepared with Mill-Q grade DI-H_2O to obtain dilutions of 1:7, 1:14, 1:21, 1:28, 1:56 corresponding to 0.059, 0.029, 0.019, 0.014 and 0.007 wt% or 570, 285, 214, 143 and 72 μg/mL of GO in solution. Prior experiments were conducted to find this range of GO concentrations suitable for application via spin-coating. The GO stock solution was vortexed for 30 s using a VWR analogue vortex mixer at highest speed before preparation of the dilutions. To eliminate any graphene conglomerates from the solution, resulting dilutions were transferred to Eppendorf vials (1 mL) and centrifuged for 20 s. For deposition on the substrates only the top portion of the resulting solutions was used for spin-coating. During the performed studies it was observed that correct positioning of the substrate on the spin-coater is critical to obtain optimal GO distribution. The devices were placed slightly off-centre, in such a manner that the rotational axis during spin coating is offset from the interdigitated area by 1 mm, omitting weakly covered spots at this axis. The prepared GO solutions were drop cast on the previously positioned substrates only a second before starting the spin-coater rotation. For the spin coating process, the steepest possible ramp (0 s) was chosen and the rotation speed of 900, 1200, 1500, 1800, 2100 was held constant for exactly 60 s. When finished, the coated substrates were immediately removed and submerged in Milli-Q grade DI-H_2O to stop any further adhesion from the solution. Each substrate was then washed with DI-H_2O and dried with nitrogen again. The described steps were performed consecutively without time gaps. The obtained GO-coated substrates were then reduced in reagent grade hydrazine monohydrate vapour (98%, Sigma-Aldrich) at 80 °C for 16 h. For this, the substrates were placed centred in glass petri-dishes and 1 mL of hydrazine was distributed concentrically around the edge of the dish, followed by immediate hermetical sealing of the petri-dishes and inserting them in the oven. After 16 h, the substrates were cooled to room temperature and the seal was opened, allowing any excess hydrazine vapour to evaporate for 1 h. The substrates were then heated to 200 °C for a thermal annealing step, after which the substrates were ready to use for characterization with a 'scanning electron microscope (SEM)' (Zeiss SUPRA 40 Field Emission Scanning Electron Microscope) and consecutively for electrical characterization using a Keithley 4200-SCS probe station. For the electrolyte-gated configuration of the transistors a flow cell with 2 mm channel width and an Ag/AgCl gate electrode was used, enabling real-time flow measurements of the device baseline drift. Upmost attention was payed to the connection via BNC Triax cables, reducing any eventual noise not originating from the substrates, which in this state already were used as EG-FETs. To evaluate the device baseline drift, all sensors were rinsed with 1× PBS buffer solution in the flow-cell setup for exactly 10 min before their baseline was recorded with an applied source-drain voltage of 50 mV, applying a −400 mV potential at the gate electrode. After that the $I_D V_G$ transfer characteristics were recorded. All experiments were performed with 300 μL/min PBS buffer flow speed.

3 | RESULTS

The devices were investigated with a SEM and the images were evaluated using ImageJ software to determine the rGO surface coverage on the substrates. This procedure is described in detail in the Supporting Information. Figure 1 shows the difference in spin coating rpm in the range from 1500 to 2100 for a GO solution with 214 μg/mL. Surface coverages of these substrates increase with lower rotation speeds during spin coating. This is

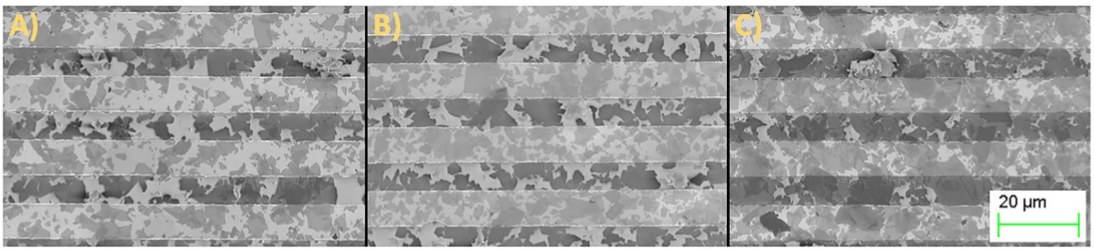

FIGURE 1 SEM image comparison of three different spin coating speeds for a 214 μg/mL GO solution. A) 2100 rpm B) 1800 rpm C) 1500 rpm. All images were recorded at 1000× magnification

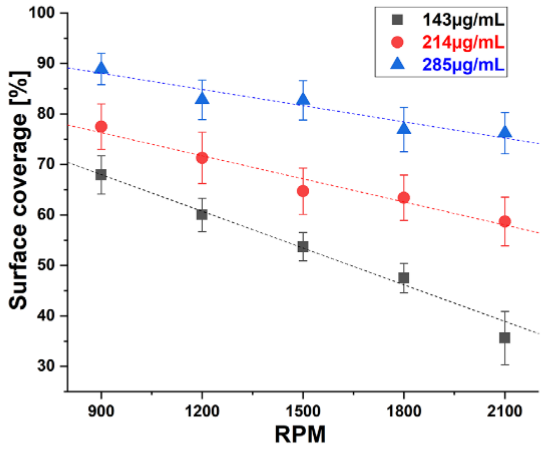

FIGURE 2 Dependence of the fabricated device surface coverage on the spin coating rpm for different GO concentrations

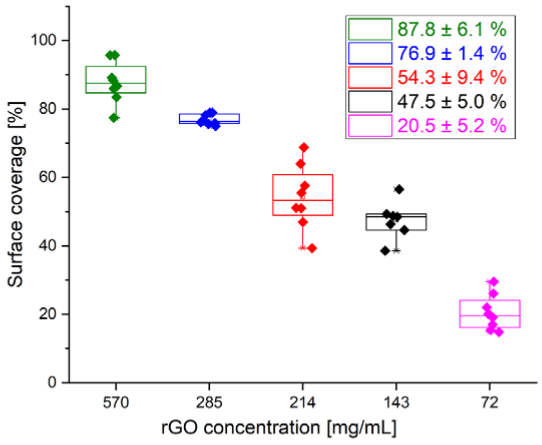

FIGURE 3 Reproducibility of surface coverage for 8 fabricated devices for different GO concentrations with a spin coating speed of 1800 rpm

a result of higher centrifugal forces during deposition and hence less surface contact and incubation time of the GO solution on the substrate. In detail, 2100 rpm resulted in 63% surface coverage, 1800 rpm in 76% and 1500 in 89%. In Figure 2, the surface coverages obtained for the selected ranges of dilution and spin coating parameters are shown. Interestingly, surface coverage depends linearly on GO concentration, while the relationship between spin coating speed and surface coverage density is also linear for a narrow RPM regime (as shown in Figure 2) but is more complicated for very high or low RPM number. Taking the standard error during device fabrication into account, the results shown in Figure 2 show a clear difference for speeds of 900 and 1200 rpm with higher coverages, while for higher rpm numbers from 1500 to 2100, surface coverage is similar. On the other hand, for the 8 devices fabricated with each of the parameters, the statistical evaluation shows the smallest standard error for 1800 rpm, (1.4%, shown in Figure 3) while 2100 and 1500 rpm devices varied by 2.5% and 2.3%, respectively. Hence, the decision was made to use 1800 rpm deposition speed with a GO concentration of 285 μg/mL for electrical characterization. It must be noted that a higher GO concentration (e.g. 570 μg/mL) with a higher rotation speed (e.g. 2500 rpm) might produce a similar result, but we did not evaluate these parameters. In general, we suspect that plotting the coverage versus the rpm and concentration as shown in Figure 2 for a wider range than shown here may well result in a linear ideal regime to obtain a morphology close to a monolayer where either the concentration and rpm are lowered or both parameters are increased, but in the work presented here, the relationship was not characterized to this extent.

As shown in Figure 3, the surface coverage reproducibility is better (standard error of 1.4%) for devices that have higher coverage due to the application of higher GO concentration (in this case 285 μg/mL) than for devices that have lower coverage due to a lower concentration of GO (214, 143 and 72 μg/mL) applied. This is expected if we take into consideration the extrapolated case of total surface coverage, with the whole surface being coated there is less variability in the production from device to device. On the other hand, Figure 3 gives no information about the quantity of multilayer structures, but as can be seen from Figure 1, the used concentrations and rotation speeds for spin coating were optimized beforehand to minimize the formation of multilayers and achieve surfaces with few overlaps of the rGO flakes to minimize the effects of intercalation of water molecules between those layers.

Interestingly, the GO distribution on the surface was found to vary depending if either a substrate with interdigitated electrodes or blank Si/SiO_2 substrates were used, although

in both cases the surface was modified with APTES and the fabrication was done using the same protocols. For the highest concentration of 570 μg/mL, the evaluation of multilayers was estimated via the SEM images and an estimated 50% or more of the device areas were found to be covered with at least 2 layers (Supporting Information). We expect that this originates from the uneven topology of the electrode surface with a few nm height profiles, where during the spin coating process the GO sheets stagger and form more overlaps in comparison to the deposition on blank substrates. Another aspect is the generally different smoothness of the used substrates, since the used Si/SiO_2 wafers are fabricated to produce ultra-low roughness while the commercially available devices with electrodes are manufactured with focus on the electrode precision and not on the substrate smoothness. Substrate roughness may also increase during the etching process required for electrode fabrication.

During the development of the protocols and tests for this study, we also examined the influence of graphitic structures on the topography and electronic performance. When applying GO via drop casting, the incubation time was always set to one hour, which is a significant amount of time during which graphene layers might agglomerate, forming graphitic structures. This could be avoided by varying the incubation time as well as the GO concentration used during drop casting. Still, for all variations of these parameters that were tested preceding this study, no suitable parameters were found to accurately control the surface coverage reproducibility and to avoid the formation of multilayered structures. In general, a major concern regarding graphitic structures is the instability of the attachment, since only relatively weak van der Waals forces hold multilayered structures together, resulting in significant variation in layer-to-layer distance. This also allows for the intercalation of molecules, especially ions, which can affect the electrical properties of the device as well as impurities, which are by definition a disadvantage of using rGO. Impurities have the most significant impact on sheet properties when located at the transition from one rGO flake to another, as they have the largest impact on percolation pathways in these locations. Furthermore, multilayers and graphitic structures may cause an ablation of a future surface functionalization or a signal attenuation of a binding event taking place on a recognition unit attached to such structures. Despite these disadvantages, the quick applicability and mass production capabilities or rGO are superior to perfectly uniform produced CVD graphene which does not suffer from multilayer formation and the associated deterioration in device properties.

Another advantage of rGO is the modified bandgap in comparison to CVD graphene. CVD graphene is a zero gap semi-metal, which makes the on–off ratio of graphene field effect transistors very low (<10) compared to conventional CMOS technologies, where ratios exceeding 10^7 are commonly achieved. As such, there have been some efforts to open the bandgap of graphene using different bandgap engineering techniques, such as using bilayer graphene or graphene nanoribbons [15]. Contrariwise, rGO resulting from most synthesis methods is a semiconducting material, exhibiting a significant gap

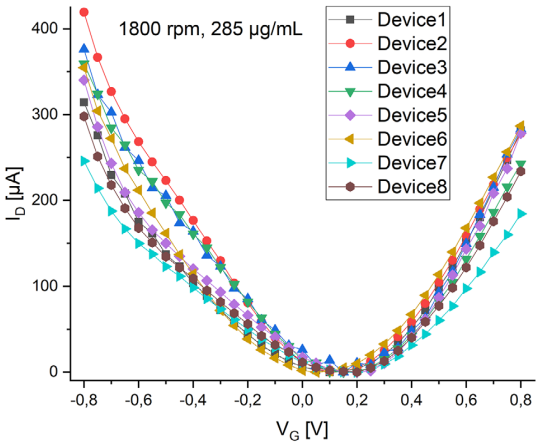

FIGURE 4 $I_D V_G$ reproducibility of eight FETs fabricated with 1800 rpm and 285 μg/mL GO solution. The I_{DS} currents of the used chips were subtracted from their Dirac point (minimum) respectively for better visual comparison

from the valence to the conduction band with a lower density of states than CVD graphene. High variations resulting from different methods of production of rGO regarding the chemical properties and defects, e.g. carbonyl, epoxy or hydroxyl [16] as well as the oxidation state depending on the used reduction method [17] have been reported. The reduction method significantly influences the semiconducting properties of the resulting films. However, commercial sources of GO are available that offer high reproducibility in terms of chemical surface features. Regardless, the application of such GO solutions requires a defined protocol to optimize reproducibility.

For the electrical evaluation of the EG-FETs, the transfer characteristics were measured (Figure 4) and the baseline drift was evaluated after initial stabilization for a period of ten minutes (Figure 5).

The basic relationship describing the measured drain-source current for an EG-FET is given by the following equation:

$$I_{DS} = W/L\, C_i\, \mu \left[V_{GS} - V_T\right] V_{DS} \tag{1}$$

where I_{DS} is the drain-source current, W the channel width, L the channel length, C_i the capacitance of the system in respect to the ionic liquid, μ the charge carrier mobility in the semiconductor channel, V_{GS} the applied Gate voltage, V_T the threshold voltage and V_{DS} the applied voltage from source to drain. This basic equation does not explicitly consider any chemical reactions between the buffer solution and rGO. Instead, these effects are described implicitly by V_T and C_i since these parameters are obtained from the properties of the device with regard to its current state at observation. As can be seen in Equation (1), the capacitance and the mobility of the FET have a significant impact on the transconductance and I_{DS} current of the device and since these parameters are altered by the formation of multilayers and the topography in general, the application method has impact on the FET performance. Furthermore, it

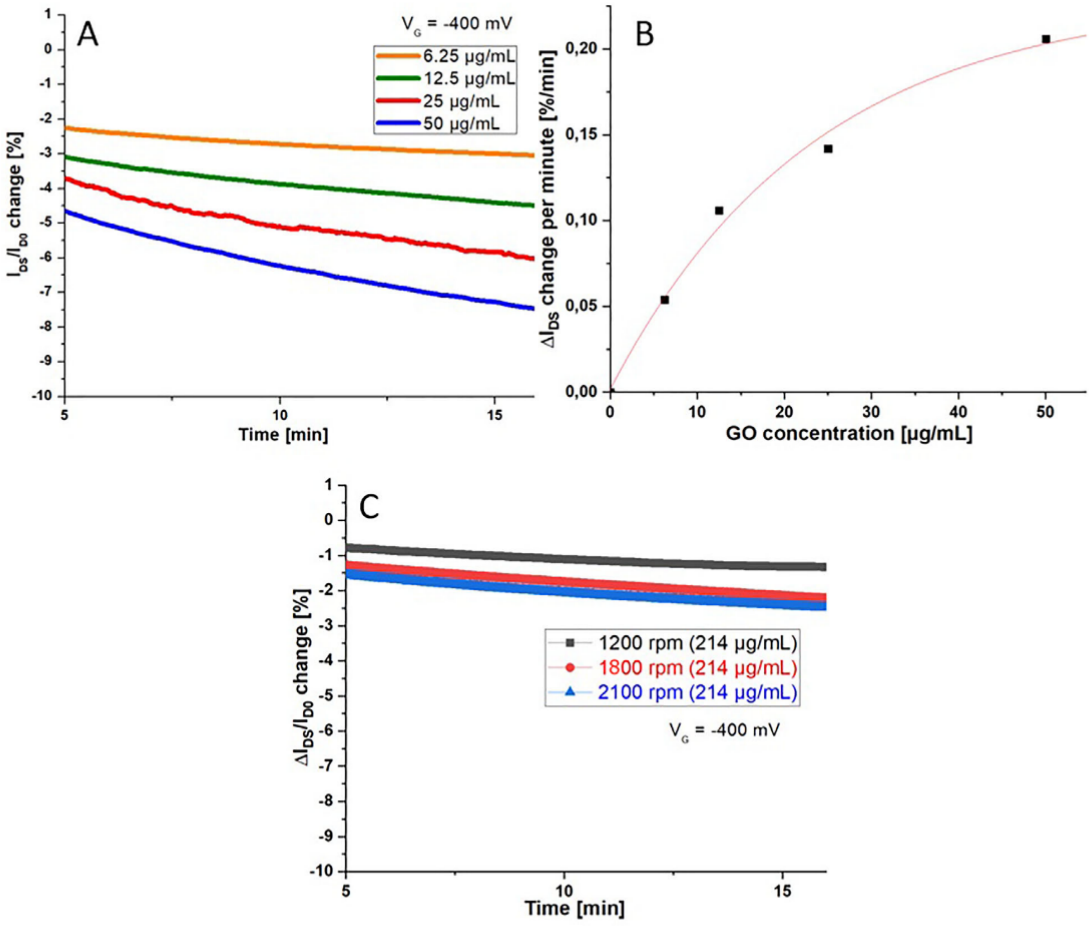

FIGURE 5 A) Baseline drifts shown as the change in normalized I_{DS} as a percentage for FETs fabricated with different GO dilutions from 6.25 to 50 μg/mL with an applied V_{GS} of −0.4 V. B) The baseline drifts per minute obtained from (A) in correlation to the used GO solution concentration. C) Baseline drifts of spin coated rGO FETs shown as the change in normalized I_{DS} as a percentage (214 μg/mL of GO applied with 1200, 1800 and 2100 rpm)

has been shown previously that protonation and especially intercalation effects of the buffer solution in biological applications play a crucial role in the stability of an electrolyte gated FET device and its baseline drift [18–20].

A major prerequisite for the fabrication of surfaces was to reduce the number of graphitic structures, which, as argued above, is possible with the used spin coating method. Regardless, an initial centrifugation step was implemented before GO application to remove any graphitic structures from the solutions. Still, during this study it was observed that excessive centrifugation or ultrasonication (to exfoliate graphitic structures) resulted in smaller flake sizes. We optimized the centrifugation time was to reduce the amount of graphitic structures while maintaining optimal flake size such that a single graphene flake could bridge the gap between electrodes. Graphite is a conducting material and in an interdigitated electrode configuration it presents a major challenge, since one such particle connecting both electrodes will be significantly more conductive than the rGO sheets [21]. Electrically, this can be understood as a parallel circuit of resistors, where a graphitic structure can decrease the resistance of the FETs. Extrapolating from the SEM images of a surface deposited with 1800 rpm and 214 μg/mL, counting the connections from source to drain, approximately 10^5 parallel connections were found for the whole device fabricated with which the electronical characterization was performed for this study. This means that the total resistance of the FET will be lower than the resistance of the most conductive connection and the majority of current flow will be found at that connection. Hence, for most applications it is crucial to fabricate devices where the connection with lowest resistance is the material of interest, in this study being rGO and therefore it is crucial to reduce the number of graphitic structures, as we have done in this study by centrifugation and the choice of suitable spin-coating parameters.

The reproducibility of the fabricated FETs was experimentally verified by the measurements of the $I_D V_G$ response curves to obtain the transconductances of the p-type and n-type charge carriers. In our experience, these response curves are the significant go-to parameter to evaluate the suitability of the devices for a wide range of applications from biosensing, electronic circuits and more. To the best of our knowledge, no other studies have tackled the issue of $I_D V_G$ reproducibility for rGO-based FETs, but it is of utmost importance to make progress towards the fabrication of a commercially available device. Originating from biosensing, our team emphasizes the usability of the resulting EG-FETs for application such as biosensors, focusing on reproducibility, the ability to functionalize the rGO and the devices stability with regard to noise levels and baseline drift. For the evaluation of baseline drift as standard parameters, a 50 mV voltage from source to drain and a gate potential VG of −400 mV were applied and a physiological PBS buffer solution with 150 mM concentration and pH 7.4 was used.

The results of this evaluation are shown in Figure 5(A) for drop casted rGO FETs and in Figure 5(B) for spin coated rGO FETs. Interestingly, the base line stability of devices fabricated by drop casted rGO the depends on the rGO, shown in Figure 5(B). On the other hand, the base line stability of devices fabricated by spin coating does not depend on rotation speed. Furthermore, it appears that when reducing the amount of flake overlaps and multilayers, baseline drift is already in a minimal regime and the observed variations are merely a statistical feature. In detail, the drift for 1200 rpm is 0.04%/min, for 1500 rpm 0.08%/min and for 2100 rpm 0.07%/min. These results are similar to chips prepared *via* drop casting with 6.25 μg/mL (which seems to be around the minimum as seen in Figure 5(B)). However, the devices fabricated by drop casting with such a low GO concentration exhibited very low conductivity and reproducibility, having a wide range of different $I_D V_G$ response curves (Supporting Information). It has been proposed that layer overlaps which lead to intercalation effects could be responsible for the baseline stability of an EG-FET device [22]. By reducing the number of intercalation sites during the herein presented optimization via spin-coating, a reduction of baseline drift and stability was observed, further supporting this argument. As shown in Figure 5, the drifts for drop casted and spin coated rGO were compared under the same conditions and a clear difference was observed, showing significantly higher baseline stability for spin coated rGO FETs.

We therefore argue that by using spin coating with the described parameters we can significantly improve the reproducibility of chip resistance, surface coverage and transfer characteristics. Other methods failed to achieve reproducibility of all these crucial parameters simultaneously.

4 | CONCLUSION

We have described an optimized deposition protocol rGO on silica-based substrates. After investigation of the surface morphology and considerations of the effects of graphitic structures and intercalation, based on the surface coverage and electronic properties a GO solution of 214 μg/mL applied via spin coating with 1800 rpm was found to be most suitable for the fabrication of uniform films. Electrical reproducibility with regards to the transfer characteristics was demonstrated and found to be suitable for the fabrication of different devices, especially biosensors or electronic circuit switches which can also be fabricated on flexible substrates. The devices were tested for their stability regarding baseline drift and found to be significantly superior to drop casted FETs using the same materials. We conclude that spin coating is a significant improvement for the fabrication of well-defined electronic devices using rGO and intend to offer a guideline to members of the community to enable easier handling and fabrication GO- or rGO-based sensing devices.

ACKNOWLEDGMENTS

This project has received funding from the European Union's Horizon 2020 research and innovation programme under the Marie Skłodowska-Curie (grant agreement No 813863), the FFG project under the name OPOSSUM (grant agreement No 870025) and the FFG project under the name TRACK (grant agreement No 873541). The data that support the findings of this study are openly available in Zenodo at https://doi.org/10.5281/zenodo.4041005.

REFERENCES

1. Novoselov, K.S., et al.: Electric field effect in atomically thin carbon films. Science 306(5696), 666–669 (2004)
2. Coroș, M., et al.: A brief overview on synthesis and applications of graphene and graphene-based nanomaterials. Front. Mater. Sci. 13(1), 23–32 (2019)
3. Li, X., et al.: Large-area synthesis of high-quality and uniform graphene films on copper foils. Science 324(5932), 1312–1314 (2009)
4. Chang, H., Wu, H.: Graphene-based nanomaterials: Synthesis, properties, and optical and optoelectronic applications. Adv. Funct. Mater. 23(16), 1984–1997 (2013)
5. Bhaviripudi, S., et al.: Role of kinetic factors in chemical vapor deposition synthesis of uniform large area graphene using copper catalyst. Nano Lett. 10(10), 4128–4133 (2010)
6. Becerril, H., et al.: Evaluation of solution-processed reduced graphene oxide films as transparent conductors. ACS Nano 2, 463–470 (2008)
7. Fatt Teoh, H., et al.: Direct laser-enabled graphene oxide–reduced graphene oxide layered structures with micropatterning. J. Appl. Phys. 112(6), 064309 (2012)
8. Kim, H.P., bin Mohd Yusoff, A.R., Jang, J.: Organic solar cells using a reduced graphene oxide anode buffer layer. Sol. Energy Mater. Sol. Cells 110, 87–93 (2013)
9. Liu, J., et al.: Bulk heterojunction polymer memory devices with reduced graphene oxide as electrodes. ACS Nano 4(7), 3987–3992 (2010)
10. He, Q., et al.: Transparent, flexible, all-reduced graphene oxide thin film transistors. ACS Nano 5(6), 5038–5044 (2011)
11. Liu, J., et al.: Fabrication of flexible, all-reduced graphene oxide non-volatile memory devices. Adv. Mater. 25(2), 233–238 (2013)

12. Liu, X., et al.: Sandwich nanoarchitecture of Si/reduced graphene oxide bilayer nanomembranes for Li-ion batteries with long cycle life. ACS Nano 9(2), 1198–1205 (2015)
13. Aspermair, P., et al.: Dual monitoring of surface reactions in real-time by combined surface-plasmon resonance and field-effect transistor interrogation. J. Am. Chem. Soc. 142(27), 11709–11716 (2020)
14. Reiner-Rozman, C., Kotlowski, C., Knoll, W.: Electronic biosensing with functionalized rGO FETs. Biosensors 6(2), 17 (2016)
15. Cooper, D.R., et al.: Experimental review of graphene. ISRN Condens. Matter Phys. 2012, 1–56 (2012)
16. Garg, R., Dutta, N.K., Choudhury, N.R.: Work function engineering of graphene. Nanomaterials 4(2), 267–300 (2014)
17. Alazmi, A., et al.: Comparative study of synthesis and reduction methods for graphene oxide. Polyhedron 116, 153–161 (2016)
18. Verguts, K., et al.: Graphene delamination using 'electrochemical methods': An ion intercalation effect. Nanoscale 10(12), 5515–5521 (2018)
19. Cicero, G., et al.: Water confined in nanotubes and between graphene sheets: A first principle study. J. Am. Chem. Soc. 130(6), 1871–1878 (2008)
20. Qian, Z., Wei, G.: Electric-field-induced phase transition of confined water nanofilms between two graphene sheets. J. Phys. Chem. A 118(39), 8922–8928 (2014)
21. Marinho, B., et al.: Electrical conductivity of compacts of graphene, multi-wall carbon nanotubes, carbon black, and graphite powder. Powder Technol. 221, 351–358 (2012)
22. Haidry, A.A., et al.: Thermally reduced graphene oxide showing n-to p-type electrical response inversion with water adsorption. Appl. Surf. Sci. 531, 147285 (2020)

SUPPORTING INFORMATION

Additional supporting information may be found online in the Supporting Information section at the end of the article.

How to cite this article: Reiner-Rozman, C., et al.: The top performer: towards optimized parameters for Reduced graphene oxide uniformity by Spin coating. *Micro Nano Lett.* 1–7 (2021) https://doi.org/10.1049/mna2.12070.

Supporting Information: The top performer: Towards optimized parameters for reduced graphene oxide uniformity by spin coating

Ciril Reiner-Rozman[1,2] , Roger Hasler[1] , Jakob Andersson[1], Teresa Rodrigues[1], Anil Bozdogan[3], Johannes Bintinger[1,2], Patrik Aspermair[1]

1 Biosensor Technologies, Austrian Institute of Technology, Konrad-Lorenz Strasse 24, Tulln an der Donau 3420, Austria

2 Danube Private University, Steiner Landstraße 124, 3500 Krems an der Donau

3 CEST Kompetenzzentrum für elektrochemische Oberflächentechnologie GmbH, Viktor Kaplan Straße 2, Wiener Neustadt 2700, Austria

Corresponding Author:

CirilReiner-Rozman, BiosensorTechnologies, Austrian Institute of Technology, Konrad-Lorenz Strasse 24, Tulln an der Donau 3420, Austria.

Email: Ciril.Reiner-Rozman@ait.ac.at

Funding Information: H2020 Marie Skłodowska-CurieActions, Grant/Award Number: 813863; Österreichische Forschungsförderungsgesellschaft, Grant/Award Numbers: 870025, 873541

Evaluation of the surface coverage using ImageJ:

In order to evaluate the surface coverage of rGO coated FET substrates the obtained SEM images were converted into binary images by thresholding using the image processing software ImageJ. By adjusting the threshold value only pixels falling within a specified range are found. After choosing suitable threshold levels to cover only the rGO coated parts in the SEM image the obtained area in the binary image was determined using the software integrated measurement tool.

As an example, we show the evaluation for the surfaces presented in figure 1 of the manuscript, the software output parameters are shown below the unmodified SEM images (top left) and the obtained binary image (top right):

A

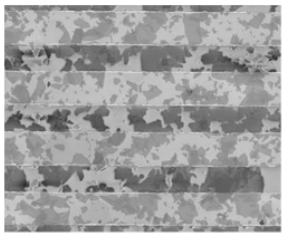

	Area	Mean	Min	Max	%Area	MinThr	MaxThr
1	54263	255	255	255	61.273	255	255

B

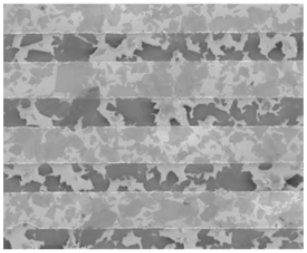

	Area	Mean	Min	Max	%Area	MinThr	MaxThr
1	64643	255	255	255	72.993	255	255

C

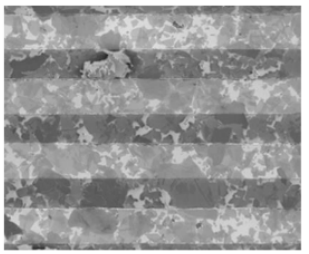

	Area	Mean	Min	Max	%Area	MinThr	MaxThr
1	77391	255	255	255	87.388	255	255

From adjustment of the threshold and referencing to the pristine data, the measurement error for this technique was found, using the upper and lower boundaries of the image contrast covering only the rGO. Threshold values of such boundary conditions can be identified considering the histogram of the image. Therefore, the surface coverage using an upper and lower threshold value was determined and the margin of error was obtained according to

$$\bar{x} \pm z^* \frac{\sigma}{\sqrt{n}}$$

where $\bar{x}$ is the mean surface coverage, σ the standard deviation, n the sample size and z^* the confidence level-specific value for a standard normal distribution. A margin of error of 4,7% was obtained according to a confidence level of 90%. As an example, this is shown below for figure 1A. Additionally, a general minimum error of 2% was assumed due to the electrode edges in the SEM images, according to the ratio of the edge sizes to the total image size, leading to a total error of 6,7%.

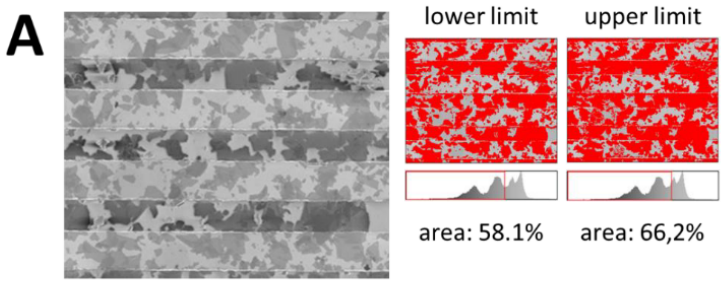

The technique is reliable for discriminating rGO covered areas from the bare SiO_2 substrate according to the different intensity values of individual pixels (as previously reported [1]). The proper selection of single and multilayer rGO is considerably simplified when looking at the histograms instead of the images directly. The rGO covered areas have higher values compared to the SiO2 background and can therefore be easily identified. But a closer look at the histogram shows different intensity peaks for different threshold values according to single or multilayers of rGO which appear lighter or darker in the SEM image. By choosing a threshold value between such peaks it is possible to distinguish those different classes of rGO layers and determine their surface area. This is shown in the image below [1].

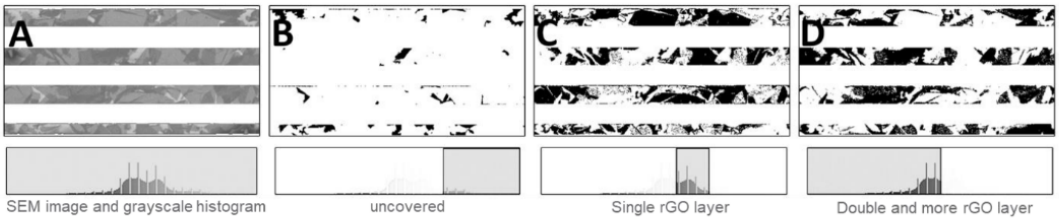

Appearance of multilayers of rGO deposited on interdigitated electrodes

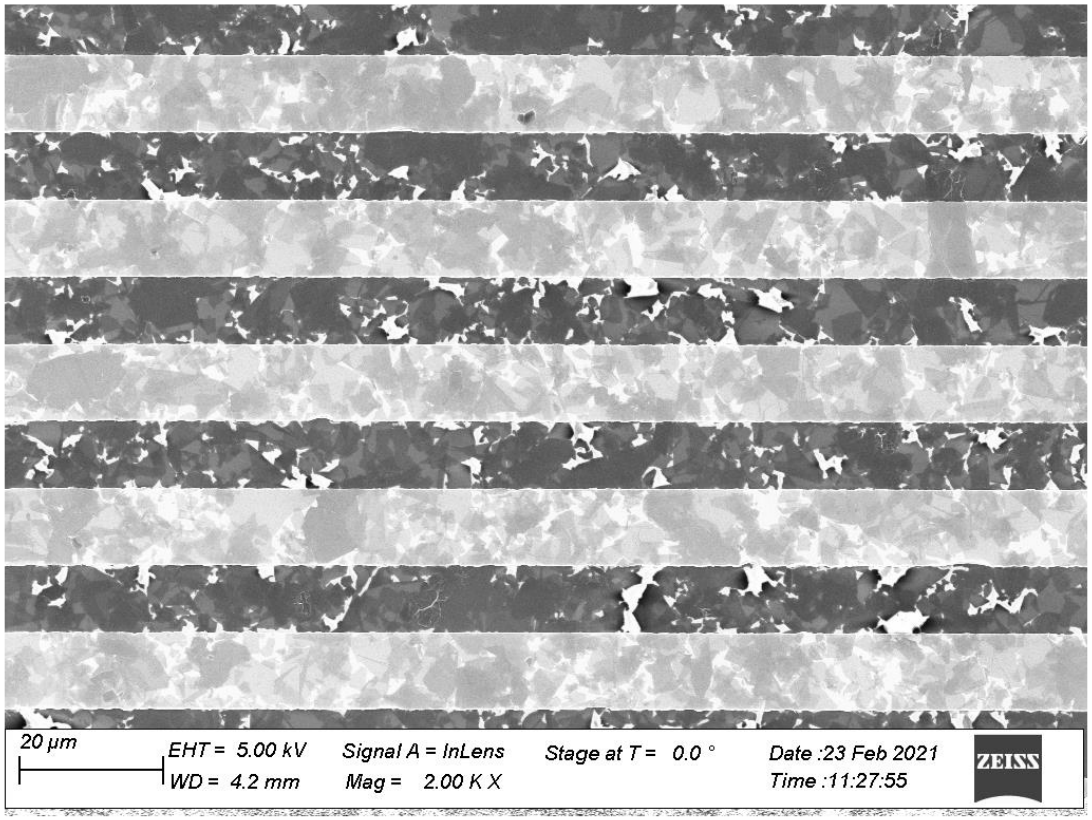

The different shades of grey in the SEM evaluation for the rGO covered surface allows us to estimate the percentage of multilayers. Theoretically optical analysis via the greyscale as described in the chapter above would be possible to evaluate the surface percentage covered with multilayers. However, in the practical approach, this procedure results in high uncertainty, depending on the adjusted grey threshold, since this procedure depends on small colour gradient variations, which is not feasible when precise statements need to be achieved.

Reference:

[1] Aspermair, P.; Doctoral Thesis, *Bio-sensing 2.0 – Electrical and optical measurement tools Towards a research platform for investigating bio-surface interactions*, University of Lille, **2019**.

6.2 Development of a specific troponin I detection system with enhanced immune sensitivity using a single monoclonal antibody

Bozdogan Anıl, El-Kased Reham F., Jungbluth Vanessa, Knoll Wolfgang, Dostalek Jakub and Kasry Amal 2020. Development of a specific troponin I detection system with enhanced immune sensitivity using a single monoclonal antibody. R. Soc. open sci.7200871200871 http://doi.org/10.1098/rsos.200871

First author paper:

A.K. and I collaborated on formulating the experimental design for Surface Plasmon Resonance (SPR), enhancing the assay, and undertaking comprehensive data analysis. We discussed the results, drafted the initial manuscript, developed figures, and reviewed and edited the final paper. V.J. was instrumental in designing and executing the SPR experiments. R.F.E. handled the SDS-PAGE, Western blot analysis, and protein modelling, and also contributed to writing the manuscript. J.D. and W.K. made crucial contributions to both the conception of the experiments and the crafting of the manuscript.

In this chapter, we report rapid detection of troponin I, a crucial biomarker for diagnosing myocardial infarction, using an immunoassay combined with surface plasmon fluorescence spectroscopy. Achieving a limit of detection (LoD) of 19 pM in 45 minutes, this system covers most of the clinically relevant range and allows detection using a single specific monoclonal antibody, beneficial for detecting complex forms in real samples.

ROYAL SOCIETY OPEN SCIENCE

royalsocietypublishing.org/journal/rsos

Research

Cite this article: Bozdogan A, El-Kased RF, Jungbluth V, Knoll W, Dostalek J, Kasry A. 2020 Development of a specific troponin I detection system with enhanced immune sensitivity using a single monoclonal antibody. *R. Soc. Open Sci.* **7**: 200871.
http://dx.doi.org/10.1098/rsos.200871

Received: 22 May 2020
Accepted: 10 September 2020

Subject Category:
Physics and biophysics

Subject Areas:
materials science/biomaterials/biophysics

Keywords:
troponin I, surface plasmon, single monoclonal antibody, biosensor

Authors for correspondence:
Reham F. El-Kased
e-mail: amal.kasry@bue.edu.eg
Jakub Dostalek
e-mail: jakub.Dostalek@ait.ac.at
Amal Kasry
e-mail: reham.kased@bue.edu.eg

Electronic supplementary material is available online at https://doi.org/10.6084/m9.figshare.c.5141460.

THE ROYAL SOCIETY PUBLISHING

Development of a specific troponin I detection system with enhanced immune sensitivity using a single monoclonal antibody

Anıl Bozdogan[1,2], Reham F. El-Kased[3], Vanessa Jungbluth[2], Wolfgang Knoll[1,2], Jakub Dostalek[2] and Amal Kasry[1,4]

[1]CEST Competence Centre for Electrochemical Surface Technology, 2700 Wiener Neustadt, Austria
[2]Biosensor Technologies, AIT-Austrian Institute of Technology GmbH, Konrad-Lorenz-Straße 24, 3430 Tulln, Austria
[3]Department of Microbiology and Immunology, Faculty of Pharmacy, and
[4]Nanotechnology Research Centre (NTRC), The British University in Egypt (BUE), El-Sherouk City, Suez Desert Road, Cairo 11837, Egypt

AK, 0000-0002-8130-8693

Using an immunoassay in combination with surface plasmon fluorescence spectroscopy (SPFS), we report the rapid detection of troponin I, a valuable biomarker for diagnosis of myocardial infarction. We discuss the implementation of (i) direct, (ii) sandwich, and (iii) competitive assay formats, based on surface plasmon resonance and SPFS. To elucidate the results, we relate the experiments to orientation-dependent interaction of troponin I epitopes with respective immunoglobulin G antibodies. A limit of detection (LoD) of 19 pM, with 45 min readout time, was achieved using single monoclonal antibody that is specific for one epitope. The borderline between normal people and patients is 20 pM to 83 pM cTnI concentration, and upon the outbreak of acute myocardial infraction it can raise to 2 nM and levels at 20 nM for 6–8 days, therefore the achieved LoD covers most of the clinically relevant range. In addition, this system allows for the detection of troponin I using a single specific monoclonal antibody, which is highly beneficial in case of detection in real samples, where the protein has a complex form leading to hidden epitopes, thus paving the way towards a system that can improve early-stage screening of heart attacks.

1. Introduction

Cardiovascular diseases (CVD) refer to several types of conditions that affect the heart and blood vessels, which include acute myocardial infarction (AMI), coronary heart disease (CHD), cerebrovascular disease, peripheral arterial disease, rheumatic heart disease and congenital heart disease. According to the World Health Organization (WHO), CVD is the leading cause of death worldwide, where it is responsible for 30% of all deaths globally and WHO estimates that by 2030, 23.6 million people will die from CVD [1]. Low- and middle-income countries often lack the integrated principal healthcare programmes for early diagnosis and treatment of people with risk factors compared with people in high-income countries, causing the annual costs of CVD management worldwide to be extremely high. In Egypt, as an example, WHO published in 2014 that CHD deaths reached 23.14% of total deaths, which ranks Egypt as the twenty-third in CHD worldwide [2]. Therefore, there is a strong demand for a robust and economical approach for early diagnosis and prognosis of CVD.

The use of classical CVD biomarkers, such as creatine kinase (CK) and lactate dehydrogenase, has been restricted owing to absence of tissue specificity and sensitivity. In 2000, the European Society of Cardiology and the American College of Cardiology recommended the use of troponin as a biomarker for the diagnosis of AMI [3], owing to the presence of tissue-specific isoforms in cardiac muscle. Troponin complex (cTn) is a heterogenic protein, which plays an important role in the regulation of cardiac muscle contraction. The troponin complex consists of three subunits: troponin T (cTnT), troponin I (cTnI) and troponin C (cTnC). Being expressed only in cardiac tissue, troponins I and T have been the preferred biomarkers for myocardial infarction for a long time [4]. cTnI is confined inside the heart muscle and it is, therefore, considered to be the standard biomarker for detecting AMI, because it is significantly more specific than other heart markers [5]. Early troponin I detection would lead to faster diagnosis and consequently the initiation of the correct treatment, which improves the prognosis for patients. It has been demonstrated that testing troponins on patient admission and again after 6–12 h provides better risk stratification and early diagnosis [6]. cTnI levels begin to rise 2–3 h after the myocardial infarction and elevation of its levels can persist for up to 10 days, making it ideal for retrospective diagnosis of infarctions [7–9]. The borderline between normal people and patients is 20 pM to 83 pM cTnI concentration, while after the outbreak of AMI, this concentration can go up to 2 nM within 3–6 h, and levels at about 20 nM for 6–8 days [10].

Several epitopes are identified on the cTnI protein; of which only six are used in laboratory research and clinical research (aa 24–40, aa 22–43, aa 41–49, aa 83–93, aa 87–91, and aa 186–192, respectively). Five of these epitopes are located on the N-terminus, which is considered the leading antigenic region of the recombinant version of cTnI protein (TNNI3 sequence) [11–13]. Different diagnostic assays have been designed for the quantitative measurements of cTnI in human blood using monoclonal antibodies, which have found widespread clinical applications as diagnostic and therapeutic agents for different diseases [14]. However, this approach lacks robustness and the common reason for the inconsistency between cTnI assay measurements can be attributed to the difference in the epitope specificity of the antibodies used in various assays. In addition, some epitopes are lost as a result of degradation of circulating troponin I, whereas others remain unaltered, resulting in different recoveries by different assays [15].

Surface plasmon resonance (SPR) biosensors represent an established technique for rapid detection and interaction analysis of biomolecules on solid surfaces [16–19]. In this technique, resonantly excited surface plasmons are used for probing the capture of specific target analytes from the analysed sample at the sensor surface. Surface plasmons originate from collective oscillations of the electron density in the metal coupled to an associated electromagnetic field that is confined to the metallic layer or metallic nanostructures deployed at the sensor surface. The analyte binding-induced refractive index change detunes the resonant excitation of surface plasmons and thus is converted to an optical signal. In addition, the resonant excitation of surface plasmons generates an enhanced electromagnetic field intensity, which can be employed for the amplification of weak spectroscopy signals such as scattering [20] and fluorescence [21]. Up to now, the probing with surface plasmons was exploited in a range of biosensors for rapid and sensitive detection of cardiac biomarkers including those based on SPR supported by metallic nanoparticles [22], gold nanoparticle aggregation assay with colorimetric readout [23], surface plasmon-enhanced scattering [20], and localized surface plasmon-enhanced fluorescence [24].

The detection of the full-length cTnI is usually performed either by polyclonal antibody or multiple monoclonal antibodies specific for several epitopes [9,25,26], in order to increase the sensitivity and the specificity, which is important in case if the protein is in its complex form.

This work reports, for the first time to our knowledge, on using surface plasmon-enhanced fluorescence spectroscopy (SPFS) assay for the sensitive detection of cTnI at clinically relevant

concentrations, using only one monoclonal antibody specific for one cTnI epitope. Moreover, it attempts to elucidate the role of the biointerface design by combined SPR and SPFS study in order to optimize the assay performance characteristics. This study is supported by protein modelling in order to visualize the dependence of the epitopes exposure on the protein orientation, which plays a significant role and it may provide important insights into the future development of cTnI immunoassays for accurate screening of CVD at early stage.

2. Material and methods

2.1. Materials

Recombinant cTnI protein TNNI3 and anti-(TNNI3) goat polyclonal antibody were purchased from MyBioSource, San Diego, CA, USA (cat. no. MBS2010502 and cat. no. MBS 833132, respectively). The cTnI protein was reconstituted in phosphate buffer saline (PBS), pH 7.4, to obtain a final concentration of 100 µg ml^{-1}. High performance chromatography was done to purify and remove any salts from the protein. Monoclonal mouse immunoglobulin G (IgG) against cTnI epitope aa 87–91, Goat anti-mouse IgG conjugated with Alexa Flour 647, and Donkey anti-goat IgG Alexa Flour 647, were all purchased from antibodies-online, USA.

2.2. Gel electrophoresis

1D sodium dodecyl sulfate-polyacrylamide gel electrophoresis (SDS-PAGE) was performed for the full-length recombinant cTnI to determine purity and molecular weight, and 13 5 µl of pure sample was mixed with 5 µl sample buffer [13] (156 mM (hydroxymethyl)aminomethane (TRIS), 5% SDS, 25% glycerol, 0.5% bromophenol blue and 12.5% 2-mercaptoethanol) [13]. The mixture (10 µl) was loaded on a Bolt 4–12% Bis-Tris Plus Gels, 1.0 mm × 15 well (Life Technologies Europe, Bleiswijk, the Netherlands). Gels were run at a constant voltage of 200 V for 50 min in 3-(N-morpholino)propanesulfonic acid (MOPS) buffer (0.025 M MOPS, 0.025 M TRIS, 3.465 mM SDS, 1.025 mM ethylenediaminetetraacetic acid (EDTA)) using the XCell SureLock Mini Cell electrophoresis chamber (Invitrogen, Karlsruhe, Germany). For all experiments, low range marker (MyBioSource, USA) was used [13]. Gels were stained using colloidal Coomassie Brillant Blue R-250 (MP, BIO, ICN, Santa Ana, CA, USA; cat. no. 821616).

2.3. Western blot

After performing the full-length protein to 1D SDS-PAGE as explained above, samples were blotted onto a polyvinylidene difluoride membrane [13] (Ji'an Qingfeng membrane Co., Ltd, Ji'an, China) by semi-dry blotting for 1 h with an electric current of 1.2 mA cm^{-2}, followed by cutting the membrane into strips and blocking with 2 ml buffer (Tris-buffered saline (TBS) 5% non-fat dry milk powder, 1% bovine serum albumin (BSA)) and incubation for 2 h [13]. The goat anti-cTnI polyclonal antibody (suspended in 0.01 M PBS [13], pH 7.4, concentration: 1 mg ml^{-1}) was used after 1 : 1800 dilution with blocking buffer [13]. Each strip was blocked and then incubated with 2 ml polyclonal antibody solution for 24 h at 4° C. This step was followed by three washing steps using 2 ml washing buffer per strip (TBS, 0.05% TWEEN 20 (v/v), 0.1% BSA (w/v)) [13]. The secondary antibody used for western blot was anti-goat IgG + HRP from MyBioSource cat. no. MBS 440120. The anti-goat IgG + horseradish peroxidase (HRP) (secondary antibody) solution was diluted to 1 : 20 000 with blocking buffer, 2 ml of this diluted solution was used to incubate the strip for 1 h at room temperature [13]. This was followed by a last washing step before visualization of the resulting band using CN/DAB substrate kit (Thermo Fisher Scientific Pierce Biotechnology, MA, USA, cat. no. 34000).

2.4. Sensor chip preparations and assay developing

A 50 nm gold layer was deposited on a high refractive index glass coated with 1.5 nm chromium, the gold layer was chemically modified with a mix of thiol with carboxy group and thiol with OH group with a ratio 1 : 9 (Sigma) by incubation overnight. The chips were then mounted on a sample holder while being attached to a flow cell of approximately 4 µl volume. The experiment was performed according to the following protocol: (i) the thiol layer was activated by a mix of 1-ethyl-3-(3-dimethylaminopropyl)carbodiimed/N-hydroxysuccinimide (EDC/NHS) (1 : 1 ratio) in order to

Table 1. List of the SPFS set-up devices.

device	supplier
counter (53131A)	agilent (Santa Clara, USA)
fluorescence band pass filter (670FS10–25)	andover Corporation Optical Filter (Salem, USA)
laser notch filter (XNF-632.8–25.0 M)	CVI Melles Griot (Albuquerque, USA)
lock-in amplifier	EG&G (Gaithersburg, USA)
photomultiplier (H6240–01)	Hamamatsu Photonics (Hamamatsu, Japan)

convert the COOH group to NH_2 group, this was done in situ using a pump at a flow rate (40 µl min^{-1}); (ii) cTnI protein was coupled to the sensor surface by the use of amine coupling; (iii) a solution with monoclonal mouse or polyclonal goat antibody (concentration of 1, 5 and 20 nM) was rinsed over this surface; followed by (iv) reaction of the affinity captured antibody with a secondary anti-mouse or anti-goat antibody, respectively. The secondary antibody was conjugated with Alexa Fluor 647 and dissolved in buffer at a concentration of 6 nM.

2.5. Surface plasmon resonance and surface plasmon-enhanced fluorescence spectroscopy measurements

An optical system combining SPR and SPFS was used for direct investigation of the interaction between the protein and its antibodies. The Kretschmann configuration, which is based on a high refractive index prism, 50 nm thermally evaporated gold glass slide, optically matched to the prism through matching oil, was used for the detection. A laser beam at wavelength of 633 nm was coupled to the prism and allowed to resonantly excite surface plasmons at the outer interface of thin gold film with a strength that was controlled by the angle of incidence. A flow cell with a volume of 4 µl was clamped against the gold sensor surface in order to flow liquid samples with a flow rate of 40 µl min^{-1}. The reflected beam intensity was measured with a lock-in amplifier in order to track changes in the SPR signal. The fluorescence signal measured on the SPFS modality was excited via the enhanced electromagnetic field intensity generated by surface plasmons. The emitted fluorescence light (at 670 nm) from the sensor surface was collected through the flow cell by a lens with a numerical aperture about NA = 0.2 and detected by a photomultiplier (H6240-01, Hamamatsu, Japan) that was connected to a counter. The intensity of the excitation beam irradiating the sensing area on the sensor chip of about 1 mm^2 was reduced to 30–60 µW to decrease bleaching of Alexa Fluor 647. The fluorescence light emitted at a wavelength of about 670 nm was spectrally separated from the excitation light at 633 nm by using a set of laser notch filter and fluorescence band pass filter (table 1).

2.6. Protein structure modelling

Protein structure modelling aims to determine spatial location of every atom in the protein molecule from the amino acid sequence by computational calculations. This was done using the I-TASSER server [27–29]. The server uses I-TASSER based algorithms to automatically generate high-quality model predictions for three-dimensional protein structure from their amino acid sequences. The I-TASSER detects structure templates from the Protein Data Bank using a fold recognition technique, which is based on protein modelling using known protein structures. The full-length structure models are constructed by reassembling structural fragments from the protein folding templates using replica exchange Monte Carlo simulations [30].

3. Results and discussion

Figure 1*a*,*b* shows SDS-PAGE of purchased recombinant full-length troponin cTnI to ensure its purity and molecular weight, confirming a molecular weight of 24 kDa. Figure 1*c* shows the Western blot results that confirm the affinity of the antibody to the full-length protein (more details are in the Material and methods section).

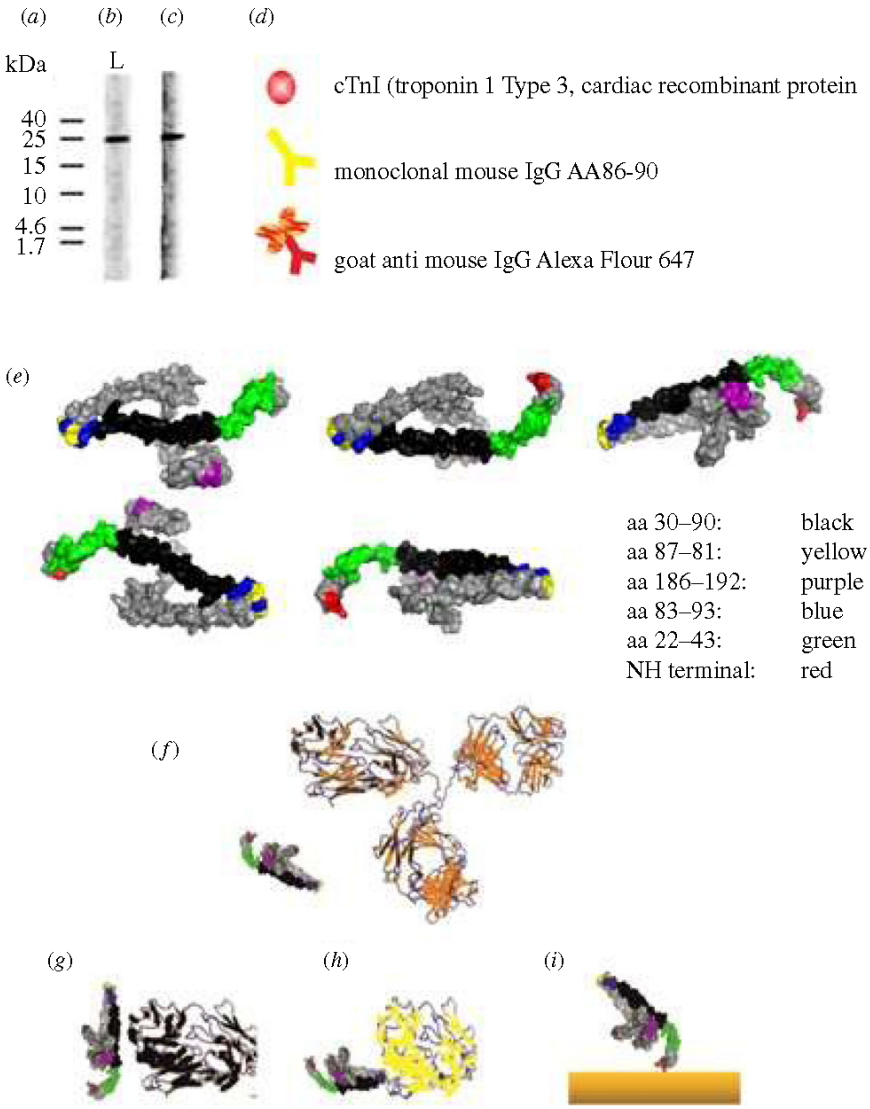

Figure 1. (*a*) cTnI protein marker lane (kDa), (*b*) 1D SDS–PAGE showing a single band at apparent molecular weight 24 kDa compared to the marker lane. (*c*) Western blot analysis against polyclonal anti-troponin antibody on a polyvinylidene fluoride (PVDF) membrane. (*d*) A schematic of the cTnI protein and the antibodies used in the experiments with their colours referring to their respective binding epitopes as shown in figure (*e*). (*e*) Modelled structure of full-length recombinant version of cTnI protein (aa 1–210) using I-TASSER software with its epitopes at different orientations. (*f*) The size comparison of immunoglobulin G antibody and cTnI (≈1 : 3). (*g–i*) shows the visualization of the possible cTnI protein orientation according to the binding epitope position; (*g*) possible orientation of cTnI protein that is affinity bound through its epitope aa 87–91 and (*h*) aa 30–90 to IgG Fab fragment. (*i*) The immobilization of the cTnI protein to the surface through its N-terminal (red) and the possible protein orientation.

Figure 1*d* provides an overview of the biomolecules that are further employed in the cTnI assay with plasmonic biosensor readout including the recombinant version cTnI protein and the respective antibodies (in colour respective to their binding protein epitopes). The structure of the full-length recombinant cTnI protein was visualized using bioinformatics methods for predicting the three-dimensional structure of protein molecules based on their amino acid sequences (more details are in the Methods section). Figure 1*e* shows the cTnI protein at different orientations where its epitopes are visualized with different colours, while the size difference between the protein and its antibody is compared in figure 1*f*. The same bioinformatics method was used to visualize the cTnI protein orientations in case of its affinity binding to mouse monoclonal antibody (recognizing cTnI epitope aa

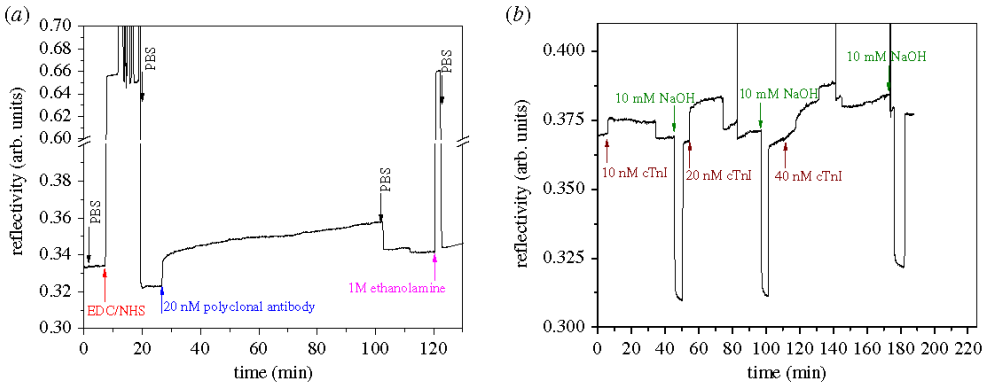

Figure 2. SPR observation of (*a*) immobilization of the polyclonal antibody on the surface modified with SAM, and (*b*) the subsequent affinity binding of the cTnI to the tethered polyclonal antibody with regeneration steps (10 mM NaOH applied) in between flow of cTnI samples.

87–91) and goat polyclonal antibody (recognizing cTnI epitope 30–90), or when coupled to the surface by using the N-terminus (figure 1*g*,*h*,*i*, respectively).

In order to bind both monoclonal and polyclonal antibodies to the cTnI protein, the possible protein orientations reveal that the epitope positions (aa 87–91 coloured in yellow) and (aa 30–90 coloured in black) spatially overlap, which may prohibit forming a sandwich.

Based on the Western blot results and the modelling, the cTnI detection was further investigated by using SPR and SPFS. On a first glance, we used the direct label-free SPR method for measuring the affinity binding of the cTnI to its polyclonal antibody immobilized on the sensor surface. To that end, we started with preparing a self-assembled monolayer (SAM), on the sensor gold surface, composed of thiols synthesized with oligo (ethylene glycol) (OEG) and carboxyl groups. Afterwards, the carboxyl groups were activated with a mix of EDC/NHS [31], followed by the amine coupling of the polyclonal antibody via its N-terminus or lysine groups figure 2*a*. As seen in figure 2*b*, the binding of cTnI showed measurable SPR signal only at a relatively high concentration of 20 nM. cTnI is known to have an isoelectric point in the range below 7 in case of AMI [32], which means that it would be negatively charged at the neutral pH that was used in the experiments. Because the gold surface is modified with a mix of thiol SAM carrying with carboxyl group and OEG groups, at pH 7, the surface would be negatively charged leading to repellence of the negatively charged protein, which in turn should prevent nonspecific binding. Although this charge effect is not strong enough to repel all negatively charged proteins, it is enough to avoid nonspecific binding. As the binding of the cTnI was not recognized until very high concentration, this was not further investigated, and a surface plasmon fluorescence-based protocol was developed.

In order to further confirm that the used monoclonal and polyclonal antibodies recognize the cTnI protein and to improve the sensitivity, SPFS readout modality was employed with the use of a secondary antibody conjugated to Alexa Fluor 647 label. As seen in figure 3*a*, the affinity binding of the antibody at the sensor surface does not change the fluorescence signal kinetics; however, the affinity binding of the respective secondary antibody leads to a strong change in the fluorescence signal $F(t)$. First, a rapid jump in fluorescence signal occurs owing to the excitation of Alexa Fluor 647-labelled molecules in the bulk, followed by gradual slower increase that is ascribed to the affinity binding of secondary antibody at the sensor surface. Upon the subsequent rinsing step, rapid decrease in the fluorescence signal is observed owing to replacing the solution with fluorophore-labelled molecules from the flow cell and then a slow decay in the signal is attributed to the dissociation of the attached biomolecules and bleaching of the fluorophore labels at the sensor surface. The fluorescence sensor response ΔF that is associated with the affinity binding (defined as the difference between the baseline signal before the injection of the antibody and the secondary antibodies and after the final rinsing) is linearly increasing with the concentration of the antibody. The unspecific interaction of the secondary antibody with the sensor surface (without captured anti-cTnI antibody) was tested and a negligible signal of $\Delta F = 132$ cps was measured for the anti-mouse secondary antibody (specific for the monoclonal antibody), however, a strong response of $\Delta F = 2790$ cps was observed for the anti-goat secondary antibody (specific for the polyclonal antibody), as shown in figure 3*b*. As was expected, the SPFS readout using a sandwich assay was not sensitive enough for low concentrations, owing to the close proximity of the epitopes aa 87–91 and aa 30–90

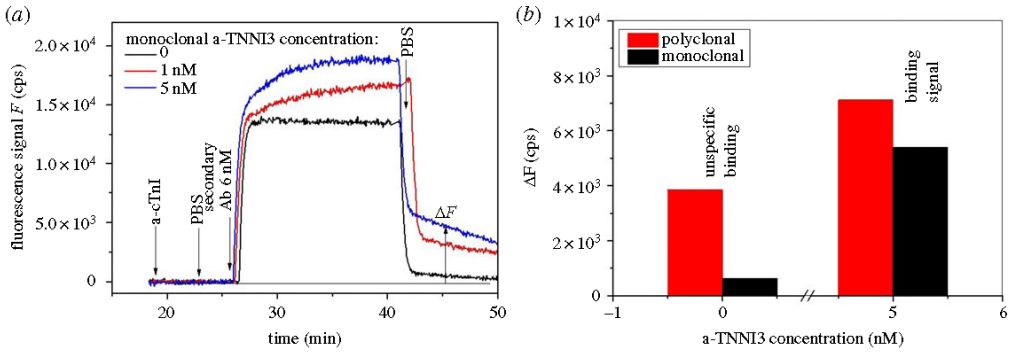

Figure 3. (*a*) Recognition of the monoclonal antibody to the cTnI protein, the black curve represents the control test, where 6 nM Alexa fluor 647 conjugated secondary antibody specific to the monoclonal cTnI was flown, no signal was observed after washing the surface. This was followed by binding of the secondary antibody to different concentrations of the monoclonal antibody bound to the cTnI, which gives clear fluorescence signal (red, blue) indicating successful binding. (*b*) A nonspecific binding test performed by flowing 6 nM Alexa fluor 647 conjugated two secondary antibodies, specific for both the monoclonal and the polyclonal antibodies, clearly showing that the unspecific interaction in case of the polyclonal antibody is higher than that of the monoclonal one (ΔF refers to fluorescence counts).

(figure 1), therefore an inhibition-competitive assay format was developed for the detection of cTnI analyte using the monoclonal anti-cTnI antibody. Although polyclonal antibodies, containing accurately identified antigenic determinants can provide an alternative to monoclonal antibodies for the detection of diseases biomarkers, whenever multipoint binding of the antigen is offered, which can result in an increased sensitivity of the assay owing to the increase in the avidity of antibody-antigen interaction [13], monoclonal antibodies are more advantageous than polyclonal ones. Their specificity is the most important advantage, as they only react with one epitope on the target molecule, while polyclonals contain hundreds or even thousands of specificities that can lead to cross-reactions and consequently much less selectivity. In addition to that, our SPFS results clearly indicate that the nonspecific binding in case of the polyclonal antibody is much higher (figure 3*b*), therefore we chose to develop the competitive assay using the monoclonal antibody. Given that cTnI is released into the blood circulation of patients of AMI predominantly in its complex form, it is crucial to use antibodies which can recognize, not only free cTnI, but also cTnI complexed with other cTn subunits [33], monoloclonals would be more advantageous in that regard. It is worth mentioning that the chosen monoclonal mouse IgG against cTnI epitope aa 87–91 is specific for cTnI where the epitope (87–91; GLGFA) is not found through the whole troponin T sequence, therefore, it cannot cross-react with cTnT and it can distinguish between both of them [34], electronic supplementary material.

As schematically shown in figure 4*a*, the developed cTnI assay with SPFS readout consisted of three steps. First, a sensor chip was prepared with cTnI protein immobilized to a mixed thiol SAM by amine coupling. Second, the analysed sample with cTnI was spiked with mouse monoclonal antibody at a concentration of 2 nM and reacted for 20 min. Afterwards, the sample was flowed over the sensor surface for 20 min followed by rinsing for 5 min. Third, a secondary anti-mouse antibody solution (6 nM) was reacted for 20 min with the affinity bound antibody at the sensor surface. After rinsing for 5 min, the fluorescence sensor response ΔF was determined. The established calibration curve in figure 4*b* shows that the sensor response ΔF is inversely proportional to the target cTnI analyte concentration. In a sample with low amounts of cTnI analyte, the majority of binding sites of the antibody spiked into the sample are free and can react with cTnI coupled to the sensor surface. Therefore, a large fluorescence signal is generated after the reaction with the secondary antibody. For large amounts of cTnI target analyte molecules present in the sample, the binding sites of the antibody are occupied, and do not bind to the surface, thus leading to a low fluorescence signal response. In order to calculate the limit of detection (LoD), the response of the fluorescence signals was plotted as a function of the cTnI analyte concentrations (figure 4*c*), and the curve was fitted using the sigmoidal function [35,36]:

$$f(x) = \frac{(A_1 - A_2)}{1 + (c/c_0)^p} + A_2.$$

The achieved LoD is 19 pM, it was determined as the concentration for which the fitted calibration curve intersects the fluorescence signal measured for a blank sample (ΔF0 = 132 cps) lowered by three times the standard deviation of noise (σ = 10.6 cps). Although this achieved LoD is not the lowest

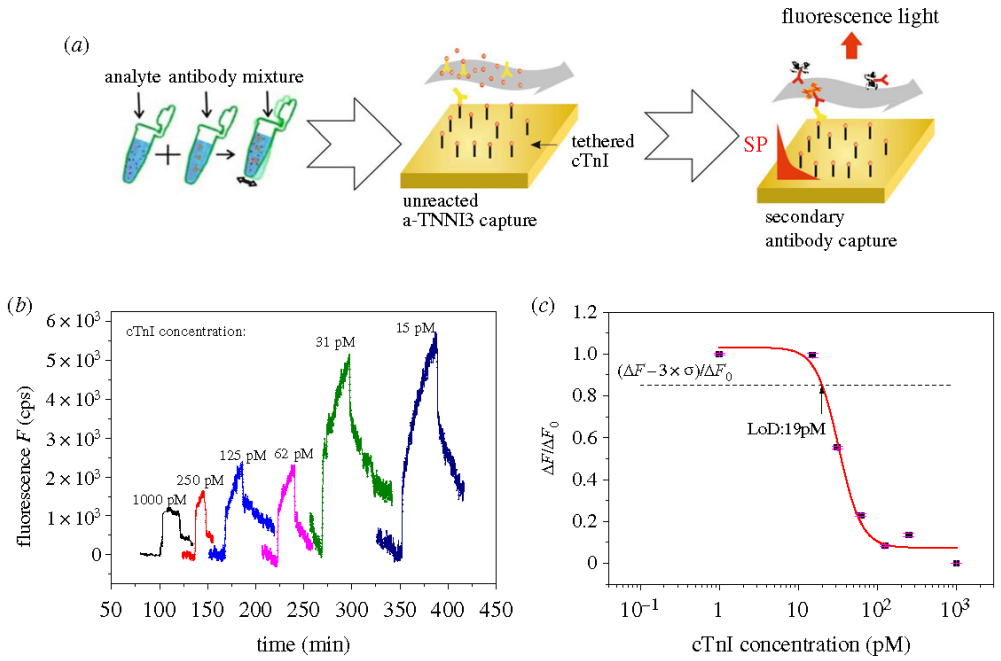

Figure 4. (*a*) A schematic of the inhibition-competitive assay steps, (*b*) fluorescence signal kinetics measured upon the binding of the secondary antibody conjugated with Alexa Fluor 647 and varied concentrations of cTnI, and (*c*) normalized calibration curve of the SPFS biosensor with an indicated LoD of 19 pM.

among the previously investigated detection methods of cTnI, it is to the authors' knowledge, the first time to detect this protein using a single monoclonal antibody specific for one epitope, which would be very beneficial to use in case of using real samples where the protein is known to be in its complex form. Detailed summaries of the other detection methods and LoDs are in [10,37].

It is worth noting that the proposed SPFS readout is inherently more tolerant to fouling of the sensor surface that inevitably occurs on the gold sensor surface with thiol SAM carrying oligo(ethylene glycol) chains when realistic samples such as blood serum [38] are tested. For the analysis of biomarkers in more complex samples including saliva and blood plasma, more advanced biointerfaces based on anti-fouling polymer brushes [39,40] can be deployed on the surface of plasmonic biosensors as was previously reported by our laboratory. In combination with the advancement of SPFS instrumentation and biointerfaces (which were not the subject of the present research reported here), the reported results make an important step towards developing affinity biosensors that can serve for rapid diagnosis of cardiac diseases at an early stage with reliable and reproducible results.

4. Conclusion

We have developed a sensitive troponin cTnI immunoassay, using a single monoclonal antibody, with an LoD of 19 pM in 45 min detection time. It takes advantage of SPFS detection by optically probing the enhanced field intensity at the fluorophore label absorption wavelength (λ_{abs}: 633 nm). We illustrate that the direct detection format based on the regular SPR biosensor principle does not provide sufficient sensitivity for the analysis of cTnI at clinically relevant concentrations. By using the same instrument operated in SPFS modality, we significantly improved the sensitivity by implementing an inhibition-competitive immunoassay. Crucial for this assay format is the careful selection of cTnI epitope and respective monoclonal antibody based on both experimental trials and theoretical modelling. These studies confirmed that immobilizing the ligand (recombinant version of target cTnI protein) directly to the surface via its N-terminal leaves the epitopes aa 30–90 and aa 87–91 available for affinity binding of respective IgG antibodies.

Data accessibility. All the necessary data are included in the main manuscript and figures, and raw data for all the figures in the paper are uploaded as electronic supplementary material. BLAST results are presented in the electronic supplementary material file.

Authors' contributions. R.F.E. performed the SDS–PAGE, Western blot analysis and the protein modelling, A.B., V.J. and A.K. designed and performed the SPR experiments. A.K., A.B. and R.F.E. wrote the paper, J.D. and W.K. contributed to both the design of the experiments and writing the paper. All authors contributed to different aspects of the work, including writing and reviewing the paper.

Competing interests. We declare we have no competing interests.

Funding. The authors would like to thank the Competence Centre for Electrochemical Surface Technology (CEST) and the British University in Egypt (BUE) for financial support.

Acknowledgements. J.D. acknowledges support from the European Union's Horizon 2020 research and innovation program under the Marie Sklodowska-Curie grant agreement no. 64268.

References

1. WHO. 2020 Cardiovascular diseases. See https://www.who.int/cardiovascular_diseases/about_cvd/en/.
2. WHO. 2018 Cardiovascular diseases. See http://www.who.int/mediacentre/factsheets/fs317/en/ (accessed 4 September 2018).
3. Babuin L, Jaffe SA. 2005 Troponin: the biomarker of choice for the detection of cardiac injury. *CMAJ* **173**, 1191–1202. (doi:10.1503/cmaj/051291)
4. Thygesen K, Alpert JS, White HD. 2007 Universal definition of myocardial infarction. *Eur. Heart J.* **28**, 2525–2538. (doi:10.1093/eurheartj/ehm355)
5. Nusier MK, Ababneh BM. 2006 Diagnostic efficiency of creatinine kinase (CK), CKMB, troponin T and troponin I in patients with suspected acute myocardial infarction. *J. Health Sci.* **52**, 180–185. (doi:10.1248/jhs.52.180)
6. Forberg JL, Henriksen LS, Edenbrandt L, Ekelund U. 2006 Direct hospital costs of chest pain patients attending the emergency department: a retrospective study. *BMC Emerg. Med.* **6**, 6. (doi:10.1186/1471-227X-6-6)
7. Wendy L, Cook DJ, Griffith LE, Crowther MA, Devereaux PJ. 2006 Elevated cardiac troponin levels in critically ill patients: prevalence incidence and outcomes. *Am. J. Crit. Care* **15**, 280–288. (doi:10.4037/ajcc2006.15.3.280)
8. Heidenreich PA, Alloggiamento T, Mcdonald KM, Go AS, Hlatky MA, Melsop K. 2001 The prognostic value of troponin in patients with non-ST elevation acute coronary syndromes: a meta-analysis. *J. Am. Coll. Cardiol.* **38**, 478–485. (doi:10.1016/S0735-1097(01)01388-2)
9. Qureshi A, Gurbuz Y, Niazi JH. 2012 Biosensors for cardiac biomarkers detection: a review. *Sens. Actuators B* **171**, 62–76. (doi:10.1016/j.snb.2012.05.077)
10. Han H, Li S, Peng P, Othman AM, Leblanc R. 2016 Recent development of cardiac troponin I detection. *ACS Sens.* **1**, 106–114. (doi:10.1021/acssensors.5b00318)
11. Katrukha AG. 2003 Antibody selection strategies in cardiac troponin assays. In *Cardiac markers* (ed. AHB Wu), pp. 173–185, 2nd edn. Berlin, Germany: Springer.
12. Vylegzhanina AV, Katrukha IA, Kogan AE, Bereznikova AV. 2013 Epitope specificity of anti-cardiac troponin I monoclonal antibody 8I-7. *Clin. Chem.* **59**, 1814–1816. (doi:10.1373/clinchem.2013.209528)
13. El-kased RF. 2018 Immuno-analytical approach and its application for cardiac disease marker detection. *J. Immunoassay Immunochem.* **39**, 538–550. (doi:10.1080/15321819.2018.1518241)
14. Sanjay ST, Fu G, Dou M, Xu F, Liu R, Qi H, Li X. 2015 Biomarker detection for disease diagnosis using cost-effective microfluidic platforms. *Analyst* **140**, 7062–7081. (doi:10.1039/c5an00780a)
15. Apple FS, Smith SW, Pearce LA, Murakami MM. 2019 Assessment of the multiple-biomarker approach for diagnosis of myocardial infarction in patients presenting with symptoms suggestive of acute coronary syndrome. *Clin. Chem.* **55**, 93–100. (doi:10.1373/clinchem.2008.102905)
16. Knoll W. 1998 Interfaces and thin films as seen by bound electromagnetic waves. *Ann. Rev. Phys. Chem.* **49**, 569–638. (DOI:10.1146/annurev.physchem.49.1.569)
17. Liebermann T, Knoll W. 2000 Surface-plasmon field-enhanced fluorescence spectroscopy. *Colloids Surf.* **171**, 115–130. (doi:10.1016/S0927-7757(99)00550-6)
18. Knoll W, Kasry A, Yu F, Wang Y, Brunsen A, DostALek J. 2008 New concepts with surface plasmons and nano-biointerfaces. *JNOPM* **17**, 121–129. (doi:10.1142/S0218863508004081)
19. Dostálek J, Kasry A, Knoll W. 2007 Long range surface plasmons for observation of biomolecular binding events at metallic surfaces. *Plasmonics* **2**, 97–106. (doi:10.1007/s11468-007-9037-8)
20. Yang CT, Wu L, Liu X, Tran NT, Bai P, Liedberg B, Wang Y, Thierry B. 2016 Exploiting surface-plasmon-enhanced light scattering for the design of ultrasensitive biosensing modality. *Anal. Chem.* **88**, 11 924–11 930. (doi:10.1021/acs.analchem.6b03798)
21. Martin B, Koji T, Mana T, Qingwen Z, Jakub D. 2014 Plasmon-enhanced fluorescence biosensors: a review. *Plasmonics* **9**, 781. (doi:10.1007/s11468-013-9660-5)
22. Tadepalli S *et al.* 2015 Peptide functionalized gold nanorods for the sensitive detection of a cardiac biomarker using plasmonic paper devices. *Sci. Rep.* **5**, 16206. (doi:10.1038/srep16206)
23. Liu X, Wang Y, Chen P, Mccadden A, Palaniappan A, Zhang J, Liedberg B. 2016 Peptide functionalized gold nanoparticles with optimized particle size and concentration for colorimetric assay development: detection of cardiac troponin I. *ACS Sensors* **1**, 1416–1422. (doi:10.1021/acssensors.6b00493)
24. Aslan K, Grell TAJ. 2011 Rapid and sensitive detection of troponin I in human whole blood samples by using silver nanoparticle films and microwave heating. *Clin. Chem.* **57**, 746–752. (doi:10.1373/clinchem.2010.159889)
25. Guy MJ, Chen YC, Clinton L, Zhang H, Zhang J, Dong X, Xu Q, Ayaz-Guner S, Ge Y. 2013 The impact of antibody selection on the detection of cardiac troponin I. *Clin. Chim. Acta* **420**, 82–88. (doi:10.1016/j.cca.2012.10.034)
26. Cai Y, Kang K, Li Q, Wang Y, He X. 2018 Rapid and sensitive detection of cardiac troponin I for point-of-care tests based on red fluorescent microspheres. *Molecules* **23**, 1102. (doi:10.3390/molecules23051102)
27. Zhang Y. 2008 I-TASSER server for protein 3D structure pre-diction. *BMC Bioinf.* **9**, 40. (doi:10.1186/1471-2105-9-40)
28. Roy A, Kucukural A, Zhang Y. 2010 I-TASSER: a unified platform for automated protein structure and function prediction. *Nat. Protocols* **5**, 725–738. (doi:10.1038/nprot.2010.5)
29. Yang J, Yan R, Roy A, Xu D, Poisson J, Zhang Y. 2015 The I-TASSER suite: protein structure and function prediction. *Nat. Methods* **12**, 7–8. (doi:10.1038/nmeth.3213)
30. Thachuk C, Shmygelska A, Hoos HH. 2007 A replica exchange Monte Carlo algorithm for protein folding in the HP model. *BMC Bioinf.* **8**, 342. (doi:10.1186/1471-2105-8-342)
31. Fischer MJE. 2010 Amine coupling through EDC/NHS: a practical approach in surface plasmon resonance; methods and protocols. *Methods Mol. Biol.* **627**, 55–73. (doi:10.1007/978-1-60761-670-2_3)
32. Peronnet E, Becquart L, Martinez J, Charrier JP, Jolivet-Reynaud C. 2007 Isoelectric point determination of cardiac troponin I forms present in plasma from patients with myocardial infarction. *Clin. Chim. Acta* **377**, 243–247. (doi:10.1016/j.cca.2006.10.006)
33. Katrukha AG, Bereznikova AV, Esakova TV, Pettersson K, Lövgren T, Severina ME, Pulkki K, Vuopio-Pulkki L-M, Gusev NB. 1997 Troponin I is released in bloodstream of patients with acute myocardial infarction not in free form but as complex. *Clin. Chem.* **43**, 1379–1385. (doi:10.1093/clinchem/43.8.1379)
34. BLAST. Global alignment. See https://blast.ncbi.nlm.nih.gov/BlastAlign.cgi.

35. Wang Y, Dostalek J, Knoll W. 2009 Long range surface plasmon-enhanced fluorescence spectroscopy for the detection of aflatoxin M1 in milk. *Biosens. Bioelectron.* **24**, 2264–2267. (doi:10.1016/j.bios.2008.10.029)
36. Dostalek J, Pribyl J, Skladal P, Homola J. 2007 Multichannel SPR biosensor for detection of endocrine disrupting compounds. *Anal. Bioanal. Chem.* **389**, 1841–1847. (doi:10.1007/s00216-007-1536-0)
37. Upasham S, Tanak A, Prasad S. 2018 Cardiac troponin biosensors: where are we now? *Adv. Health Care Tech.* **4**, 1–13. (doi:10.2147/AHCT.S138543)
38. Hageneder S, Bauch M, Dostalek J. 2016 Plasmonically amplified bioassay: total internal reflection fluorescence vs. epifluorescence geometry. *Talanta* **156–157**, 225–231. (doi:10.1016/j.talanta.2016.05.023)
39. Riedel T, Hageneder S, Surman F, Pop-Georgievski O, Noehammer C, Hofner M, Brynda E, Rodriguez-Emmenegger C, Dostalek J. 2017 Plasmonic hepatitis B biosensor for the analysis of clinical saliva. *Anal. Chem.* **89**, 2972–2977. (doi:10.1021/acs.analchem.6b04432)
40. Kotlarek D, Vorobii M, Ogieglo W, Knoll W, Rodriguez-Emmenegger C, Dostalek J. 2019 Compact grating-coupled biosensor for the analysis of thrombin. *ACS Sensors* **4**, 2109–2116. (doi:10.1021/acssensors.9b00827)

ROYAL SOCIETY OPEN SCIENCE

Supporting Information

R. Soc. open sci.
doi:10.1098/not yet assigned

Development of a Specific Troponin I Detection System with Enhanced Immune Sensitivity using a Single Monoclonal Antibody

Anıl Bozdogan [1,2], Reham F. El-Kased [3*], Vanessa Jungbluth [2], Wolfgang Knoll [1,2], Jakub Dostalek [2*], Amal Kasry [1,4*]

1 CEST Competence Centre for Electrochemical Surface Technology, 2700 Wiener Neustadt, Austria.
2 Biosensor Technologies, AIT-Austrian Institute of Technology GmbH, Konrad-Lorenz-Straße 24, 3430 Tulln, Austria.
3 Department of Microbiology and Immunology, Faculty of Pharmacy, The British University in Egypt (BUE), El-Sherouk City, Suez Desert Road, Cairo 11837, Egypt.
4 Nanotechnology Research Centre (NTRC), The British University in Egypt (BUE), El-Sherouk City, Suez Desert Road, Cairo 11837, Egypt

Supplementary Information

Raw data of Figures 2, 3, and 4: are submitted as electronic supplementary materials.

Blast results of cTnT and cTnI:

The epitope (87 – 91); GLGFA is not found through the whole Troponin T sequence.

cTnT:

```
  1 msdieevvee yeeeeqeeaa veeqeeaaee daeaeaetee traeedeeee eakeaedgpm
 61 eeskpkprsf mpnlvppkip dgervdfddi hrkrmekdln elqalieahf enrkkeeeel
121 vslkdrierr raeraeqqri rnerekerqn rlaeerarre eeenrrkaed earkkkalsn
181 mmhfggyiqk aqterksgkr qterekkkki laerrkvlai dhlnedqlre kakelwqsiy
241 nleaekfdlq ekfkqqkyei nvlrnrindn qkvsktrgka kvtgrwk
```

cTnI:

```
  1 madgssdaar eprpapapir rrssnyraya tephakkksk isasrklqlk tlllqiakqe
 61 lereaeerrg ekgralstrc qplelaglgf aelqdlcrql harvdkvdee rydieakvtk
121 niteiadltq kifdlrgkfk rptlrrvris adammqallg arakesldlr ahlkqvkked
181 tekenrevgd wrknidalsg megrkkkfes
```

6.3 On the Detection of cTnI - A Comparison of Surface-Plasmon Optical -, Electrochemical -, and Electronic Sensing Concepts

Rodrigues T, Mishyn V, **Bozdogan A**, Leroux, Y.R., Happy H, Kasry A, Boukherroub R, Dostalek J, Aspermair P, Bintinger J, Kleber C, Szunerits S and Knoll W. “On the Detection of cTnI - A Comparison of Surface-Plasmon Optical -, Electrochemical -, and Electronic Sensing Concepts”. Ann Clin Med Case Rep. 2021; V6(2): 1-16

Co-author paper:

I played a pivotal role in engaging in meaningful discussions, crafting the manuscript, and performing in-depth data analysis. I spearheaded the Surface Plasmon Field-Enhanced Fluorescence Spectroscopy (SPFS) experiments and was deeply involved in the design and execution of the gFET experiments. Collaboratively, T.R. and V.M. also played essential roles in designing the gFET experiments, scripting the manuscript, and analyzing the data. L.Y.R. took up the responsibility of synthesizing the diazonium-TIP. R.B., A.K., P.A., J.B., and C.K. contributed significantly to the conceptualization of the project and drafting of the manuscript. S.S. and W.K. participated actively in both designing the experiment and writing the manuscript.

The study focuses on using cTnI as a reference system for biosensor calibration, emphasizing the importance of ease of operation, test kit robustness, and cost over a wide range of LoD values. With ongoing advancements, new proposals targeting these factors will likely emerge for improved detection concepts.

Annals of Clinical and Medical Case Reports

Research Article ISSN 2639-8109 | Volume 6

"On the Detection of cTnI - A Comparison of Surface-Plasmon Optical -, Electrochemical -, and Electronic Sensing Concepts"

Rodrigues T[1,2], Mishyn V[1,2], Bozdogan A[1,3], Leroux, Y.R.[4], Happy H[2], Kasry A[3,5], Boukherroub R[2], Dostalek J[1], Aspermair P[1], Bintinger J[1,6], Kleber C[6], Szunerits S[2] and Knoll W[1,3,6]

[1]AIT Austrian Institute of Technology GmbH, Biosensor Technologies, 3430 Tulln, Austria

[2]Univ. Lille, CNRS, Centrale Lille, Univ. Polytechnique Hauts-de-France, UMR 8520 - IEMN, F-59000 Lille, France

[3]CEST Competence Centre for Electrochemical Surface Technology, 2700 Wiener Neustadt, Austria

[4]Univ. Rennes, CNRS, ISCR –UMR 6226, Campus de Beaulieu, F-35000 Rennes, France

[5]Nanotechnology Research Centre (NTRC), The British University in Egypt (BUE), El-Sherouk City, Suez Desert Road, Cairo 11837, Egypt

[6]Department of Physics and Chemistry of Materials, Faculty of Medicine/Dental Medicine, Danube Private University, Krems, Austria

***Corresponding author:**

Wolfgang Knoll,
AIT Austrian Institute of Technology,
Tel+43 664 2351720, +4350550 4000,
E-Mail: wolfgang.knoll@ait.ac.at

Keywords:

Cardiac Troponin I; Biosensor; Surface-Plasmon Fluorescence Spectroscopy; Differential Pulse Voltammetry; Graphene Field-Effect Transistor

Received: 12 Feb 2021
Accepted: 01 Mar 2021
Published: 06 Mar 2021

Citation:

Knoll W. "On the Detection of cTnI - A Comparison of Surface-Plasmon Optical -, Electrochemical -, and Electronic Sensing Concepts". Ann Clin Med Case Rep. 2021; V6(2): 1-16

1. Introduction

"Cardiovascular diseases (CVDs) are the number one cause of death globally, taking an estimated 17.9 million lives each year. CVDs are a group of disorders of the heart and blood vessels and include coronary heart disease, cerebrovascular disease, rheumatic heart disease, and other conditions. Four out of five CVD deaths are due to heart attacks and strokes, and one third of these deaths occurs prematurely in people under 70 years of age" (cited from [1]). In addition, the total economic burden of CVD is enormous; the costs are expected to rise from approximately US$ 863 billion in 2010 to a staggering US$ 1,044 billion by 2030 worldwide [2].

Acute Myocardial Infarction (AMI), the most life-threatening version of acute coronary syndromes, causes severe irreversible tissue injury in the myocardium. The analysis of AMI primarily depends on electrocardiography (ECG) but only 57% of patients can be diagnosed correctly for AMI, and some of these patients can even show normal or non-diagnostic ECG when presented to the Emergency Room [3]. What is worse, 25% of AMI have happened without any symptoms like pain in the chest, back, or jaw. Therefore, a rapid, sensitive, and cost-efficient platform is needed to meet the diagnostic requirements in AMI detection [4].

Over the years, various marker molecules have been proposed for AMI diagnostics, among which were Aspartate Transaminase, Creatine Kinase, or Myoglobin [5]; although cardiac Troponin T (cTnT) or Troponin I (cTnI) have become the golden standards for myocardial infarction diagnostics and resulted in the development of the first bedside testing method [6]. During these years, there have been significant improvements in assays for cTn with regards to analytical sensitivity and precision at low concentrations [7]. The first-generation assay was not able to detect low plasma concentrations of troponin, while the second generation could identify injury earlier, but was not sensitive enough for healthy people. Finally, the third generation are high-sensitivity troponin assays and can reliably detect the low troponin levels in healthy individuals, as well as can differentiate patients with myocardial ischemia onset and early necrosis [8].

The corresponding cut off levels of cTnI in plasma for healthy patients were in the first generation 0.5 ng mL^{-1} (500 pg mL^{-1}). With

the advances in the development of high sensitivity troponin tests, the reference cutoff levels for cTnI in serum used to establish AMI has been progressively lowered and is currently in the range of 26 pg mL^{-1} [9]. This is about 100-1000 times lower than the cTnI level in patients with a clear positive test for AMI, with serum levels of cTnI as high as 5-50 ng mL^{-1} [10]. Upon the occurrence of an AMI, the death of cardiac myocytes causes the cTnI concentration up to 50 ng mL^{-1} within 3−6 h, and finally to a level around 550 ng mL^{-1} where it remains elevated for a few days, while that of other biomarkers will decline more rapidly [11].

The enormous clinical importance of having reliable methods and devices for testing cTnI, the scientific challenge that the low level of the marker in the blood of healthy patients means (at a molecular mass of cTnI of 24 kDa, 26 pg mL^{-1} correspond to 1.08 pM concentrations), and the commercial interest in sensitive, specific, robust, and affordable sensors spurred an unmatched race among biomolecular engineers for the development of new formats and examples of sensors that meet these requirements.

In this context, we intend to present in this short summary first a rather comprehensive (though probably not complete) list of examples in the literature of what other groups have reported. We will limit the compilation to the type of transduction principle that has been applied and the limit of detection (LoD) that has been achieved.

Then we use the results of our own studies to reflect on a few issues that one encounters in developing cTnI sensors. In particular, we will introduce 3 types of sensing concepts, based on:

- surface-plasmon optics (focusing on the most sensitive version offered by surface-plasmon fluorescence spectroscopy (SPFS)) [12],
- electrochemical assay, focusing on differential pulse voltammetry (DPV) [13],
- graphene FETs (gFET) as electronic sensors [14].

These sensors all measure in one way or another the surface coverage of the analyte molecules (cTnI in our case) that bind (reversibly) from solution to surface-immobilized receptors.

We present data for two types of receptors:

- antibodies [15],
- DNA aptamers [16].

Indeed, monoclonal antibody development involves several immunizations of a host animal, isolation of antibody-producing cells, followed by hybridoma selection and antibody production. Each step is time-intensive, with the entire process realistically taking four to six months. With aptamer selection being an *in vitro* process that is typically completed within 2-3 months, and together with increased shelf life of aptamers over antibodies with comparable affinity constants, these surface receptors lately are more intensively employed for sensing concepts [17].

In our examples, these receptors are immobilized using three types of chemistries typically applied by the community for the coupling of the receptor:

- Formation of self-assembled monolayers (SAMs) via thiol interaction with Au,
- π- π stacking interaction between 1-pyrenecarboxylic acid (PCA) and graphene followed by amide bond formation using EDC/NHS chemistry on the activated esters,
- Electroreduction of diazonium salts on graphene materials followed by Cu(I) based click-chemistry.

The substrates themselves represent three different types of substrate materials:

- Au for SPFS,
- Nitrogen-doped porous reduced graphene oxide (N-prGO) for the electrochemical studies,
- Graphene, prepared by chemical vapor deposition for the FETs.

And finally, we refer to two types of samples:

- cardiac Troponin I in PBS buffer, and
- clinical saliva samples.

We will discuss very briefly the essential basics of (and differences between) the various sensor platforms and compare the obtained results, in particular, with respect to the achieved LoDs in the light of the clinical requirements (cf. above).

2. Materials & Methods

2.1. Optical sensing

2.1.1. Surface-Plasmon Fluorescence Spectroscopy

For the direct optical analysis of the interaction between the protein and its receptors, antibodies in this case, an optical device combining surface plasmon resonance (SPR) [18] and surface plasmon-enhanced fluorescence spectroscopy (SPFS) [19, 20] in the Kretschmann configuration was used. The set-up consisted of a high refractive index (LaSF9) prism, optically matched to the sensor chip (50nm gold evaporated onto a LaSF9 glasss slide) and coupled to a flow cell. A laser beam at a wavelength of λ = 633 nm was directed to the prism base, and the reflected light collected by a photo detector in total internal reflection mode. The intensity was measured with a lock-in amplifier to observe changes in the SPR signal. At the appropriate angle of incidence, the enhanced electromagnetic field intensity generated by the resonant excitation of surface plasmons excites the chromophore-labelled analyte molecules bound from solution to the receptor units, immobilized on the sensor surface [21]. Their fluorescence signal was measured

(at λ = 670 nm) in this SPFS mode by a photomultiplier (H6240-01, Hamamatsu, Japan), linked to a photon counter. The beam intensity was reduced to 30-60 µW to avoid the bleaching of the employed chromophore Alexa Fluor 647. In order to separate the fluorescence light from scattered excitation light @ λ = 633 nm a set of filters (laser notch filter and fluorescence bandpass filter) was used.

2.1.2. Sensor Chip Preparation and Assay Development

LaSF9 high refractive index glass slides (Hellma Optics) were thermally evaporated-coated with 2 nm chromium and 50 nm gold, then incubated overnight in a 1:9 SH-PEG-COOH/ SH-PEG-OH (Sigma-Aldrich) solution for further surface functionalization. The SAM-coated gold slides were placed in the microfluidic flow cell with a volume of 4 µl. cTnI proteins were immobilized to the (EDC/NHS-) activated ester groups via amine coupling, and either monoclonal mouse or polyclonal goat antibodies (Abs) were rinsed across the cTnI capture layer. As a secondary antibody, AlexaFluor 647 conjugated anti-mouse or anti-goat antibodies were used at a concentration of 6 nM to monitor by SPFS the surface coverage of the primary ABs.

2.2. Electrochemical Sensing

2.2.1. Synthesis of N-prGO: The synthesis of prGO was achieved via dispersion of rGO powder (100 mg) in 30% H_2O_2 (100 mL), ultrasonicating for 30 min and heating for 12 h at 60 °C. The obtained solution was filtered and the recovered prGO powder was dialyzed to remove H_2O_2 and to separate from small sized graphene quantum dots [22].

The synthesis of N-prGO was carried out by mixing prGO powder and liquid ammonia (1:30 w/v) by ultrasonication before being transferred into a 50 mL Teflon coated stainless steel autoclave and heated for 24 h at 200 °C. The acquired solution was separated by filtration followed by washing with ethanol/water (1:1) mixture solution to completely remove the ammonia. The product was kept for drying in an oven at 60 °C overnight.

2.2.2. Preparation of the Electrodes: Glassy carbon electrodes (GC) were modified by drop-casting 5 µl of a suspension of N-prGO (1 mg ml^{-1} in water) and drying for 24 h in an oven at 60 °C. The formed GC/N-prGO electrodes were immersed in 0.1 M PBS (pH 7.0) and cycled 30 times between -1.5 V and +1.1 V at a scan rate of 0.1 V s^{-1} to stabilize the interface. Thereafter, to insure good reduction of the prGO, the potential was furthermore kept at -1.5 V for 3 min.

The GC/N-prGO electrode was immersed into a mixture of 1-pyrenecarboxylic acid (1 mM) and synthesised pyrene-PEG (1 mM) [23] with a ratio of 1:20 for 1 h at room temperature. The employed aptamer with the sequence 5'-NH_2-TTT TTT CGT GCA GTA CGC CAA CCT TTC TCA TGC GCT GCC CCT CTT A-3' was immobilized by first activating the carboxyl groups of 1-pyrenecarboxylic acid *via* immersion into a solution of EDC (15 mM)/ NHS (15 mM) in PBS (0.1 M, pH 7.4) for 30 min, followed by covalent coupling of the 5'-NH_2-modified aptamer (5 µL, 5 µM in PBS) by incubation for 40 min and washing (3 times) with PBS.

2.2.3. Differential Pulse Voltammetry: For the detection of cTnI, differential pulse voltammograms (DPV) [24] were recorded in a 5 mM $[Fe(CN)_6]^{4-}$ solution in 0.1 M PBS pH 7.4 within the potential range from -0.2 V to +0.5 V at a modulation amplitude of 5 mV and a step potential of 80 mV, step height of 15 mV and step time of 250 ms. Aptamer modified GC/N-prGO-COOH/PEG electrodes were immersed into cTnI standard solution or in samples containing cTnI for 30 min. After rinsing with PBS buffer (0.1 M, pH 7.4, three times), the electrodes were transferred into a 5 mM $[Fe(CN)_6]^{4-}$ solution in 0.1 M PBS pH 7.4 and a DPV signal was recorded. Following the measurements, immersion of the sensor into NaOH (0.1M, pH 12.0) for 20 min was used to regenerate the sensor interface.

2.3. Electronic Sensing Based on Graphene Field-Effect Transistors

2.3.1. Preparation of Functional Graphene Channels by "Click" Chemistry: For cTnI electronic sensing, we used a covalently-modified graphene field-effect transistor for the binding via "click" chemistry of a PEG-DNA aptamer mixture in a ratio of 1:2 [25]. Surface modification starts on a clean CVD-grown graphene after transferring it to an interdigitated electrodes device (Figure 1): first, electro-grafting of 4-((triisopropylsilyl)ethylenyl)benzenediazonium tetrafluoroborate (TIPS-Eth-ArN_2^+) (10 mM) in 0.1 M N-butylhexafluorophosphate (NBu_4PF_6) in acetonitrile was performed using cyclic voltammetry at a scan rate of 50 mV s^{-1} for five cycles between +0.30 V and -0.60 V vs. Ag/AgCl. The electrodes were rinsed with copious amounts of acetonitrile and acetone and gently dried. Before "click" chemistry, the TIPS protecting group was removed by the immersion of the Graphene-TIPS surface into tetrabutylammonium fluoride (TBAF, 0.1 M in THF) for 1h. The surface was then left for 15 min in a pure THF solution for cleaning. The deprotected surface was then exposed to a 1:2 mixture of methoxypolyethylene glycol azide (mPEG Azide, average MW 1000) and the DNA aptamer, using $CuSO_4$ (0.01 M) and L-ascorbic acid as reaction catalyst. The interface was treated with an aqueous solution of EDTA (10 mM) for 10 min to chelate any remaining Cu^{2+} residues and finally washed copiously with water and left to dry.

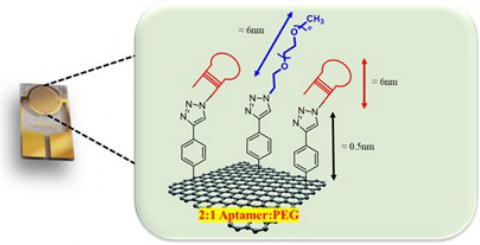

Figure 1: Graphene based field effect transistor surface-modified by anti-fouling PEG chains and aptamers for specific cTnI sensing

2.3.2. Electronic Read-out of cTnI Binding: Graphene transfer characteristics were recorded after each modification step using a Keithley 2400 source-meter with custom-made LabVIEW software. All measurements were performed using a MicruX flow cell made of PMMA with fixed flow channel geometry (16 µl), ensuring a defined flow rate of 50 µl min^{-1} to minimize mass transport limitation of the analyte to the sensor surface in all experiments [26]. Electrical measurements were performed by applying a 50 mV source–drain bias V_{DS} and sweeping the gate potential V_{GS} while monitoring the current between the drain and the source I_{DS}. A silver chloride wire (diameter 1 mm, Sigma-Aldrich) was used to operate the graphene-FET device in liquid gate configuration, with a constant gate bias of 0.2 V. The general procedure of the sensing experiment started with continuously flushing the pure buffer (PBS, 0.01x) until a stable baseline of drain current was established, followed by injection of the analyte at a constant flow rate [27].

3. Results

The long list of papers published on the detection of cTnI is given in Table 1, containing a total of 120 references, with the first paper published in 2004.

The spectrum of the applied detection principles is rather wide, with a clear focus on optical (including surface-plasmon resonance (SPR), fluorescence, colorimetric, fluorescence resonance energy transfer (FRET)), as well as electrochemical techniques (e.g., cyclic- or differential pulse- voltammetry, impedimetric protocols, electro-chemiluminescence, etc.). However, also a few exotic detection formats for the monitoring of cTnI as a marker for AMI events have been reported; e.g., surface-enhanced resonance Raman spectroscopy (SERRS), magneto-optics, single-photon detection, electro-acoustic principles, to mention but a few. In addition, several reports appear in the literature on the use of electrical or electronic concepts for cardiac marker sensing.

Concerning the transducer functionalization as a means to guarantee the mere specific recognition and binding of the analyte proteins, three receptor systems have been described; i.e., antibodies, peptides, and aptamers.

Most remarkable in this long list of references is the incredible spread of reported limits of detection (LoD), ranging from $7.7x10^{5}$ pg mL^{-1} to $4.8x10^{-4}$ pg mL^{-1}, thus covering 9 orders of magnitude! Given the current cut-off level for cTnI in healthy patients of 26 pg mL^{-1}, one half of the reported tests have only historical value and don't need to be considered further: no clinic would use any of these principles and protocols.

At the other end of the spectrum, extreme sensitivities seem to be offered with spectacular LoDs – but not for free: in all cases, the reported values are the result of extreme complexities with multiple amplification steps – totally useless for practical applications: doctors need simple and easy to apply tests and recipes. And not even from a scientific point of view any of these reports on "ultra-sensitive" sensors is helpful: none of the authors dares about trying to understand the basic physical principles that might operate in their experiment! The simple question: what is the molecular mechanism and/or a theoretical model by which one could understand that the sensor response changes by a factor of 3-5 (!) upon varying the cTnI concentration by 5-7 orders of magnitude [28-32] (Calling this "linear" is another story…). All reports refer to a bimolecular reaction between the ligand, cTnI, and its antibody or specific aptamer. A description of this reaction by a Langmuir model might be too simple; however, it would be a good starting point: it would explain that there might be a truly linear regime at concentrations well below the half-saturation concentration, i.e., the dissociation constant, K_d, for the specific receptor-ligand pair! And it would suggest that there should be a saturation behavior for analyte concentrations in the sample solution well-above this K_d-value.

In order to explain why it is so important to generate this model-based understanding of the molecular interactions on the sensor surface, we refer to our own work and summarize in the following experimental binding data that were collected by i) surface plasmon fluorescence spectroscopy, by ii) an electrochemical technique, i.e., differential pulse voltammetry, and by the most recent methodological developed in our laboratories, i.e., iii) an electronic read-out concept based on graphene field-effect transistors (gFETs).

3.1 Optical cTnI Sensing Based on Surface-Plasmon Fluorescence Spectroscopy

Because a direct detection format with mere SPR readout provided insufficient sensitivity, the first example that we present is an approach based on surface-plasmon fluorescence spectroscopy with a special inhibition immune assay [33]. As shown in Figure 2, this assay consisted of three steps: firstly, samples with known concentrations of cTnI were spiked in the bulk solution with mouse monoclonal anti-cTnI antibodies, each at a concentration of 2 nM, and incubated for 20 min (Figure 2(a)). Theses samples were then flowed for 20 min over the surface of a sensor chip that was prepared with cTnI proteins immobilized onto a mixed thiol SAM with active ester groups coupled to the amine moieties of the proteins (Figure 2(b)). And finally, after rinsing for 5 min, a 6 nM solution of a secondary Alexa Fluor 647-conjugated anti-mouse antibody was allowed to react with the affinity bound primary antibody (Figure 2(c)). After another 5 min of rinsing, the fluorescence sensor response ΔF was determined. Due to the competitive binding in the reaction vessel, the sensor response shows an increase with decreasing analyte concentration, as seen in Figure 2(d). In a solution with low concentration of cTnI analyte, most binding sites of the a-TNNI3 antibody are available and attach to the sensor surface with the immobilized cTnI. This way, a high fluorescence signal is seen after the reaction with the labelled secondary antibody. At a high concentration of the cTnI target analyte present in the bulk solution, the binding sites of the a-TNNI3 antibody are occupied, thus leading to low fluorescence signal on the sensor chip.

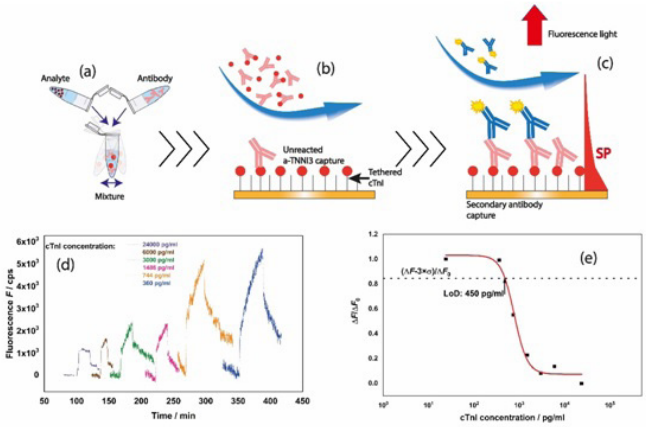

Figure2: Schematics of the competitive assay, consisting of (a) mixing of the analyte (of known concentrations for the calibration curve) with a known concentration of a primary antibody; (b) flowing the mixture across the chip surface of the sensor which was functionalized by a monolayer of immobilized cTnI; (c) rinsing the flow-cell with the fluorescently labelled secondary antibodies, and (d) recording the fluorescence signal of the binding of the secondary antibody. (e) fluorescence signal, taken from (d) as a function of the cTnI concentration in the bulk mixture.

The 3 σ-limit of detection (LoD) derived from the response of the fluorescence signals plotted as a function of the cTnI concentrations (Figure 2(e)) was 450 pg mL^{-1}, below the most recently clinically defined threshold for diagnostically relevant levels of cardiac troponins.

3.2. Electrochemical Determination of cTnI Levels by Differential Pulse Voltammetry

Carbon-based materials [34] are promising candidates for the sensitive detection of medically relevant markers like cTnI by electrochemical means [35]. We added lately to this field by proposing the use of nitrogen-doped porous reduced graphene oxide (N-prGO) [36] for detection and quantification of cTnI (Figure 3a). The good electrochemical conductivity (Figure 3b) of N-prGO, formed by a two-step process from reduced graphene oxide by first treatment with hydrogen peroxide (H_2O_2) and subsequent hydrolysis of the formed epoxy groups to hydroxyl groups, accompanied by C-C bond breaking to produce a rGO porous structure, is one important element in this sensor. Coupling of an aptamer, known for its high selectivity towards cTnI [37], via 1-pyrenecarboxylic acid and the presence of an antifouling element such as PEG-based pyrene ligand, are other important elements in this approach.

Addition of cTnI of different concentrations to these interfaces results in a decrease of the maximum current as recorded by differential pulse voltammetry with $[Fe(CN)_6]^{4-}$ as redox probe (Figure 4a). This change is proportional to the cTnI concentration between 1 pg mL^{-1} and 100 ng mL^{-1} with a detection limit of about 0.88 pg mL^{-1} (Figure 4b).

Interestingly, this sensor concept allows also for sensing of cTnI in

saliva samples of patients who reported chest pain. The sensitivity of the sensor changes when working in saliva due to the presence of a large variety of proteins and salts (Figure 4c), but a comparable LoD of 1 pg mL^{-1} could still be reached. The electrochemical response of a saliva sample of a healthy and an AMI diagnosed patient could be differentiated (Figure 4d). cTnI concentrations of below 1 pg mL^{-1} were determined for the healthy patients, while a cTnI level of 675 pg mL^{-1} was determined for the AMI diagnosed patients. In the case of the healthy patients, the quantitation limit of the sensor was just good enough to indicate that the concentration is below 1 pg mL^{-1}.

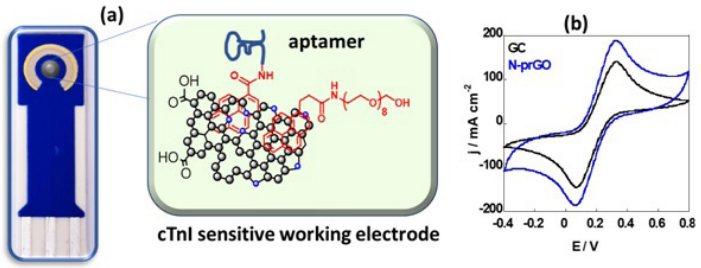

Figure 3: (a) Concept of the electrochemical cTnI sensor based on drop casting N-prGO onto the carbon working electrode followed by modification with 1-pyrenecarboxylic acid and poly (ethylene glycol) (PEG) modified pyrene ligand and covalent integration of an aptamer onto the1-pyrenecarboxylic acid functions. (b) Cyclic voltammograms recorded on GC (black), and GC coated with N-prGO (blue) using $[Fe(CN)_6]^{4-}$ (5 mM)/PBS (0.1M)) as redox mediator, scan rate = 100 mV s^{-1}.

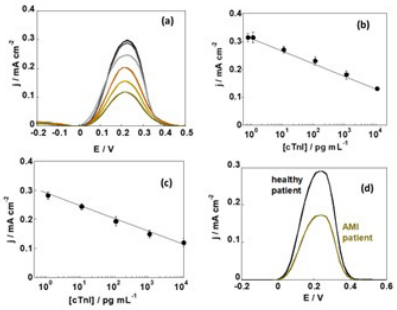

Figure 4: (a) Differential pulse voltammograms at various cTnI concentrations (0, 0.001, 0.01, 0.1, 1 and 10 ng mL^{-1}) in PBS ×1 (pH 7.4). (b) Calibration curve in PBS ×1 (pH 7.4). (c) Calibration curve for cTnI in human saliva samples spiked with different concentrations of cTnI. (d) DPV curves in saliva of patient samples with chest pain and diagnosed AMI and healthy ones as controls.

3.3. Electronic Sensing Based on Graphene Field-Effect Transistors

FET-based biosensors, properly functionalized by a selective receptor layer, will directly convert any biological interaction into an electrical signal [38], allowing also for real-time detection of cTnI with high sensitivity and selectivity. This measured current signal is due to the accumulation of charge carriers in the channel caused by a modulation of the gate potential, which in turn is influenced by the presence of the analyte bound to its receptor. In particular, graphene as a channel material in FETs has many interesting properties that make it attractive for biosensing including, high sensitivity to near surface charges and electric fields, excellent electrical characteristics (high mobility, high transfer kinetics, high conductivity, among others), as well as good mechanical properties and biocompatibility [39, 40].

After coupling the 2:1 aptamer: PEG layer by "click" chemistry to the graphene channel of the transistor (cf. section 2.c1), the transfer characteristics of the modified-graphene FET during exposure to cTnI solutions with concentrations ranging from 3 to 1000 pg mL^{-1} were recorded after stabilization with each concentration (Figure 5a). At different cTnI concentrations, an increase of the FET source-drain current is observed in the holes' regime and a decrease in the electrons' regime. This comes as a consequence of the positively charged molecules adsorbed onto the channel – since

cTnI has the isoelectric point at pH 9.87, it is positive in PBS at pH 7.4. This will induce a negative charge in the graphene channel, generating more electrons, leading them to become the majority carriers; the I_DV_G curve shifts to the left side due to graphene's n-doping, leading to a decrease of the central neutrality point (CNP) also known as Dirac point. This suggests that the decrease of the Dirac point value is attributed to the charge gating effect of the attached linker molecules and cTnI. The sensor response was analyzed at a gate voltage of 350 mV – at this value, the current for each cTnI concentration and for the PBS 0.01x baseline was extracted from the I_DV_G curve. By calculating $\Delta I_{DS} = I_{DS}$ ([cTnI]$_n$) – I_{DS} ($PBS_{0.01x}$), for each given concentration, n, in pg mL^{-1}, a calibration curve was obtained (Figure 5b). The fit of these data to a Langmuir model (black curve in (Figure 5(b)) gave a dissociation constant of K_d = 55 pg mL^{-1}. As judged from the minimal difference of the source-drain-current at V_G = 350 mV (cf. Figure 5a) between pure buffer and the 3 pg mL^{-1} solution we estimate a LoD = 1 pg mL^{-1}.

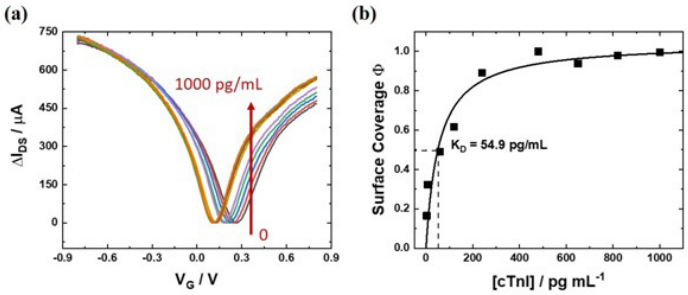

Figure 5: (a) Graphene transfer characteristics (ΔI_{DS}-*vs*-V_G curves) after stabilization with each cTnI concentration (0, 3, 6, 60, 120, 240, 480, 650, 820 and 1000 pg mL^{-1}) in 0.01x PBS (pH 7.4) without washing steps. (b) ΔI_{DS}, converted according to the Langmuir model to the corresponding surface coverage, Φ, as a function of the analyte concentration of the solution running through the flow cell.

4. Discussion

We start the discussion with a few fundamental remarks concerning the use of biosensors as analytical tools for monitoring the concentration of clinically relevant markers in body liquids like whole blood, plasma, urine, saliva, or others. For any one of the concepts developed for monitoring the cardiac marker cTnI that were reported in the literature (cf. Table 1) the optical, electrochemical or electronic transducers were all functionalized, each with a layer of specific receptor molecules. For cTnI, these receptors were either specific antibodies, peptides (derived from phage-display approaches), or aptamers. These functional coatings are optimized to serve a double purpose for the transducer that will be exposed to the analyte solution: on the one side, it offers specific sites with a typically high binding affinity for the analyte molecule of interest; and on the other side, it passivates the sensor surface by an anti-fouling coating which prevents all other molecules in the cocktail of the analyte solution from binding as well, thus preventing a possibly strong background sensor signal from non-specific binding events.

Upon exposure of such a functionalized transducer surface to the analyte solution (some of) the empty binding sites will be occupied by the association (binding) of the analyte molecules from the bulk. If the binding is reversible, i.e., if the analyte can also dissociate again, the surface coverage, i.e., the fraction of occupied binding sites of the receptor (mono-)layer establishes an equilibrium with the corresponding bulk concentration – which is the level of the marker of interest in the test sample. This one-to-one correlation between the bulk concentration of the marker and its surface density on the sensor surface is the basis for the quantitative evaluation of the marker concentration in the test solution from a measurement of its surface coverage on the transducer device used.

The sensitivity of any sensor depends critically on two factors: the first is the binding affinity of the analyte molecule to the receptor molecule. This receptor affinity can be quantified by an inhibition constant or K_d value, which indicates the bulk concentration required to occupy 50% of the receptor molecules on the transducer surface; hence, it is also called half-saturation constant. Obviously, the lower this constant, the lower the bulk concentration can be to reach half-saturation on the sensor. This is the motivation for the race towards high-affinity receptors, e.g., by the SELEX process for the development of high-affinity aptamers [41], or the search for high affinity antibodies [42].

The second factor that is crucial is a feature of the transducer itself and depends on its principle of operation: it reduces to the simple question: how low in coverage, well below half-saturation, can one still see a sensor signal upon the binding of only a few ligands to the receptor molecules. Given the broad diversity of transducer principles developed for biosensors, there

is no general answer to this question and depends heavily on the physics behind the transduction concept implemented. The only common feature frequently observed is the use of labels that are introduced with the sole purpose, i.e., to enhance the signal contribution of each analyte molecule to the overall sensor response. The well-established enzyme-linked immunosorbent assay (ELISA) is a classic example for that concept and was developed to enhance via enzymatic amplification the signal from each binding event.

For the examples for cTnI detection from our own group presented above, the fluorescence-labeling of the antibodies used in our surface-plasmon optical detection approach falls into this category: the binding of an antibody to the ligand cTnI is further enhanced by recording the fluorescence emission originating from a secondary chromophore-labeled (detection) antibody binding to the first one. The multiple cycling between the ground and the excited state of the chromophore with the emission of up to 2000 photons per second per dye molecule [43] represents an enhancement factor of the detection scheme that increases the sensitivity significantly. It should be pointed out that it is not the analyte that needs to be labelled, but the secondary antibody. Hence, this is not a serious limitation of this and similar techniques; however, it means an additional processing step. Similarly, the example given for the category of electrochemical sensors based on the modification of the differential pulse voltammetric signal upon the binding of cTnI to an aptamer binding layer depends on the surface coverage and thus generates a sensor signal that is strictly correlated with the binding events of interest. In this example, the mechanism for enhancement is the redox cycling of the mediator $[Fe(CN)_6]^{4-}$. Only the electronic sensing platform discussed as the third example monitors the binding of cTnI from a solution sample to the aptamer receptor layer by the direct impact of analyte molecules (and possibly the resulting impact on the receptor, e.g., a change in the charge distribution by a reorganization in the structure of the aptamer) on the source-drain current of a field-effect transistor tuned to an appropriate gate voltage (V_G = 350 mV in this case).

With this in mind, we are now turning to the surface-plasmon optical sensor data. The concept that we focus on is based on a particular format, an inhibition immuno-assay: the first step is the mixing of the sample solution of the appropriate antibody, the receptor R, of known concentration, c_R, with the marker molecules, the ligands L, at concentration, c_L. According to the reaction ([44], cf. also Figure 2(a)):

the concentration of the ligand-receptor complex, c_{RL}, is determined by the equilibrium constant, K_A, (the inverse of the dissociation constant (half-saturation constant), $K_d = k_d / k_a$,) given by the mass action law

$$K_A = c_{RL} / c_R \cdot c_L. \qquad \text{Eqn. (1)}$$

The unreacted, still empty receptor molecules together with the formed complexes are then rinsed through the flow cell across the transducer surface of the SPFS spectrometer (Figure 2(b)), bind to the surface-immobilized cTnI ligands, and are detected via a secondary chromophore- labeled antibody (Figure 2(c)), the fluorescence of which is monitored. For very low concentrations of the ligand in the reaction vessel, only a small fraction of the receptor molecules is occupied; hence, leads to a high fluorescence signal (cf. Figure 2(d)). Increasing successively the ligand concentration in the reaction vessel, occupies more and more of the receptors; hence, the fluorescence signal decreases (Figure 2(d)). The result is a titration curve of the receptor in the bulk solution of the reaction vessel (Figure 2(e)), the fit of which according to eqn. (1) yields the dissociation constant K_d = 840 pg mL^{-1} (corresponding to K_d = 35 pM). The 3σ- criterion for the limit of detection leads to LoD = 450 pg mL^{-1}. For the first generation of troponin assays in the clinic, this result was good enough; however, despite representing a very attractive high affinity constant for an antigen-antibody interaction, the progress in high-sensitivity troponin tests with their progressively lowered cut-off level for healthy patients nowadays asks for better performance assays. It should be pointed out, although, that it was not so much the affinity of the employed antibody that limits the applicability of the assay, it was the moderate LoD, compared to the K_d-value of the interaction that acts as the show stopper: because of the inversion of the signal generation – a low level of ligands in the bulk solution means a high fluorescence signal on the sensor and vice-versa - a relatively high background fluorescence at low analyte concentrations leads to a difference between K_d and LoD of only a factor of 2, very different from the best cases of an SPFS-based biosensor assay reported in the literature [45] where for the detection of a (fluorescently labelled) 196bp PCR amplicon by a PNA capture probe on the sensor surface, a LoD = 100 fM was achieved at a K_d value of 2.7 nM, i.e., a ratio of LoD / K_d = 1 / 30000!

The next example that we presented was based on differential pulse voltammetry with $[Fe(CN)_6]^{4-}$ as the redox mediator, and using a specific aptamer, taken from the literature [37] as the receptor system for cTnI binding to this sensor surface from the analyte solution. A key concept in electrochemical systems is the fact that the kinetics of the heterogeneous electron transfer is modulated upon ligand-analyte interactions. Using the negatively charged ferrocyanide redox couple $[Fe(CN)_6]^{4-}$ revealed that electron transfer is increasingly hindered upon interaction of the positively charged cTnI analyte (theoretical isoelectric point 9.87) with the surface linked aptamer most likely due to restricting the diffusion. With a LoD of 0.88 pg mL^{-1} in PBS and 1 pg mL^{-1} in saliva, this concept is a very attractive alternative to other techniques described in the literature. The simplicity of the method and the portable character of the sensor format makes, this approach appealing as point-of-care testing (POCT) device.

Table 1: Compilation of publications reporting on the detection of cTnI. Given are the LoD (all values scaled in units of pg mL^{-1}, with 24 pg mL^{-1} = 1 pM) and year of publication, together with the analytical technique applied: SPR, surface-plasmon resonance; CL, chemiluminescence; FRET, fluorescence recovery after photobleaching; SPFS, surface-plasmon fluorescence spectroscopy; ECL, electro-chemiluminescence; FET, field-effect transistor; SE(R)RS, surface-enhanced (resonance) Raman spectroscopy; SAW, surface acoustic wave.

Applied Technique		LoD pg ml^{-1}	Year	Ref.
Fluorescence	QD	770000	2008	[46]
Electrochemical	Peptides	340000	2010	[47]
Electrochemical		16000	2017	[48]
SPR	Au nanorod	10000	2009	[49]
SPR		6800	2011	[50]
CL	ELISA	5600	2007	[51]
Fluorescence	Aptamers	5000	2015	[52]
SPR		5000	2016	[53]
SPR		1400	2004	[54]
SPR		1250	2017	[55]
Electrochemical	Aptamers	1190	2014	[56]
Electrochemical	AuNPs	1000	2011	[57]
Electrochemical	Conducting paper	1000	2012	[58]
Chemiresistor	ZnO NP	1000	2016	[59]
Electrochemical	Antibody	800	2021	[60]
FRET		700	2009	[61]
Electrochemical	MIP	650	2016	[62]
Paramagnetic	Magnetic NPs	500	2007	[63]
SPFS	Antibody	450	2020	[64]
Electrochemical	AuNPs	250	2013	[65]
Impedimetric		200	2010	[66]
Electrochemical	AuNPs	200	2012	[67]
Colorimetric	Peptides/AuNP	200	2016	[68]
Electrochemical microchip		148	2007	[69]
ECL		110	2018	[70]
Fluorescence	Fluoro-microbead	100	2011	[71]
Electrochemical	Au and Ag	100	2013	[72]
Fluorescence	AMPPD-ALP	100	2014	[73]
Photonic Xtal	Antibodies	100	2014	[74]
FRET	Antibody	97	2020	75]
FET	Silicon nanowire	92	2012	[76]
Paramagnetic	Magnetic NPs	72	2009	[77]
Electrochemical		70	2016	[78]
Fluorescence	Aptamer	70	2018	[79]
SPR	Peptides	68	2011	[80]
ECL	AuNPs	60	2013	[81]
Electrochemical	Nanocomposites of AuNPs	50	2016	[82]
Electrochemical	Antibody	50	2020	[83]
Cyclic voltammetry		40	2018	[84]
Paramagnetic	Magnetic NPs	30	2010	[85]
Colorimetric	HRP	27	2009	[86]
Electrochemical		25	2015	[87]
Electrochemical	Antibody/Aptamer	24	2015	[37]
Electrochemical	Aptamer	24	2017	[88]
Electrochemical	DNA	24	2019	[89]
Electrochemical	Aptamer	23	2018	[90]
Fluorescence		16	2018	[91]
Electrochemical	Aptamer 1	16	2019	[92]
SERRS	AuNP	16	2020	[93]
SPR/electric	Antibody	15	2018	[94]
Electro-acoustic	Antibody	14	2020	[95]
Optomagnetic		11.7	2009	[96]
ELISA		10	2009	[97]
Colorimetric	AuNP	10	2010	[98]

Colorimetric	AuNPs	10	2010	[99]
Chemiresistor	SWCNT/ AuNP	10	2013	[100]
Potentiometric		10	2014	[101]
Electrochemical		10	2018	[102]
Electrochemical	Array of Au NPS Aptamers	8	2017	[103]
CMOS Transistor	Antibody	7.7	2014	[104]
Chemiresistor	Nanowire, Antibody	7.7	2015	[105]
Electrochemical	Aptamer	7.5	2019	[106]
SAW	AuNPs	6.2	2013	[107]
AlGaN/GaN transistor		6	2018	[108]
Electrochemical		6	2018	[109]
Electrochemical	Aptamer	5.7	2019	[110]
Optical	Antibody	5.7	2020	[111]
Fluorescence	Antibody	5.6	2020	[112]
Fluorescence	FITC	5	2011	[113]
SERS	Graphene-Au NP	5	2019	[114]
Electrical	Silicon nanowire	5	2016	[115]
Electrochemical	Aptamer	4.3	2019	[116]
Electrochemical	Pt nanoparticles	4.2	2014	[117]
Electrochemical	QD	4	2010	[118]
Electrochemical	Au NPs	3.4	2016	[119]
FET	ZnO NPs	3.24	2017	[120]
Electrochemical		2.4	2016	[121]
ELISA		2	2010	[122]
ECL	AuNPs	2	2011	[123]
Fluorescence	Europium(III)	2	2012	[124]
Chemiresistor	Antibody	1	2014	[125]
Chemiresistor	Antibody	1	2014	[126]
Impedimetric		1	2016	[127]
Impedimetric		1	2017	[128]
Electrochemical	Aptamer	1	2018	[129]
Electrochemical	Aptamer	1	2018	[36]
Electrochemical	Graphene-multi walled carbon	0.94	2015	[130]
CL	Antibody	0.84	2020	[131]
ECL	Au NPs	0.5	2015	[132]
ECL	Aptamer	0.48	2019	[133]
Electrochemical	Au NPs Ru-peptide	0.4	2014	[134]
Chemiresistor	Nanowire, Antibody	0.25	2012	[135]
Paramagnetic	Antibody	0.2	2007	[136]
Electrochemical		0.17	2018	[137]
SPR	Antibody	0.12	2020	[138]
Fluorescence	TiO2 nanotube array AM700	0.1	2012	[139]
Electrochemical	Aptamer	0.05	2020	[140]
Electrochemical		0.033	2019	[141]
ECL		0.016	2015	[142]
ECL	AuNPs	0.012	2017	[143]
Electrochemical		0.01	2011	[144]
Photoelectrochemical		0.0067	2018	[28]
ECL	Antibody	0.004	2019	[29]
Electrical	Aptamer	0.0024	2020	[30]
Fluorescence	Antibody	0.00084	2013	[31]
ECL	Antibody	0.00048	2019	[32]

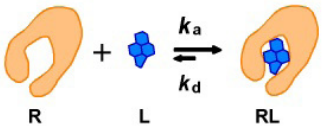

The last example from the set of techniques that we applied for the development of a sensitive cTnI test assay was based on a transistor device using graphene as the channel material that connects source and drain electrodes. The functionalization of this channel by a diazonium-based coupling strategy with the attachment of the cTnI-specific aptamer [37] by click chemistry leads to a very promising $I_D V_G$ behavior (cf. Figure 5(a)), indicating excellent mobilities in the device structure. Even more important is the very reproducible (and reversible [44]) shift of the individual $I_D V_G$-curves upon rinsing analyte solution through the flow cell. The observed behavior is given only by a shift of the Dirac point to lower positive voltages, in line with the understanding that the binding of the analyte protein leads to an aptamer/cTnI complex at the sensor surface that results in a gradual change of the surface potential at the channel/analyte solution interface that adds to the gate voltage.

By plotting the change of the source-drain current, I_{DS}, taken at a constant gate voltage of V_G = 350 mV as a function of the cTnI concentration, we observed a behavior that suggested an analysis in terms of a classic binding behavior: for low concentrations, the current increased linearly with the cTnI concentration, to then merge into a saturation behavior at higher concentrations (Figure 5(b)). Assuming a Langmuir binding model these data can be fitted with the dissociation constant as the only parameter, resulting in K_d = 55 pg mL^{-1} (corresponding to about 2.5 pM). This is a remarkably high affinity for an aptamer as receptor for a bio-affinity reaction and a good starting point for a very sensitive assay for clinical applications. The obtainable LoD is certainly better than 1 pg mL^{-1}, as judged from the clear difference of the $I_D V_G$-curves measured in bare PBS-buffer and after injecting a cTnI-solution with a concentration of only 3 pg mL^{-1}. With these limits, the approach falls definitely into the regime of assays with a clinically relevant resolution: the cut-off level of assays of even the third generation is defined as 26 pg mL^{-1} for healthy individuals.

5. Conclusion

In recent years, the cardiac marker, cTnI, obviously became a reference system heavily used by the community of biosensor developers to calibrate their broad range of transducer concepts and experimental setups. The result is a long list of publications dealing with just this one marker, quantifying its LoD as the clinically relevant parameter. As mentioned before, the range of LoD values reported in the literature is covering 9 orders of magnitude! However, a relatively large number of papers is only (at best) of historical value because todays cut-off requirements for clinical applications are at the level of 26 pg mL^{-1} (to be able to monitor also healthy patients), although one has to admit that the cut-off level was constantly decreasing over the years: what used to be a good technique for the detection of the cTnI level in patients' blood a few years ago is not acceptable any more today. Still, the list of reports with LoDs in line with the current clinical levels is impressive. Hence, a practitioner looking for a good detection concept for cTnI needs to take into consideration other factors of the test kit like the ease of operation, the robustness of the test kit, the costs, etc. Hence, it can be expected that even in the foreseeable future there will be new proposals for and reports about better devices that may eventually also be marketable and will find their way into the clinic of doctor's office. We, too, continue to work on that target.

6. Acknowledgement

Financial support from the Centre National de la Recherche Scientifique (CNRS), the University of Lille, the Hauts-de-France region, and the CPER "Photonics for Society", are acknowleged.

References

1. https://www.who.int/health-topics/cardiovascular-diseases#tab=tab_1
2. http://www.championadvocates.org/en/champion-advocates-programme/the-costs-of-cvd
3. McDonnell B, Hearty S, Leonard P, Richard O'Kennedy R. Cardiac biomarkers and the case for point-of-care testing. Clinical Biochem. 2009; 42(7–8): 549-61.
4. Han X, Li S, Peng Z, Othman AM, Leblanc R. Recent Development of Cardiac Troponin I Detection. ACS Sens. 2016; 1(2): 106–11
5. Szunerits S, Mishyn V, Grabowska I, Boukherroub R. Electrochemical cardiovascular platforms: Current state of the art and beyond. Biosens Bioelectron. 2019; 131: 287-98.
6. Hamm CW, Goldmann B, Heeschen C, Kreymann G, Berger J, Meinertz T. Emergency Room Triage of Patients with Acute Chest Pain by Means of Rapid Testing for Cardiac Troponin T or I. N. Engl. J. Med. 1997; 337: 1648-53.
7. Upasham S, Tanak A, Prasad S. Cardiac troponin biosensors: where are we now? Advanced Health Care Technologies. 2018; 4: 1-13.
8. https://www.mlo-online.com/continuing-education/article/21121636/implementation-of-highsensitivity-cardiac-troponin-into-clinical-practice.
9. Romiti GF, Cangemi R, Toriello F, Ruscio E, Sciomer S, Moscucci F, et al. Sex-Specific Cut-Offs for High-Sensitivity Cardiac Troponin: Is Less More? Cardiovasc Ther. 2019; 9546931.
10. Kontos MC, Anderson FP, Alimanrd R, Ornato JP, Tatum JL, Jesse RL. Ability of troponin I to predict cardiac events in patients admitted from the emergency department. J Am Coll Cardiol. 2000; 36(2000) 1818-23.
11. Maqsood A, Kaid K, Cohen M. Clinical Significance of Borderline Cardiac Troponin (cTnI) in Patients Presenting with Acute Coronary Syndrome who are Referred for Cardiac Catheterization. The Internet Journal of Cardiovascular Research. 2006; 4: 1-4.
12. Sergelen K, Fossati S, Turupcu A, Oostenbrink C, Liedberg B, Knoll W, et al. Plasmon field-enhanced fluorescence energy transfer for hairpin aptamer assay readout, ACS sensors. 2017; 2(7): 916-23.
13. Vasilescu A, Wang Q, Li M, Boukherroub R, Szunerits S. Aptamer-

Based Electrochemical Sensing of Lysozyme. Chemosensors. 2016; 4(2): 10.

14. Syu YC, Hsu WE, Lin CT. Review—Field-Effect Transistor Biosensing: Devices and Clinical Applications. ECS Journal of Solid State Science and Technology. 2018; 7(7): Q3196-207.
15. Saeed AFUH, Wang R, Ling S, Wang S. Antibody Engineering for Pursuing a Healthier Future. Front. Microbiol. 2017; 8: 495.
16. Zhang Y, Lai BS, Juhas M. Recent Advances in Aptamer Discovery and Applications, Molecules. 2019; 24(5): 941.
17. Bognár Z, Gyurcsányi RE. Aptamers against Immunoglobulins: Design,Selection and Bioanalytical Applications. Int. J. Mol. Sci. 2020; 21: 5748.
18. Knoll W. Interfaces and Thin Films as Seen by Bound Electromagnetic Waves. Ann. Rev. Phys. Chem. 1998; 49: 569-638.
19. Knoll W, Kasry A, Liu J, Neumann T, Niu L, Park H, et al. Surface Plasmon Fluorescence Techniques for Bio-Affinity Studies Handbook of Surface Plasmon Resonance, Eds. R.B.M. Schasfoort and Anna J. Tudos Chpt. 2008; 9: 275-312.
20. Liebermann T, Knoll W. Surface-plasmon field-enhanced fluorescence spectroscopy. Colloids and Surfaces A: Physicochemical and Engineering Aspects. 2000; 171(1-39): 115-30.
21. Yu F, Persson B, Lofas S, Knoll W. Atto-Molar Sensitivity of Surface Plasmon Fluorescence Spectroscopy, J. Am. Chem. Soc. 2004; 126: 8902-3.
22. Singh SK, Dhavale VM, Boukherroub R, Kurungot S, Szunerits S. N-doped porous reduced graphene oxide as an efficient electrode material for high performance flexible solid-state supercapacitor Appl Mater. Today. 2017; 8: 141-9.
23. Barras A, Szunerits S, Marcon L, Monfilliette-Dupont N, Boukherroub R. Functionalization of Diamond Nanoparticles Using "Click" Chemistry, Langmuir. 2010; 26: 13168-72.
24. Selvam SP, Chinnadayyala SR, Cho S, Yun K. Differential Pulse Voltammetric Electrochemical Sensor for the Detection of Etidronic Acid in Pharmaceutical Samples by Using rGO-Ag@SiO2/Au PCB. Nanomaterials. 2020; 10(7): 1368.
25. Mishyn V, Aspermair P, Leroux Y, Happy H, Knoll W, Boukherroub R, Szunerits S. "Click" Chemistry on Gold Electrodes Modified with Reduced Graphene Oxide by Electrophoretic Deposition. Surfaces. 2019; 2: 193-204.
26. Aspermair P, Mishyn V, Bintinger J, Happy H, Bagga K, Subramanian P, et al. Reduced graphene oxide–based field effect transistors for the detection of E7 protein of human papillomavirus in saliva. Anal. Bioanal. Chem. 2021; 413(3): 779-87.
27. Reiner-Rozman C, Larisika M, Nowak C, Knoll W. Graphene-based liquid-gated field effect transistor for biosensing: Theory and experiments. Biosens. Bioelectron. 2015; 70: 21-7.
28. Chen J, Kong L, Sun X, Feng J, Chen Z, Fan D, Wei Q. Ultrasensitive photoelectrochemical immunosensor of cardiac troponin I detection based on dual inhibition effect of Ag@Cu2O coreshell submicron-particles on CdS QDs sensitized TiO2 nanosheets. Biosens Bioelectron 2018; 117: 340-6.
29. Ye J, Zhu L, Yan M, Zhu Q, Lu Q, Huang J, et al. Dual-Wavelength Ratiometric Electrochemiluminescence Immunosensor for Cardiac Troponin I Detection. Analytical Chemistry. 2019; 91(2): 1524-31.
30. Zhang J, Lakshmipriya T, Gopinath SCB. Electroanalysis on an Interdigitated Electrode for High-Affinity Cardiac Troponin I Biomarker Detection by Aptamer–Gold Conjugates. ACS Omega. 2020; 5(40): 25899-905.
31. Lee S, Kang SH. Quenching Effect on Gold Nano-patterned Cardiac Troponin I Chip by Total Internal Reflection Fluorescence Microscopy. Talanta. 2013; 104: 32-8.
32. Yan M, Ye J, Zhu Q, Zhu L, Huang J, Yang X. Ultrasensitive Immunosensor for Cardiac Troponin I Detection Based on the Electrochemiluminescence of 2D Ru-MOF Nanosheets. Analytical Chemistry. 2019; 91(15): 10156-63.
33. Wang Y, Dostalek J, Knoll W. Long range surface plasmon-enhanced fluorescence spectroscopy for the detection of aflatoxin M1 in milk. Biosens. Bioelectron. 2009; 24: 2264-7.
34. Huang X, Yin Z, Wu S, Qi X, He Q, Zhang Q, et al. Graphen-Based Materials: Synthesis, Characterization, Properties, and Applications. Small. 2011; 14(7): 1876-902
35. Bai Y, Xu T, Zhang X. Graphene-based biosensors for detection of biomarkers. Micromachines. 2020; 11: 60.
36. Chekin F, Vasilescu A, Jijie R, Singh SK, Kurungot S, Iancu M, et al. Sensitive electrochemical detection of cardiac troponin I in serum and saliva by nitrogen-doped porous reduced graphene oxide electrode. Sensors Actuators B Chem. 2018; 262: 180-7.
37. Jo H, Gu H, Jeon W, Youn H, Her J, Kim SK, et al. Electrochemical aptasensor of cardiac troponin I for the early diagnosis of acute myocardial infarction, Anal. Chem. 2015; 87: 9869-75.
38. CHENG S. Detection of biomarkers using field effect transistor (FET)-based biosensors for disease diagnosis. 2015.
39. Ohno Y, Maehashi K, Matsumoto K. Label-Free Biosensors Based on Aptamer-Modified Graphene Field-Effect Transistors. J. Am. Chem. Soc. 2010; 132(51): 18012-3.
40. Kwong Hong D, sang T, et al. Chemically Functionalised Graphene FET Biosensor for the Label-free Sensing of Exosomes. Sci. Rep. 2019; 9(1): 211.
41. Szeto K, Craighead HG. Devices and approaches for generating specific high-affinity nucleic acid aptamers. Appl. Phys. Rev. 2014; 1: 031103.
42. Warszawski S, Borenstein Katz A, Lipsh R, et al. Optimizing antibody affinity and stability by the automated design of the variable light-heavy chain interfaces. PLoS Comput Biol. 2019; 15(8): e1007207.
43. Lakowicz, JR. Principles of Fluorescence Spectroscopy, Springer, 2006.
44. http://www.chemgapedia.de/vsengine/vlu/vsc/de/ch/13/vlu/kinetik/affinitaet/affinitaetsreaktionen.vlu/Page/vsc/de/ch/13/pc/kinetik/affinitaet/binkin.vscml.html.
45. Yao D, Yu F, Kim J, Scholz J, Nielsen PE, Sinner EK, Knoll W. Surface plasmon field-enhanced fluorescence spectroscopy in PCR product analysis by peptide nucleic acid probes. Nucleic Acids Research. 2004; 32: 22.

46. Stringer RC, Hoehn D, Grant SA. Quantum Dot-Based Biosensor for Detection of Human Cardiac Troponin I Using a Liquid-Core Waveguide. IEEE Sens. J. 2008; 8: 295-300.
47. Wu J, Cropek DM, West AC, Banta S. Development of a troponin I biosensorusing a peptide obtained through phage display, Anal. Chem. 2010; 82: 8235-43.
48. Sandil D, Kumar S, Arora K, Srivastava S, Malhotra B, Sharma S, Puri NK. Biofunctionalized nanostructured tungsten trioxide based sensor for cardiacbiomarker detection, Mater. Lett. 2017; 186: 202-5.
49. Guo ZR, Gu CR, Fan X, Bian ZP, Wu HF, Yang D, et al. Fabrication of Anti-human Cardiac Troponin I Immunogold Nanorods for Sensing Acute Myocardial Damage.Nanoscale Res. Lett. 2009; 4: 1428-33.
50. Kwon YC, Kim MG, Kim EM, Shin Y, Lee SK, Lee SD, et al. Development of a surface plasmon resonance-based immunosensorfor the rapid detection of cardiac troponin I, Biotechnol. Lett. 2011; 33: 921-7.
51. Torabi F, Mobini Far HR, Danielsson B, Khayyami M. Development of a plasma panel test for detection of human myocardial proteins by capillary immunoassay. Biosens Bioelectron. 2007; 22(7): 1218-23.
52. Dorraj GS, Rassaee MJ, Latifi AM, Pishgoo B, Tavallaei M. Selection of DNA aptamers against Human Cardiac Troponin I for colorimetric sensor based dot blot application. J. Biotechnol. 2015; 208: 80-6.
53. Pawula M, Altintas Z, Tothill IE. SPR detection of cardiac troponin T for acute myocardial infarction. Talanta. 2016; 146: 823-30.
54. Masson JF, Obando L, Beaudoin S, Booksh K. Sensitive and Real-Time Fiber-Optic-Based Surface Plasmon Resonance Sensors for Myoglobin and Cardiac Troponin I. Talanta. 2004; 62: 865-70.
55. Wu Q, Sun Y, Zhang D, et al. Ultrasensitive magnetic field-assisted surface plasmon resonance immunoassay for human cardiac troponin I. Biosens Bioelectron. 2017; 96: 288-93.
56. Jiang SH, Fan T, Liu LJ, Chen Y, Zhang XQ, Sha ZL, et al. The Detection of cTn I by The AptamerBiosensor. Progress in Biochemistry and Physics. 2014; 41: 916-20.
57. Ahammad AS, Choi YH, Koh K, Kim JH, Lee JJ, Lee M. Electrochemical detection of cardiac biomarker troponin I at gold nanoparticle-modified ITO electrode by using open circuit potential, Int. J. Electrochem. Sci. 2011; 6: 1906-16.
58. Jagadeesan KK, Kumar S, Sumana G. Application of conducting paper forselective detection of troponin, Electrochem. Commun. 2012; 20: 71-4.
59. Tan CM, Arshad MK, Fathil MFM, Adzhri R, Nuzaihan M, Ruslinda AR, et al. Interdigitated Electrodes Integrated with Zinc Oxide Nanoparticles for Cardiac Troponin I Biomarker Detection. IEEE-ICSE2016 Proc. 2016.
60. Gupta A, Sharma SK, Pachauri V, Ingebrandt S, Singh S, Sharma AL, et al. Sensitive impedimetric detection of troponin I with metal–organic framework composite electrode. RSC Advances. 2021; 11(4): 2167-74.
61. Mayilo S, Kloster MA, Wunderlich M, et al. Long-range fluorescence quenching by gold nanoparticles in a sandwich immunoassay for cardiac troponin T. Nano Lett. 2009; 9(12): 4558-63.
62. Zuo J, Zhao X, Ju X, Qiu S, Hu W, Fan T, et al. A new molecularly imprinted polymer (MIP)-based electrochemical sensor for monitoring cardiac troponin I (cTnI) in the serum, Electroanalysis 2016; 28: 2044-9.
63. Kiely J, Hawkins P, Wraith P, Luxton R. Paramagnetic Particle Detection for Use with an Immunoassay Based Biosensor. IETSci., Meas. Technol. 2007; 1: 270-5.
64. Bozdogan A, El-Kased RF, Jungbluth V, Knoll W, Dostalek J, Kasry A. Development of a specific troponin I detection system with enhanced immune sensitivity using a single monoclonal antibody. Royal Society Open Science. 2020; 7(10): 200871.
65. Periyakaruppan A, Gandhiraman RP, Meyyappan M, Koehne JE. Label-free detection of cardiac troponin-I using carbon nanofiber based nanoelectrode arrays, Anal. Chem. 2013; 85: 3858-63.
66. Silva BVM, Cavalcanti IT, Mattos AB, Moura P, Sotomayor MDPT, Dutra RF. Disposable immunosensor for human cardiac troponin Tbased on streptavidin-microsphere modified screen-printed electrode.Biosens Bioelectron. 2010; 26(3): 1062-7.
67. Bhalla V, Carrara S, Sharma P, Nangia Y, Suri CR. Gold nanoparticles-mediated label-free capacitance detection of cardiac troponin I, Sens. Actuators B. 2012; 161: 761-8.
68. Liu X, Wang Y, Chen P, McCadden A, Palaniappan A, Zhang J, et al. Peptide Functionalized Gold Nanoparticles with Optimized Particle Size and Concentration for Colorimetric Assay Development: Detection of Cardiac Troponin I. ACS Sens. 2016; 1(12): 1416-22.
69. Ko S, Kim B, Jo SS, Oh SY, Park JK. Electrochemical detection of cardiac troponin I using a microchip with the surface-functionalized poly(dimethylsiloxane) channel, Biosens. Bioelectron. 2007; 23: 51-9.
70. Jiang M-H, Lu P, Lei Y-M, Chai Y-Q, Yuan R, Zhuo Y. Selfaccelerated electrochemiluminescence emitters of Ag@SnO2 nanoflowers for sensitive detection of cardiac troponin T. Electrochim Acta. 2018; 271: 464-71.
71. Song SY, Han YD, Kim K, Yang SS, Yoon HC. A Fluoro-Microbead Guiding Chip for Simple and Quantifiable Immunoassay of Cardiac Troponin I (cTnI). Biosens. Bioelectron. 2011; 26: 3818-24.
72. Shumkov AA, Suprun EV, Shatinina SZ, Lisitsa AV, Shumyantseva VV, Archakov AI. Gold and silver nanoparticles for electrochemical detection ofcardiac troponin I based on stripping voltammetry. Bio-NanoScience. 2013; 3: 216-22.
73. Liu J, Zhang LL, Wang YS, Zheng Y, Sun S H. An improved portable biosensing system based on enzymatic chemiluminescence and magnetic immunoassay for biological compound detection. Measurement. 2014; 47: 200-6.
74. Zhang B, Morales AW, Peterson R, Tang L, Ye JY. Label-free Detection of Cardiac Troponin I with a Photonic Crystal Biosensor. Biosens. Bioelectron. 2014; 58: 107-13.
75. Lee KW, Kim KR, Chun HJ, Jeong KY, Hong DK, Lee KN, et al. Time-resolved fluorescence resonance energy transfer-based lateral flow immunoassay using a raspberry-type europium particle and a single membrane for the detection of cardiac troponin I. Biosensors and Bioelectronics. 2020; 163: 112284.
76. Kong T, Su R, Zhang B, Zhang Q, Cheng G. CMOS-compatible, label-freesilicon-nanowire biosensors to detect cardiac troponin I for acute

myocardialinfarction diagnosis, Biosens. Bioelectron. 2012; 34: 267-72.

77. Bruls DM, Evers TH, Kahlman JAH, van Lankvelt PJW, Ovsyanko M, Pelssers EGM, et al. Rapid Integrated Biosensor for Multiplexed Immunoassays Based on Actuated Magnetic Nanoparticles. Lab Chip. 2009; 9: 3504-10.
78. Kazemi SH, Ghodsi E, Abdollahi S, Nadri S. Porous graphene oxide nanostructure as an excellent scaffold for labelfree electrochemical biosensor: detection of cardiac troponin I. Mater Sci Eng C Mater Biol Appl. 2016; 69: 447-52.
79. Liu D, Lu X, Yang Y, Zhai Y, Zhang J, Li L. A novel fluorescent aptasensor for the highly sensitive and selective detection of cardiac troponin I based on a graphene oxide platform. Anal Bioanal Chem. 2018; 410(18): 4285-91.
80. Kwon YC, Kim MG, Kim EM, et al. Development of a surface plasmon resonance-based immunosensor for the rapid detection of cardiac troponin I. Biotechnol Lett. 2011; 33(5): 921-7.
81. Li F, Yu Y, Cui H, Yang D, Bian Z. Label-free electrochemiluminescence immunosensor for cardiac troponin I using luminol functionalized goldnanoparticles as a sensing platform. Analyst. 2013; 138: 1844-50.
82. Liu G, Qi M, Zhang Y, Cao C, Goldys EM. Nanocomposites of goldnanoparticles and graphene oxide towards an stable label-freeelectrochemical immunosensor for detection of cardiac marker troponin-I,Anal. Chim. Acta. 2016; 909: 1-8.
83. Vasantham S, Alhans R, Singhal C, Nagabooshanam S, Nissar S, Basu T, et al. Paper based point of care immunosensor for the impedimetric detection of cardiac troponin I biomarker. Biomedical Microdevices. 2020; 22(1).
84. Rezaei B, Shoushtari AM, Rabiee M, Uzun L, Mak WC, Turner APF. An electrochemical immunosensor for cardiac troponin, I using electrospun carboxylated multi-walled carbon nanotube -whiskered nanofibres. Talanta. 2018; 182: 178-6.
85. Dittmer WU, Evers TH, Hardeman WM, Huijnen W, Kamps R, de Kievit P, et al. Rapid, High Sensitivity, Point-Of-Care Test for Cardiac Troponin Based on Optomagnetic Biosensor. Clin. Chim. Acta. 2010; 411: 868-73.
86. Cho IH, Paek EH, Kim YK, Kim JH, Paek SH. Chemiluminometric Enzyme-Linked Immunosorbent Assays (ELISA)-on-a-Chip Biosensor Based on Cross-Flow Chromatography. Anal.Chim. Acta. 2009; 632: 247-55.
87. Horak J, Dincer C, Qelibari E, Bakirci H, Urban G. Polymer-modified microfluidic immunochip for enhanced electrochemical detection of troponinI, Sens. Act. 2015; 209: 478-85.
88. Jo H, Her J, Lee H, Shim YB, Ban C. Highly sensitive amperometric detection of cardiac troponin I using sandwich aptamers and screen-printed carbon electrodes. Talanta. 2017; 165: 442-8.
89. Lee T, Lee Y, Park SY, Hong K, Kim Y, Park C, et al. Fabrication of electrochemical biosensor composed of multi-functional DNA structure/Au nanospike on micro-gap/PCB system for detecting troponin I in human serum. Colloids Surf B Biointerfaces. 2019; 175: 343-50.
90. Qiao X, Li K, Xu J, Cheng N, Sheng Q, Cao W, et al. Novel electrochemical sensing platform for ultrasensitive detection of cardiac troponin I based on aptamer-MoS2 nanoconjugates. Biosens Bioelectron. 2018; 15; 113: 142-7.
91. Cai Y, Kang K, Li Q, Wang Y, He X. Rapid and sensitive detection of cardiac troponin I for point-of-care tests based on red fluorescent microspheres Molecules. 2018; 23: 1102.
92. Sun D, Luo Z, Lu J, Zhang S, Che T, Chen Z, Zhang L. Electrochemical dual-aptamer-based biosensor for nonenzymatic detection of cardiac troponin I by nanohybrid electrocatalysts labeling combined with DNA nanotetrahedron structure. Biosens Bioelectron. 2019; 134: 49-56.
93. Tu D, Holderby A, Coté GL. Aptamer-based surface-enhanced resonance Raman scattering assay on a paper fluidic platform for detection of cardiac troponin I. J. Biomed. Opt. 2020; 25(9): 097001.
94. Han X, Kojori HS, Leblanc RM, Kim SJ. Ultrasensitive Plasmonic Biosensors for Real-Time Parallel Detection of Alpha-L-Fucosidase and Cardiac-Troponin-I in Whole Human Blood. Analytical Chemistry. 2018; 90(13): 7795-9.
95. Peng J, Song G, Niu H, Wang P, Zhang X, Zhang S, Chen D. Detection of cardiac biomarkers in serum using a micro-electromechanical film electroacoustic resonator. Journal of Micromechanics and Microengineering. 2020; 30(7): 075011.
96. Bruls DM, Evers TH, Kahlman JAH, et al. Rapid integrated biosensor for multiplexed immunoassays based on actuated magnetic nanoparticles.Lab Chip. 2009; 9(24): 3504-10.
97. Cho IH, Paek EH, Kim YK, Kim JH, Paek SH. Chemiluminometric enzyme-linked immunosorbent assays (ELISA)-on-a-chip biosensor based on cross-flow chromatography. Anal Chim Acta. 2009; 632(2): 247-55.
98. Choi DH, Lee SK, Oh YK, Bae BW, Lee SD, Kim S, et al. A Dual Gold Nanoparticle Conjugate-BasedLateral Flow Assay (LFA) Method for the Analysis of Troponin I.Biosens. Bioelectron. 2010; 25: 1999-2002.
99. Wu WY, Bian ZP, Wang W, Zhu JJ. PDMS gold nanoparticle compositefilm-based silver enhanced colorimetric detection of cardiac troponin I, Sens.Actuators B. 2010; 147: 298-303.
100. Rajesh, Sharma V, Puri NK, Singh RK, Biradar RM, Mulchanadani A. Label-free detection of cardiac troponin-I using gold nanoparticles functionalized single-walled carbon nanotubes based chemiresistive biosensor. Appl. Phys. Lett. 2013; 103: 203703.
101. Pedrero M, Campuzano S, Pingarrón JM. Electrochemical biosensors for the determination of cardiovascular markers: a review. Electroanalysis. 2014; 26(6): 1132-53.
102. Sandil D, Srivastava S, Malhotra B, Sharma S, Puri NK. Biofunctionalized tungsten trioxide-reduced graphene oxide nanocomposites for sensitive electrochemical immunosensing of cardiac biomarker. J Alloys Compd. 2018; 763: 102-10.
103. Negahdary M, Behjati-Ardakani M, Sattarahmady N, Yadegari H, Heli H. Electrochemical aptasensing of human cardiac troponin I based on an array of gold nanodumbbells-Applied to early detection of myocardialinfarction, Sensors and Actuators B: Chemical. 2017; 252: 62-71.
104. Yen PW, Huang CW, Huang YJ, Chen MC, Liao HH, Lu SS, et al. A device design of an integrated CMOS poly-silicon biosensor-on-chip

to enhance performance of biomolecular analytes in serum samples. Biosens. Bioelectron. 2014; 61: 112-8.

105. Shen SH, Wang IS, Cheng H, Lin CT. An enhancement of high-k/oxide stacked dielectric structure for silicon-based multi-nanowire biosensor in cardiac troponin I detection. Sens. Act. 2015; 218: 303-9.
106. Sun D, Lin X, Lu J, Wei P, Luo Z, Lu X, Chen Z, Zhang L. DNA nanotetrahedron-assisted electrochemical aptasensor for cardiac troponin I detection based on the co-catalysis of hybrid nanozyme, natural enzyme and artificial DNAzyme. Biosens Bioelectron. 2019; 142.
107. Lee J, Lee Y, Park JY, Seo H, Lee T, Lee W, et al. Sensitive and reproducible detection of cardiactroponin I in human plasma using a surface acoustic wave immunosensor,Sens. Actuators. 2013; 178: 19-25.
108. Sarangadharana I, Regmia A, Chena YW, Hsua CP, Chena PC, Changb WH, et al. High sensitivity cardiac troponin I detection in physiological environment using AlGaN/GaN High Electron Mobility Transistor (HEMT) Biosensors. Biosens. Biolelectron. 2018; 100: 282-9.
109. Yan H, Tang X, Zhu X, Zeng Y, Lu X, Yin Z, et al. Sandwich-type electrochemical immunosensor for highly sensitive determination of cardiac troponin I using carboxylterminated ionic liquid and helical carbon nanotube composite as platform and ferrocenecarboxylic acid as signal label. Sensors Actuators B Chem. 2018; 277: 234-40.
110. Luo Z, Sun D, Tong Y, Zhong Y, Chen Z. DNA nanotetrahedron linked dual-aptamer based voltammetric aptasensor for cardiac troponin I using a magnetic metal-organic framework as a label. Mikrochim Acta. 2019; 186(6): 374.
111. Wang Y, Yang Y, Chen C, Wang S, Wang H, Jing W, et al. One-Step Digital Immunoassay for Rapid and Sensitive Detection of Cardiac Troponin I. ACS Sensors. 2020; 5(4): 1126-31.
112. Wu M, Zhang X, Wu R, Wang G, Li G, Chai Y, et al. Sensitive and Quantitative Determination of Cardiac Troponin I Based on Silica-Encapsulated CdSe/ZnS Quantum Dots and a Fluorescence Lateral Flow Immunoassay. Analytical Letters. 2020; 53(11) 1757-73.
113. Aslan K, Grell TA. Rapid and Sensitive Detection of Troponin I in Human Whole Blood Samples by Using Silver Nanoparticle Films and Microwave Heating. Clin. Chem. 2011; 57: 746-52.
114. Fu X, Wang Y, Liu Y, Liu H, Fu L, Wen J, et al. A graphene oxide/gold nanoparticle-based amplification method for SERS immunoassay of cardiac troponin I. Analyst. 2019; 144: 1582-9.
115. Kim K, Park C, Kwon D, Kim D, Meyyappan M, Jeon S, Lee JS. Silicon nanowire biosensors for detection of cardiac troponin I (cTnI) with high sensitivity, Biosens. Bioelectron. 2016; 77: 695-701.
116. Lopa NS, Rahman MM, Ahmed F, Ryu T, Sutradhar SC, Lei J, et al. Simple, low-cost, sensitive and label-free aptasensor for the detection of cardiac troponin I based on a gold nanoparticles modified titanium foil. Biosens Bioelectron. 2019; 126: 381-8.
117. Singal S, Srivastava AK, Biradar AM, Mulchandani A. Ptnanoparticles-chemical vapor deposited graphene composite basedimmunosensor for the detection of human cardiac troponin I, Sens. ActuatorsB. 2014; 205: 363-70.
118. Zhou F, Lu M, Wang W, Bian ZP, Zhang JR, Zhu JJ. Electrochemical Immunosensor for Simultaneous Detection of Dual Cardiac Markers Based on a Poly(Dimethylsiloxane)-Gold Nanoparticles Composite Microfluidic Chip: A Proof of Principle. Clin. Chem. 2010; 56: 1701-7.
119. Wang B, Jing R, Qi H, Gao Q, Zhang C. Label-free electrochemical impedancepeptide-based biosensor for the detection of cardiac troponin I incorporatinggold nanoparticles modified carbon electrode, J. Electroanal. Chem. 2016; 781: 212-7.
120. Fathil MFM, Md Arshad MK, Ruslinda AR, Gopinath SBC, Nuzaihan M, Adzhri MNR, et al. Substrate-gate coupling in ZnO-FETbiosensor for cardiac troponin I detection, Sens. Actuators. 2017; 242: 1142-54.
121. Wang B, Jing R, Qi H, Gao Q, Zhang C. Label-free electrochemical impedance peptide-based biosensor for the detection of cardiac troponin I incorporating gold nanoparticles modified carbon electrode. J Electroanal Chem. 2016; 78: 212-7.
122. Park JP, Cropek DM, Banta S. High affinity peptides for the recognition of the heart disease biomarker troponin I identified using phage display.Biotechnol Bioeng. 2010; 105(4): 678-86.
123. Shen W, Tian D, Cui H, Yang D, Bian Z. Nanoparticle-basedelectrochemiluminescence immunosensor with enhanced sensitivity forcardiac troponin I using N-(aminobutyl)-N-(ethylisoluminol)-functionalizedgold nanoparticles as labels, Biosens. Bioelectron. 2011; 27: 18-24.
124. Jarvenpaa ML, Kuningas K, Niemi I, Hedberg P, Ristiniemi N, Pettersson K, et al. Rapid and Sensitive Cardiac Troponin I Immunoassay Based on Fluorescent Europium(III)-Chelate-Dyed Nanoparticles. Clin. Chim. Acta. 2012; 414: 70-5.
125. Tuteja K, Priyanka SK, Bhalla V, Deep A, Paul AK, Suri CR. Graphene-gated biochip for the detection of cardiac marker Troponin I. Anal. Chim. Acta. 2014; 809: 148-54.
126. Tuteja SK, Sabherwal P, Deep A, Rastogi R, Paul AK, Suri CR. Biofunctionalized rebar graphene (f-RG) for label free detection of cardiac marker troponin I. ACS Appl. Mat Interfaces. 2014; 6(17): 14767-71.
127. Singal S, Srivastava AK, Gahtori B, Rajesh. Immunoassay for troponin I using a glassy carbon electrode modified with a hybrid film consisting of graphene and multiwalled carbon nanotubes and decorated with platinum nanoparticles. Microchim Acta. 2016; 183(4): 1-10.
128. Shanmugama NR, Muthukumarb S, Chaudhry S, Anguianao J, Prasad S. Ultrasensitive nanostructure sensor arrays on flexible substrates for multiplexed and simultaneous electrochemical detection of a panel of cardiac biomarkers. Biosens Bioelectron. 2017; 89: 764-72.
129. Grabowska I, Sharma N, Vasilescu A, Iancu M, Badea G, Boukherroub R, et al. Electrochemical Aptamer-Based Biosensors for the Detection of Cardiac Biomarkers. ACS Omega. 2018; 3(9): 12010-8.
130. Singal S, Srivastava AK, Dhakate S, Biradar AM, Rajesh R. Electroactive graphene-multi-walled carbon nanotube hybrid supported impedimetric immunosensor for the detection of human cardiac troponin-I. RSC Adv 2015; 5(92): 74994-5003.
131. Han GR, Ki H, Kim MG. Automated, Universal, and Mass-Producible Paper-Based Lateral Flow Biosensing Platform for High-Performance Point-of-Care Testing. ACS Applied Materials & Interfaces. 2020; 12(1) 1885-94.
132. Dong M, Li M, Qi H, Li Z, Gao Q, Zhang C. Electrogeneratedchemiluminescence peptide-based biosensing method for cardiac troponin

Iusing peptide-integrating Ru (bpy) 3 2+-functionalized gold nanoparticles asnanoprobe, Gold Bull. 2015; 48: 21-9.

133. Saremi M, Amini A, Heydari H. An aptasensor for troponin I based on the aggregation-induced electrochemiluminescence of nanoparticles prepared from a cyclometallated iridium(III) complex and poly(4-vinylpyridine-co-styrene) deposited on nitrogen-doped graphene. Mikrochim Acta. 2019 22; 186(4): 254.
134. Shan M, Li M, Qiu XY, Qi HL, Gao Q, Zhang CX. Sensitive Electrogenerated Chemiluminescence Peptide-based Biosensor for the Determination of Troponin I with Gold Nanoparticles Amplification. Gold Bull. 2014; 47: 57-64.
135. Lee I, Luo X, Huang J, Cui XT, Yun M. Detection of Cardiac Biomarkers Using Single Polyaniline Nanowire-Based Conductometric Biosensors. Biosens. 2012; 2: 205-20.
136. Todd J, Freese B, Lu A, Held D, Morey J, Livingston R, et al. Ultrasensitive Flow-Based Immunoassays Using Single-Molecule Counting. Clin. Chem. 2007; 53: 1990-5.
137. Zhang T, Ma N, Ali A, Wei Q, Wu D, Ren X. Electrochemical ultrasensitive detection of cardiac troponin I using covalent organic frameworks for signal amplification. Biosens Bioelectron. 2018; 119: 176-81.
138. Çimen D, Bereli N, Günaydın S, Denizli A. Detection of cardiac troponin-I by optic biosensors with immobilized anti-cardiac troponin-I monoclonal antibody. Talanta. 2020; 219: 121259.
139. Kar P, Pandey A, Greer JJ, Shankar K. Ultrahigh Sensitivity Assays for Human Cardiac Troponin I Using TiO2 Nanotube Arrays. Lab Chip. 2012; 12: 821-8.
140. Mi X, Li H, Tan R, Tu Y. Dual-Modular Aptasensor for Detection of Cardiac Troponin I Based on Mesoporous Silica Films by Electrochemiluminescence/Electrochemical Impedance Spectroscopy. Analytical Chemistry 2020; 92(21): 14640-7.
141. Lv H, Zhang X, Li Y, Ren Y, Zhang C, Wang P, et al. An electrochemical sandwich immunosensor for cardiac troponin I by using nitrogen/sulfur co-doped graphene oxide modified with Au@Ag nanocubes as amplifiers. Mikrochim Acta. 2019; 186(7): 416.
142. Xu Z, Dong Y, Li J, Yuan R. A ferrocene-switched electro-chemiluminescence „off-on" strategy for the sensitive detection of cardiac troponin I based on target transduction and a DNA walking machine. Chem Commun (Camb). 2015; 51(76): 14369-72.
143. Zhang L, Xiong C, Wang H, Yuan R, Chai Y. A sensitiveelectrochemiluminescence immunosensor for cardiac troponin I detection based on dual quenching of the self-enhanced Ru(II) complex by folic acid andin situ generated oxygen, Sens. Actuators B. 2017; 241: 765-72.
144. Akanda MR, Aziz MA, Jo K, Tamilavan V, Hyun MH, Kim S, Yang H. Optimization of phosphatase-and redox cycling-based immunosensors and its application to ultrasensitive detection of troponin I, Anal. Chem. 2011; 83: 3926-33.

6.4: Polyclonal aptamer libraries as binding entities on a graphene FET based biosensor for the discrimination of apo- and holo- binding protein 4

Ann-Kathrin Kissmann‡, Jakob Andersson‡, **Anil Bozdogan‡**, Valerie Amann, Markus Krämer, Hu Xing, Heinz Fabian Raber, Dennis H. Kubiczek, Patrik Aspermair, Wolfgang Knoll and Frank Rosenau. Nanoscale Horiz., 2022, 7, 770 DOI: 10.1039/D1NH00605C

(‡ Contributed equally)

First author paper: Together with A.K.K. and J.A., I participated in formulating the experimental design for the gFET, undertaking the experiment, interpreting the results, drafting the initial manuscript, creating figures, and reviewing and revising the final paper. Specifically, my role was paramount in the development of the assay for the gFET sensor. I experimented with various immobilization techniques at multiple pH levels, designed the biosensor for ensuing detection, and executed gFET experiments. A.K.K., V.A., and M.K. took part in constructing and characterizing the aptamer library and played a significant role in writing the manuscript. P.A., F.R., and W.K. made valuable contributions to the experiment's design and the manuscript's composition.

In this study, we demonstrate that polyclonal aptamer libraries against two isoforms of retinol binding protein 4 (RBP4) can be used for GFET functionalization, discriminating retinol-loaded or empty RBP4, which can serve as a marker for diabetes development. This biosensor showcases the potential of aptamers as highly sensitive interfaces in GFET-based sensors for future diagnostic platforms, with applications in medical diagnostics and environmental health monitoring.

Nanoscale Horizons

ROYAL SOCIETY OF CHEMISTRY

COMMUNICATION

View Article Online
View Journal | View Issue

Cite this: *Nanoscale Horiz.*, 2022, **7**, 770

Received 17th November 2021,
Accepted 28th April 2022

DOI: 10.1039/d1nh00605c

rsc.li/nanoscale-horizons

Polyclonal aptamer libraries as binding entities on a graphene FET based biosensor for the discrimination of apo- and holo-retinol binding protein 4†

Ann-Kathrin Kissmann,‡[a] Jakob Andersson,‡*[b] Anil Bozdogan,‡[bc] Valerie Amann,[a] Markus Krämer,[a] Hu Xing,[a] Heinz Fabian Raber,[a] Dennis H. Kubiczek,[a] Patrik Aspermair,[b] Wolfgang Knoll[bd] and Frank Rosenau*[a]

Oligonucleotide DNA aptamers represent an emergently important class of binding entities towards as different analytes as small molecules or even whole cells. Without requiring the canonical isolation of individual aptamers following the SELEX process, the focused polyclonal libraries prepared by this *in vitro* evolution and selection can directly be used to label their dedicated targets and to serve as binding molecules on surfaces. Here we report the first instance of a sensor able to discriminate between loaded and unloaded retinol-binding protein 4 (RBP4), an important biomarker for the prediction of diabetes and kidney disease. The sensor relies on two aptamer libraries tuned such that they discriminate between the protein isoforms, requiring no further sample labelling to detect RBP4 in both states. The evolution, binding properties of the libraries and the functionalization of graphene FET sensor chips are presented as well as the functionality of the resulting biosensor.

New concepts

Covalent surface modification of GFETs with nanoscale affinity entities like aptamers has recently been demonstrated as advantageous over non-covalent functionalization strategies. The stable and robust surfaces resulting from covalent grafting of specific binding molecules are expected to become versatile and cheap devices for biosensing applications. In this work, we show that polyclonal aptamer libraries against the two isoforms of retinol-binding protein 4 (RBP4) can be used for GFET functionalization to discriminate retinol-loaded or empty RBP4. Empty RBP4 can serve as a marker during diabetes development, which is currently not yet used in clinical routine. Thus, a respective biosensor represents not only an attractive tool for early diabetes diagnostics, but also demonstrates the power of aptamers as highly sensitive sensing interfaces of GFET-based sensors in future sensing (clinical) diagnostic platforms. We believe that due to the simplicity of library evolution and efficiency of covalent chemical grafting onto the graphene layers of GFETs will open new avenues for these electronic devices to become standard (bio-) sensors for a broad range of applications in medical diagnostics and environmental health monitoring.

Introduction

Retinol binding protein 4 (RBP4) is a serum protein, which belongs to the lipocalin ligand binding protein family.[1] It serves as a transporter in the blood for all-*trans*-retinol (vitamin A alcohol) and other retinoids like retinal or retinoid acid from hepatic retinoid stores to peripheral tissues of the body.[2] RBP4 is expressed in the liver and circulates in blood serum,[3] where normal levels of the protein can range from 40 to 60 μg mL^{-1} in humans.[4] Under physiological conditions, mainly ligand-bound RBP4 (holo-RBP4), approximately 90% of blood RBP4,[5] circulates in an 1 : 1 : 1 complex with transthyretin (TTR) (Scheme 1) and all-*trans*-retinol as its stability is further enhanced and RBP4 is prevented from extensive loss throughout glomerular filtration and catabolism in the kidneys.[6,7] Under healthy conditions, the RBP4 expression is tightly regulated and after the transport of retinol to its target cells the remaining unbound RBP4 (apo-RBP4) is rapidly filtered out and the protein is cleared from the serum.[8] However, the amount of RBP4 can be increased in the serum as a consequence of diseases like obesity,[9] chronic kidney disease,[10] insulin resistance,[11] and type 2 diabetes mellitus.[12] Depending on the level of elevation of the concentration of a certain RBP4 isoform or disbalances of RBP4 to retinol ratios, various reactions affecting the human health state can be triggered.[13] Recent studies showed, that especially apo-RBP4 contributes in adipose tissue to the development of

[a] *Institute of Pharmaceutical Biotechnology, Ulm University, Albert-Einstein-Allee 11, 89081 Ulm, Germany. E-mail: frank.rosenau@uni-ulm.de*
[b] *AIT Austrian Institute of Technology GmbH, Giefinggasse 4, 1210 Vienna, Austria. E-mail: jakob.andersson@ait.ac.at*
[c] *CEST Kompetenzzentrum für Elektrochemische Oberflächentechnologie GmbH, Viktor Kaplan Straße 2, Wiener Neustadt, Austria*
[d] *Danube Private University, Steiner Landstraße 124, 3500 Krems an der Donau, Austria*

† Electronic supplementary information (ESI) available. See DOI: https://doi.org/10.1039/d1nh00605c

‡ These authors contributed equally.

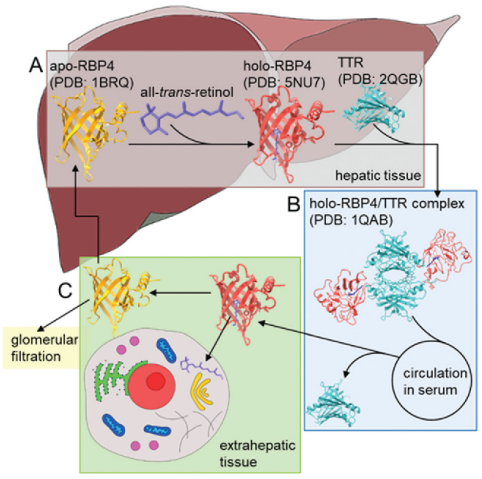

Scheme 1 RBP4-mediated transport of all-*trans*-retinol in blood serum from stores in the liver to extrahepatic peripheral tissue. (A) Secretion of RBP4 from the rough endoplasmatic reticulum of hepatocytes to the blood serum. Binding of apo-RBP4 with retinol and subsequent complexation of holo-RBP4 with transthyretin (TTR) forms a 1 : 1 : 1 holo-RBP4/TTR complex. Release into the serum is mediated by retinol availability, the conformational change upon retinol-binding is supposed to trigger the release. (B) Delivery of retinol from hepatic retinoid stores to peripheral extrahepatic tissues during periods of inadequate vitamin A intake. Transport of the holo-RBP4/TTR complex in blood serum to target cells, there the complex is cleaved to release holo-RBP4. (C) RBP4-associated retinol uptake by peripheral tissue due to specific interactions of holo-RBP4 with RBP4-receptors on the surface of target cells. Free RBP4 is either cleared by glomerular filtration or returned to hepatic stores afterwards.

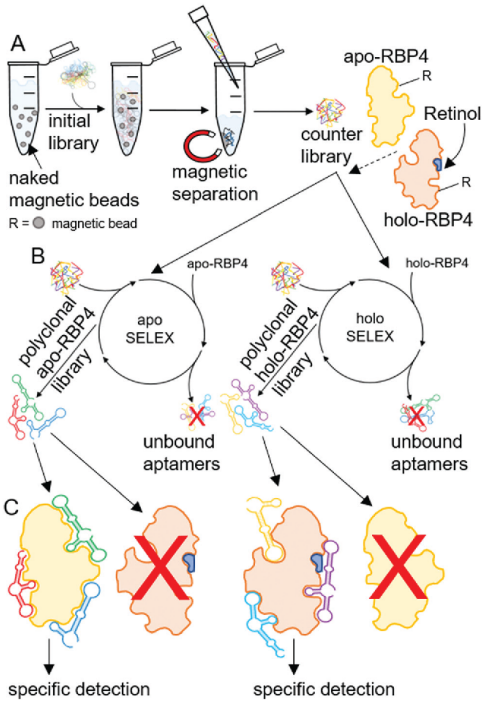

Scheme 2 SELEX based evolution of focused aptamer libraries for specific detection of apo- or holo-RBP4. (A) Initial counter selection by incubation of an initial aptamer library (~6×10^{14} individual aptamers), containing 40 randomized nucleotides flanked by two primer binding sites, with naked Dynabeads® M-280 tosyl-activated resulting in an aptamer 'counter library' with reduced amounts of aptamers with specificity against the naked beads. (B) Selection of specific polyclonal aptamer libraries by SELEX against apo- or holo-RBP4. Reduction of sequence diversity by incubating the counter selected aptamer library first with naked beads and subsequent with the target proteins (bound to Dynabeads® M-280 tosyl-activated (indicated as 'R')) and aptamers exhibiting an adequate three-dimensional structure bind to the targets. The remaining unbound aptamers are subsequently removed, the bound aptamers are then eluted from the target proteins, amplified by ePCR and the undesired complementary strands are removed prior to the next SELEX round. (C) Specific target detection by binding of focused aptamer libraries. Exclusive binding of polyclonal apo-RBP4 aptamers to apo-RBP4 and of holo-RBP4 aptamers to holo-RBP4.

an inflammatory state, which may result in insulin resistance.[14,15] Likewise, patients suffering from type 2 diabetes mellitus may exhibit moderate plasma RBP4 levels, but their level of free RBP4 in proportion to retinol is increased indicating an imbalance in ratios as a crucial factor.[16] Nowadays, several enzyme-linked immunosorbent assays (ELISAs) are commercially available the for detection of RBP4 in human serum, but they lack accuracy and are insufficient for the quantification of high concentrations of RBP4.[17] Hence, quantitative western blotting is used as the standard procedure for the detection of serum RBP4, especially in insulin-resistant states.[12] Typically only the amount of total RBP4 is measured and no further differentiation in isoforms is made. In order to overcome these restrictions and to create a methodology allowing to discriminate between apo- and holo-RBP4 the development of specific binding molecules with distinct affinities either for the apo- or the holo-protein would be an attractive amendment of the current existing RBP4 specific diagnostic technologies.

Since their introduction more than 20 years ago, nucleic acid aptamers have become serious alternatives, which offer considerable additional technical options making them increasingly attractive for different applications compared to antibodies or antibody derivatives, as they can serve as promising binding molecules in techniques requiring highly specific detection and quantification of target molecules.[18] Aptamers are single-stranded oligonucleotides like RNA or single-stranded DNA (ssDNA) with surprising physical and chemical stability, high specificity and affinity in combination with low overall immunogenicity, they can acquire different secondary and tertiary structures and are capable to bind defined targets.[19] High-affinity aptamers can be evolved and isolated from large random sequence libraries. In this selection process, performed completely *in vitro*, called systematic evolution of ligands by exponential enrichment (SELEX), repeated rounds of target binding

and PCR mediated amplification aptamers with binding affinity are successively enriched (Scheme 2).[20] Additionally, to reduce the sequence space of the random nucleotide library, an initial elimination of nonspecific oligonucleotides by a counter selection using only the target carrier material prior to the selection process leads to a so called 'counter library' with enhanced selectivity. Counter-selections against the carrier material before each round of selection also enable increased specificity towards the target protein, since otherwise in the selection step aptamers would not only be selected against the immobilized target, but also against its carrier material. Aptamers can be selected against a wide range of target structures including proteins,[21] whole cells, and microorganisms,[22,23] small molecules and chemical compounds like metal ions.[24] They can not only be used in diverse fields such as diagnostics,[25] biomarker discovery,[26] imaging agents,[27] drug delivery,[28] and as pharmaceutical compounds in molecular therapy,[29,30] but they are also attractive molecules for the construction of binding entities in technical devices like electronic biosensors[31] on which predominantly antibodies or antibody derivatives have been used.[32–34]

Recently, we have shown that as a significant simplification of the aptamer textbook procedures, where the overall aim is to isolate and characterize individual aptamer sequences before they are used for applications, already focused polyclonal libraries can not only be used directly after sufficient enrichment, but can even outperform single aptamers.[23] Thus, the use of focused polyclonal aptamer libraries can be expected to be advantageous due to higher precision based on the larger sequence space available for productive target recognition and increased performance in sensor technologies and diagnostics.

In order to specifically detect and quantify serum RBP4 such focused polyclonal aptamer libraries were evolved in an iterative SELEX process with recombinant purified target RBP4 proteins immobilized on magnetic particles (Scheme 2) in combination with fluorescence monitoring of the success of this molecular evolution process ("FluMag-SELEX").[35] Therefore, each round of aptamer evolution started by a counter-selection step using naked magnetic beads prior to selection steps using apo- or holo-RBP4 coated magnetic beads. The aim was to create the possibility to differentiate between RBP4 isoforms (*i.e.* the apo- and holo-RBP4) and therefore two independent focused aptamer libraries were successfully evolved simultaneously against both apo- and holo-RBP4. The selective and precise quantification of RBP4 isoforms plays an important role in early diagnostics and in the reduction of either the level of serum apo- or holo-RBP4, as well as balancing impairments in RBP4 to retinol ratios. Exclusive specific binding of both polyclonal aptamer libraries to their dedicated targets was used for the subsequent development of aptamer-based apo-RBP4 and holo-RBP4 biosensors based on electrolyte-gated field effect transistors (EG-FETs).

EG-FET devices have been used extensively in biosensing applications, for example, to detect microRNA,[36] DNA[37] biomarkers for heart failure,[38] cancer,[39] biotin in the pM range,[40] and urea.[41] We have also recently developed a highly sensitive method of detecting the E7-protein for human papillomavirus implicated in carcinogenesis.[31]

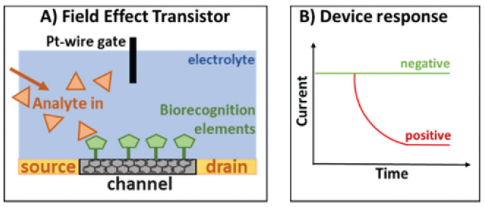

Scheme 3 (A) Typical configuration of an EG-FET. (B) Response of the device when there is no target analyte (green) and when the target analyte is present (red).

One of the primary benefits of EG-FET sensing devices is that they do not require target labelling with fluorescent or redox probes. Both the sensor chips and the read-out equipment are low cost and therefore highly suitable for use in point-of-care settings and in low socioeconomic areas where expertise and laboratory environments are not readily available.

An EG-FET is based on the same principle as a metal oxide FET: a source and drain electrode are separated by a semiconducting channel (Scheme 3). By applying a voltage at the gate electrode, channel conductivity is changed, modulating the current flowing between the source and drain electrodes. Biorecognition elements (antibodies, antigens, proteins or aptamers) can be deposited on the channel and when the target analyte binds, the change in dielectric layers at the interface between the channel and the electrolyte changes. As a result, the mobility of charge carriers in the channel is also changed.[42] At a constant gate voltage, binding events on the channel can therefore be observed as a change in the source–drain current (I_{DS}), therefore changing the gate voltage coupling to the channel will alter the source–drain current. We deposited the previously developed aptamer libraries on reduced graphene oxide field-effect transistors (rGO-FETs, a sub-class of EG-FET devices) using a previously developed methods.[31]

This platform also allows simultaneous optical and electronic sensing when the platinum wire gate electrode is replaced with a planar gold surface, achieving additional insight.[43]

Results and discussion

Recombinant RBP4 production in *E. coli* and purification from cell extracts

Competent cells of the expression strain *E. coli* BL21 (DE3) were transformed freshly prior to RBP4 over-expression and grown for 5 h after induction with IPTG, and the cell growth was monitored photometrically. After its biotechnological production, cell harvest, and cell lysis almost no RBP4 was isolated from lysate supernatants but remained in the insoluble fraction (Fig. S1A, ESI†). This recombinant protein expressed in *E. coli* requires a denaturation and refolding process to be active and ready for retinol/retinal binding, as the formation of inclusion bodies was described for recombinant RBP4 previously.[44] It is not unusual that foreign proteins aggregate as inclusion bodies

after high level over-expression in *E. coli*.[45] Several factors like a strong promotor system or a high target gene copy number favour a higher rate of recombinant protein expression leading to inclusion bodies formation.[46] Those can typically be dissolved under strongly denaturing conditions (*e.g.* urea) followed by incubation with the diluted denaturant in excess to enable protein refolding.[47,48] Therefore, RBP4 was recovered according to Wang *et al.* from inclusion bodies as a soluble protein by dissolving the cell pellets in a denaturation buffer containing 8 M urea and subsequent refolding steps. It could be observed as a band with an apparent molecular mass of 21 kDa (Fig. S1A, ESI†). After all refolding steps, the resulting protein solution was submitted to size exclusion chromatography (SEC) for further purification. The collected fractions, assumed to contain purified RBP4, were analyzed by SDS-PAGE in Fig. S1C (ESI†), there single bands at a molecular mass of ~21 kDa represented RBP4. The corresponding protein concentrations (Fig. S1B, ESI†) were calculated by the ChromLab Software and a total yield of ~12 mg RBP4 was gained after urea extraction and purification from inclusion bodies harvested from 1 L culture.

Ligand binding properties and functionality of apo-RBP4

The functionality of the purified RBP4 was further confirmed by determining its capacity to specifically bind increasing amounts of all-*trans*-retinal. Varying concentrations of retinal were added to a constant amount of the recombinant apo-RBP4. This mixture was incubated under exclusion of light and the quenching of intrinsic tryptophan fluorescence was monitored. The amount of apo-RBP4 in the reaction mixture decreased until only ligand-bound RBP4 was present after complexation with all-*trans*-retinal (Fig. S1D, ESI†). Interaction between RBP4 and retinal was confirmed, as the retinal quenched the intrinsic RBP4 tryptophan fluorescence due to energy transfer to the bound ligand. After binding, retinal is known to be incorporated into the binding cavity of the β-barrel of RBP4, where the polar groups remain solvent exposed.[2] High affinity binding of all-*trans*-retinal to *E. coli*-derived RBP4 was confirmed previously by spectral analysis. There, fluorescence quenching by binding increasing concentrations of retinal was monitored demonstrating the specific interaction at a single binding site.[49] In order to select aptamer libraries against apo- or holo-RBP4, first immobilization of proteins on magnetic Dynabeads M-280 tosyl-activated was performed. Covalent coupling of the tosyl-groups on the surface of the magnetic beads with primary amino groups of apo-RBP4 was performed as described by the manufacturer. To verify the coating with apo-RBP4 or holo-RBP4, the intrinsic tryptophan fluorescence emission was monitored at 340 nm with an excitation at 280 nm. Fluorescence was measured of apo-RBP4, apo- or holo-RBP4 coated beads, retinal, and naked magnetic beads (Fig. S1E, ESI†). Afterwards, to confirm retinal binding of holo-RBP4, emission was monitored at 490 nm with an excitation at 350 nm. The immobilization could be verified, as apo-RBP4 coated beads showed similar tryptophan fluorescence as single apo-RBP4 and intrinsic holo-RBP4 fluorescence was quenched after complexing apo-RBP4 immobilized on magnetic tosyl-beads with retinal. In comparison, signals gained by holo-RBP4 coated beads and by unbound retinal were similar. Uncoated naked magnetic beads exhibited no signals after fluorescence measurements, as buffers were used purely in the coating process.

Evolution of aptamer libraries specific for RBP4 isoform and verification of their specificities

With the aim to develop a methodological tool for the specific quantification of serum apo- and holo-RBP4, polyclonal ssDNA aptamer libraries were evolved during an iterative FluMag-SELEX over a total of eight selection rounds. In order to differentiate between the RBP4 forms, two independent focused ssDNA aptamer libraries were selected in a simultaneous SELEX process against both RBP4 isoforms. These polyclonal aptamer libraries that bind to either apo-RBP4 or holo-RBP4 were successfully selected from a random ssDNA library containing $\sim 6 \times 10^{14}$ individual aptamers with 40 randomized nucleotides flanked by two primer binding sites (23 nt each). The specificity was increased by early counter selection measures in which non-specific oligonucleotides were eliminated by using empty (or "naked") magnetic beads prior to each selection round. During the individual rounds of the FluMag-SELEX, the aptamers were Cy5-labelled *via* labelled PCR primers and analyzed fluorescently afterwards. To verify the evolution progress, defined amounts of aptamers (10 pmol) from each SELEX round were incubated with apo- or holo-RBP4-coated magnetic beads after the selection process. The libraries against apo-RBP4 were incubated for 30 min at 25 °C with apo-RBP4-coated magnetic beads and the holo-RBP4 libraries with holo-RBP4-coated beads and analyzed fluorescently after elution. The amount of eluted aptamers increased with each selection round indicating the progress of the enrichment process (Fig. 1A). The resulting two focused polyclonal aptamer libraries were further analyzed after the final selection round for specific target binding. The affinity binding characteristics of both final aptamer libraries were examined by analysis using apo- or holo-RBP4 coated magnetic beads as well as naked beads. Therefore, 10 pmol of round eight aptamer libraries were used for each of the RBP4 binding assays. The binding assays were performed using the apo-RBP4 library to specifically distinguish apo-RBP4 immobilized on magnetic beads from holo-RBP4 and the naked beads negative control. Then, the final polyclonal holo-RBP4 library was analyzed similar in order to specifically detect holo-RBP4.

As expected, both aptamer libraries were confirmed to specifically and efficiently bind their dedicated targets. Only marginal signals were exhibited by the apo-RBP4 library for holo-RBP4 and magnetic beads (Fig. 1B), but high specificity was observed for the holo-RBP4 aptamer library (Fig. 1B).

In addition, the highly selective target binding of both aptamer libraries was visualized using fluorescence microscopy. Therefore, 30 pmol of each aptamer library were incubated for 30 min with RBP4-coated magnetic beads as well as with naked beads as negative controls. Afterwards, images were taken under transmitted light to visualize the magnetic beads and to detect target binding. Exclusive target binding of apo-RBP4 aptamers was observed visually, as only fluorescence

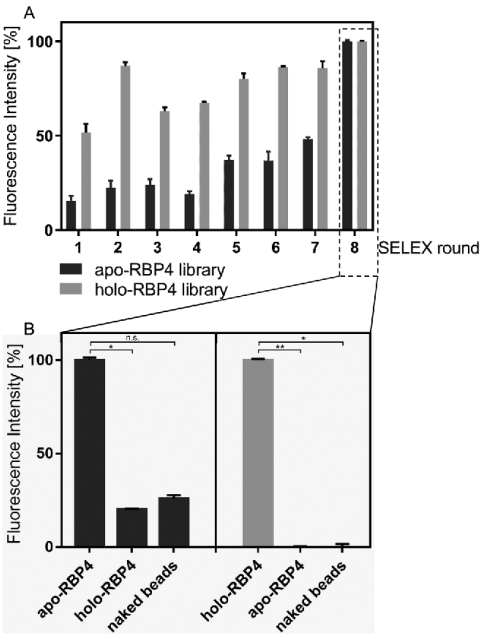

Fig. 1 Characterization of specific RBP4 binding to Cy5-labelled aptamer libraries. (A) RBP4 ssDNA aptamer libraries enrichment. Black bars, increased binding of selected aptamers to apo-RBP4 during SELEX. Grey bars, increased binding of aptamers to holo-RBP4 during SELEX. The evolution progress was monitored using fluorescence measurement at an excitation of 635 nm with an emission at 670 nm. (B) Specificity analysis of the final polyclonal aptamer libraries. Binding of aptamers against apo-RBP4 or holo-RBP4 to both apo- and holo-RBP4 as well as to naked Dynabeads® M-280 tosyl-activated. All experiments were performed using 10 pmol aptamers, 13.6 μg apo- or holo-RBP4 and 0.68 mg magnetic beads, fluorescence was monitored at an excitation of 635 nm with an emission at 670 nm. Error bars symbolize standard deviations of measurements conducted in triplicates. P values <0.05 were considered significant. * denotes $P < 0.05$, ** <0.01, n.s. not significant.

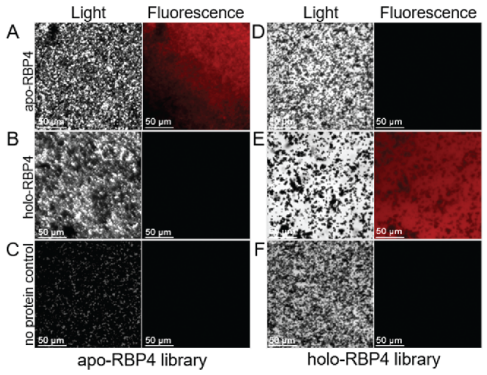

Fig. 2 Fluorescence microscopic analysis of specific RBP4 binding to Cy5-labelled aptamer libraries. (A) Binding of apo-RBP4 aptamers to apo- and (B) holo-RBP4 as well as to (C) naked Dynabeads® M-280 tosyl-activated. (D) Binding of holo-RBP4 aptamers to apo- and (E) holo-RBP4 as well as to (F) naked Dynabeads® M-280 tosyl-activated. All experiments were performed using 30 pmol aptamers, 13.6 μg apo- or holo-RBP4 and 0.68 mg magnetic beads. Images were monitored using a Leica DMi8 coded (Leica Microsystems CMS GmbH, Wetzlar, Germany) at ×40 magnitude under transmitted light and using the Y5 filter (excitation: 590–650 nm and emission: 662–738 nm) for fluorescence imaging.

signals were observed after the binding to apo-RBP4 coated magnetic beads (Fig. 2A).

As expected, beads coated with holo-RBP4 did not show any red fluorescence (Fig. 2B), indicating the differentiation between both RBP4 forms by the apo-RBP4 library. Likewise, highly specific target recognition was observed for the holo-RBP4 aptamer library. Red fluorescence signals could be observed after the binding of these aptamers to their dedicated target holo-RBP4 (Fig. 2D) and, as predicted, no signals were obtained after the incubation with apo-RBP4-coated beads (Fig. 2E). Moreover, both aptamer libraries exhibited no binding to the magnetic beads indicated by no fluorescence signals (Fig. 2C and F). These visual fluorescence signals additionally show the rapid and efficient labelling properties of both polyclonal aptamer libraries and furthermore the discriminating ability of them both between apo- and holo-RBP4.

Specific electrical sensing of apo- and holo-RBP4 using rGO-FETs

To assess the performance of aptamer libraries in biosensing applications, they were used as biorecognition element on an electrolyte-gated reduced graphene oxide field effect transistor (EG-rGO-FET). Chips were fabricated using a previously optimized protocol.[50] Measurements were made in a Micrux all-in-one flow cell using an Ag/AgCl electrode as gate. Special aptamer libraries were prepared with primers bearing an amine functional group at the 5′-end. This aptamer library was then immobilized *via* EDC–NHS coupling on a pyrene-carboxylic acid functionalized reduced graphene oxide surface using previously published protocols (see Scheme 4).[31] Analyte binding alters the charge transfer characteristics of the device which can be measured *via* 'I_DV_G-curves' in which the gate voltage (V_G) is swept from −0.5 to 0.5 V and the source–drain current I_{DS} is recorded. Higher voltages were not tested to avoid damaging biological components. Shifts in I_DV_G characteristics are caused by differences in charge carrier mobility originating from changes in the charge distribution at the channel-electrolyte interface.[51] The charge distribution is altered during binding events, for example of charged analytes such as proteins and due to structural changes in the negatively charged aptamer backbone upon analyte binding.

Analyte binding can be observed in real time by monitoring I_{DS} at a fixed gate potential during analyte addition[38,39,52] or I_DV_G curves can be recorded after analyte addition.[36,53–55] Measuring I_{DS} in real time during analyte addition was not reliable (see Fig. S5, ESI†). We suspect that when a constant gate voltage is applied during analyte binding, a subset of the

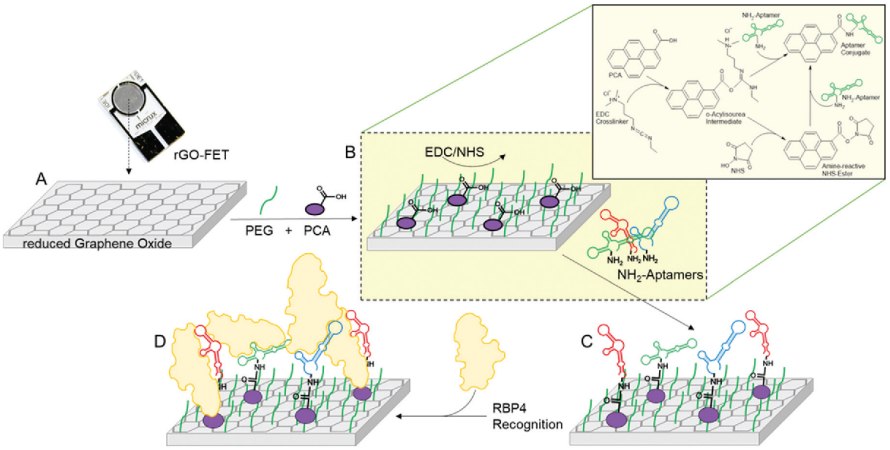

Scheme 4 Functionalization of rGO-FETs with polyclonal ssDNA aptamer libraries and specific apo- or holo-RBP4 detection. (A) The rGO-FET were immersed into a mixture of PyPEG (PEG pre-conjugated with a PBSE) (500 μM) and 1-pyrenecarboxylic acid (PCA, 50 μM, linker) in DMSO for 12 h at room temperature to obtain a 10 : 1 ratio of blocking and linking agents on the biosensor's surface. (B and C) Apo- or holo-RBP4 aptamer library immobilization by first activating the carboxyl groups by immersion into a solution of EDC (15 mM)/NHS (15 mM) in 150 mM PBS solution for 30 min, followed by covalent coupling of the 5′-NH_2-modified aptamer (100 nM in milliQ grade water for 40 min at 25 °C). (D) Specific affinity recognition of either apo- or holo-RBP4 by the on rGO-FET immobilized polyclonal ssDNA aptamer libraries in electrical measurements.

aptamer library might be misfolded and lose some or all affinity for RBP_4. Instead, we recorded full I_DV_G curves after incubation of the chip with each analyte concentration, which allowed excellent reproducibility between devices. As the time required for either sensing method is relatively similar, I_DV_G – based sensing is acceptable for diagnostic purposes.

An I_DV_G-shift can occur both in the Dirac point (the potential at which I_{DS} is at its minimum) and the slope of the curves, with specific interactions causing a significantly more pronounced change than non-specific interactions. I_DV_G curves were recorded first in 1× PBS solution as a background and after the addition of each analyte concentration (3–300 nM) with both target and non-target analyte (either apo- or holo-RBP4).

Fig. 3 shows typical device responses to specific and non-specific binding events. Additional data can be found in the ESI.†

Slight changes in the shape and slope of the I_DV_G curve occurred after adding the non-target analyte (see Fig. 4), but there was no Dirac point shift. This change can be attributed to non-specific binding events of the analyte to the aptamers or PEG groups on the surface. Addition of the target analyte resulted in a more pronounced shift in the I_DV_G curve, with changes in both the slope and the Dirac point, indicating of stronger, specific binding events.

The most pronounced shifts in I_DV_G curves upon analyte binding occurred around −0.4 V (see Fig. 3). To quantify sensor response, I_{DS} shifts at this potential upon analyte addition were used to compare the signal change for specific and non-specific binding events. Fig. 4 shows the device response to specific and non-specific analyte binding. Both for the apo- and holo- aptamer libraries, addition of the target analyte produced a significantly stronger I_{DS} – shift than the non-target analyte.

As the total concentration of RBP4 in human serum is approximately 1–3 μM (estimates vary depending on the method used to quantify RBP4 levels),[17,56] we tested RBP4 concentrations from 0.3–300 nM to determine device performance. At all concentrations, the specific response was significantly stronger than the nonspecific signal. A small signal could also be seen upon addition of 100 pM RBP4 (see Fig. S5, ESI†), indicating a theoretical detection limit of 2 ng mL^{-1} RBP4, which is three orders of magnitude more sensitive than a previously reported aptamer-based RBP4 sensing method.[57]

As the sample matrix for RBP4 detection would be human blood plasma (HBP), we used blood plasma to test sensor passivation. Due to the high viscosity of undiluted HBP, it was impractical to test the sensor in this environment, and device response was only tested in 10% HBP or less. There was a change in device response in the presence of 10% and 1% HBP, however, rinsing with buffer returned the signal to the baseline. This could be observed both with an rGO-FET device and in a surface plasmon resonance experiment (see Fig. S6, ESI†). Thus, there was no unspecific binding potentially interfering with RBP4 detection. To determine if the presence of HBP interfered with RBP4 detection, we added 1% HBP spiked with RBP4. After rinsing, the signal did not return to baseline, indicating that while HBP was removed, RBP4 remained on the surface.

Diluting the patient sample to 10% would also reduce the concentration of RBP4 tenfold from 3 μM to 300 nM. This is well within the sensitivity range of our device, which would

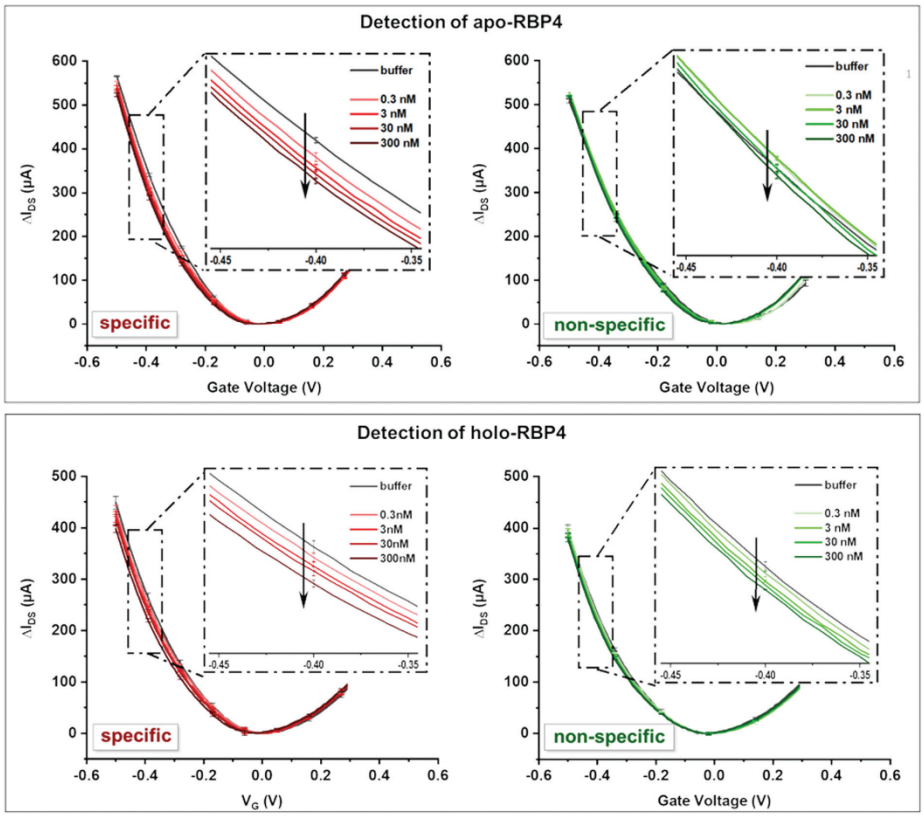

Fig. 3 Top: Detection of apo-RBP4. Bottom: Detection of holo-RBP4. I_DV_G curves are an average of a minimum of 3 individual curves with error bars showing the standard deviation. Both devices showed significantly more pronounced shifts in their I_DV_G characteristics upon specific analyte binding.

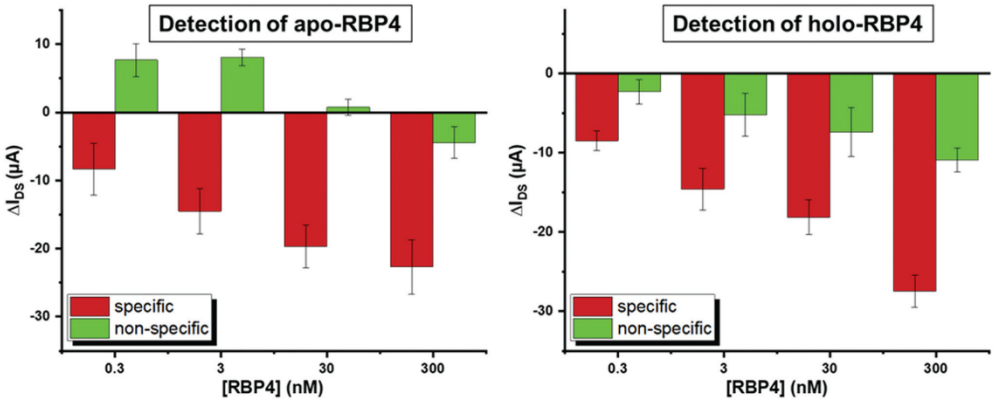

Fig. 4 Average difference in current at −0.4 V upon addition of increasing concentrations of RBP4. Δ-Values shown are averages of a minimum of three independent experiments on different devices. Error bars show the standard deviation.

allow a dilution by a factor of up to 10 000. Using the device in a clinical setting, a 100-fold dilution of a healthy patient sample should produce a pronounced signal with the holo-RBP4 aptamer library and little to no response in the device functionalized with the apo-library. Pathological states with increased apo-RBP4 levels should produce a decreased response in the former and an increased response in the latter. Future studies will further optimize device performance in blood and with real patient samples.

Conclusion

The evolution of focused polyclonal aptamer libraries instead of single aptamers against target molecules serves as a promising strategy in diagnostics and sensor technology. Larger sequence spaces enable a distinct and specialized diversity of binding aptamers. Multiple target recognition can be achieved generating enhanced versatility and thus increased performance in sensing and quantification of target molecules. Moreover, the great biotechnological availability of polyclonal aptamer libraries contributes to the rapid, cost-effective and easy development of novel, highly specific electronic sensors for use as powerful tools in clinical diagnostics. By functionalizing the channel of an rGO-FET device, we were able to selectively discriminate between RBP4 isoforms at physiologically relevant concentrations between 0.3 and 30 nM. We believe that these results may open a route to develop biosensors for the fast and reliable measurement of the RBP4 isoform concentrations as a novel diagnostic marker.

Conflicts of interest

There are no conflicts to declare.

References

1 E. Esteve, W. Ricart and J. M. Fernández-Real, *Diabetes Care*, 2009, **32**, S362–S367.
2 M. E. Newcomer and D. E. Ong, *Biochim. Biophys. Acta, Protein Struct. Mol. Enzymol.*, 2000, **1482**, 57–64.
3 S. J. Thompson, A. Sargsyan, S. A. Lee, J. J. Yuen, J. Cai, R. Smalling, N. Ghyselinck, M. Mark, W. S. Blaner and T. E. Graham, *Diabetes*, 2017, **66**, 58–63.
4 W. S. Blaner, *Endocr. Rev.*, 1989, **10**, 308–316.
5 C. H. Chen, T. J. Hsieh, K. Der Lin, H. Y. Lin, M. Y. Lee, W. W. Hung, P. J. Hsiao and S. J. Shin, *J. Biol. Chem.*, 2012, **287**, 9694–9707.
6 M. Kanai, A. Raz and D. S. Goodman, *J. Clin. Invest.*, 1968, **47**, 2025–2044.
7 L. Quadro, L. Hamberger, V. Colantuoni, M. E. Gottesman and W. S. Blaner, *Mol. Aspects Med.*, 2003, **24**, 421–430.
8 J. Raila, T. E. Willnow and F. J. Schweigert, *J. Nutr.*, 2005, **135**, 2512–2516.
9 K. Kelly, S. Kashyap, V. O'Leary, J. Major, P. Schauer and J. Kirwan, *Obesity*, 2009, **18**, 663–666.
10 C.-H. Chu, H.-C. Lam, J.-K. Lee, C.-C. Lu, C.-C. Sun, H.-J. Cheng, M.-C. Wang and M.-J. Chuang, *Endocr. J.*, 2011, **58**, 841–847.
11 Q. Yang, T. E. Graham, N. Mody, F. Preitner, O. D. Peroni, J. M. Zabolotny, K. Kotani, L. Quadro and B. B. Kahn, *Nature*, 2005, **436**, 356–362.
12 T. E. Graham, Q. Yang, M. Blüher, A. Hammarstedt, T. P. Ciaraldi, R. R. Henry, C. J. Wason, A. Oberbach, P.-A. Jansson, U. Smith and B. B. Kahn, *N. Engl. J. Med.*, 2006, **354**, 2552–2563.
13 S. K. Frey, B. Nagl, A. Henze, J. Raila, B. Schlosser, T. Berg, M. Tepel, W. Zidek, M. O. Weickert, A. F.-H. Pfeiffer and F. J. Schweigert, *Lipids Health Dis.*, 2008, **7**, 29.
14 H. Xu, G. T. Barnes, Q. Yang, G. Tan, D. Yang, C. J. Chou, J. Sole, A. Nichols, J. S. Ross, L. A. Tartaglia and H. Chen, *J. Clin. Invest.*, 2003, **112**, 1821–1830.
15 J. M. Olefsky and C. K. Glass, *Annu. Rev. Physiol.*, 2010, **72**, 219–246.
16 C. Erikstrup, O. H. Mortensen, A. R. Nielsen, C. P. Fischer, P. Plomgaard, A. M. Petersen, R. Krogh-Madsen, B. Lindegaard, J. G. Erhardt, H. Ullum, C. S. Benn and B. K. Pedersen, *Diabetes, Obes. Metab.*, 2009, **11**, 204–212.
17 T. E. Graham, C. J. Wason, M. Blüher and B. B. Kahn, *Diabetologia*, 2007, **50**, 814–823.
18 A. D. Ellington and J. W. Szostak, *Nature*, 1990, **346**, 818–822.
19 T. K. Sharma, J. G. Bruno and A. Dhiman, *Biotechnol. Adv.*, 2017, **35**, 275–301.
20 C. Tuerk and L. Gold, *Science*, 1990, **249**, 505–510.
21 P. Bayat, R. Nosrati, M. Alibolandi, H. Rafatpanah, K. Abnous, M. Khedri and M. Ramezani, *Biochimie*, 2018, **154**, 132–155.
22 D. Kubiczek, N. Bodenberger and F. Rosenau, *Antimicrobial Research: Novel bioknowledge and educational programs*, 2017, vol. 6, pp. 368–378.
23 D. Kubiczek, H. Raber, N. Bodenberger, T. Oswald, M. Sahan, D. Mayer, S. Wiese, S. Stenger, T. Weil and F. Rosenau, *Chem. – Eur. J.*, 2020, **26**, 14536–14545.
24 H. Qu, A. T. Csordas, J. Wang, S. S. Oh, M. S. Eisenstein and H. T. Soh, *ACS Nano*, 2016, **10**, 7558–7565.
25 S. S. Sekhon, P. Kaur, Y. H. Kim and S. S. Sekhon, *npj 2D Mater. Appl.*, 2021, **5**, 21.
26 A. Minopoli, B. Della Ventura, B. Lenyk, F. Gentile, J. A. Tanner, A. Offenhäusser, D. Mayer and R. Velotta, *Nat. Commun.*, 2020, **11**, 6134.
27 J. Zhang, L. P. Smaga, N. S.-R. Satyavolu, J. Chan and Y. Lu, *J. Am. Chem. Soc.*, 2017, **139**, 17225–17228.
28 T. Liang, Z. Yao, J. Ding, Q. Min, L. Jiang and J. J. Zhu, *ACS Appl. Mater. Interfaces*, 2018, **10**, 34050–34059.
29 J. Zhou and J. Rossi, *Nat. Rev. Drug Discovery*, 2017, **16**, 181–202.
30 G. Mahlknecht, R. Maron, M. Mancini, B. Schechter, M. Sela and Y. Yarden, *Proc. Natl. Acad. Sci. U. S. A.*, 2013, **110**, 8170–8175.
31 P. Aspermair, V. Mishyn, J. Bintinger, H. Happy, K. Bagga, P. Subramanian, W. Knoll, R. Boukherroub and S. Szunerits, *Anal. Bioanal. Chem.*, 2020, 7–11.
32 Y. Chen, R. Ren, H. Pu, X. Guo, J. Chang, G. Zhou, S. Mao, M. Kron and J. Chen, *Sci. Rep.*, 2017, **7**, 10974.

33 S. Afsahi, M. B. Lerner, J. M. Goldstein, J. Lee, X. Tang, D. A. Bagarozzi, D. Pan, L. Locascio, A. Walker, F. Barron and B. R. Goldsmith, *Biosens. Bioelectron.*, 2018, **100**, 85–88.
34 G. Seo, G. Lee, M. J. Kim, S.-H. Baek, M. Choi, K. B. Ku, C.-S. Lee, S. Jun, D. Park, H. G. Kim, S.-J. Kim, J.-O. Lee, B. T. Kim, E. C. Park and S. Il Kim, *ACS Nano*, 2020, **14**, 5135–5142.
35 R. Stoltenburg, C. Reinemann and B. Strehlitz, *Anal. Bioanal. Chem.*, 2005, **383**, 83–91.
36 B. Cai, L. Huang, H. Zhang, Z. Sun, Z. Zhang and G.-J. Zhang, *Biosens. Bioelectron.*, 2015, **74**, 329–334.
37 S. Xu, S. Jiang, C. Zhang, W. Yue, Y. Zou, G. Wang, H. Liu, X. Zhang, M. Li, Z. Zhu and J. Wang, *Appl. Surf. Sci.*, 2018, **427**, 1114–1119.
38 Y.-M. Lei, M.-M. Xiao, Y.-T. Li, L. Xu, H. Zhang, Z.-Y. Zhang and G.-J. Zhang, *Biosens. Bioelectron.*, 2017, **91**, 1–7.
39 L. Zhou, H. Mao, C. Wu, L. Tang, Z. Wu, H. Sun, H. Zhang, H. Zhou, C. Jia, Q. Jin, X. Chen and J. Zhao, *Biosens. Bioelectron.*, 2017, **87**, 701–707.
40 S. Wang, M. Z. Hossain, K. Shinozuka, N. Shimizu, S. Kitada, T. Suzuki, R. Ichige, A. Kuwana and H. Kobayashi, *Biosens. Bioelectron.*, 2020, **165**, 112363.
41 T. Ono, Y. Kanai, K. Inoue, Y. Watanabe, S. Nakakita, T. Kawahara, Y. Suzuki and K. Matsumoto, *Nano Lett.*, 2019, **19**, 4004–4009.
42 C. Reiner-Rozman, M. Larisika, C. Nowak and W. Knoll, *Biosens. Bioelectron.*, 2015, **70**, 21–27.
43 P. Aspermair, U. Ramach, C. Reiner-Rozman, S. Fossati, B. Lechner, S. E. Moya, O. Azzaroni, J. Dostalek, S. Szunerits, W. Knoll and J. Bintinger, *J. Am. Chem. Soc.*, 2020, **142**, 11709–11716.
44 T. T.-Y. Wang, K. C. Lewis and J. M. Phang, *Gene*, 1993, **133**, 291–294.
45 A. Singh, V. Upadhyay, A. K. Upadhyay, S. M. Singh and A. K. Panda, *Microb. Cell Fact.*, 2015, **14**, 41.
46 A. Mitraki, B. Fane, C. Haase-Pettingell, J. Sturtevant and J. King, *Science*, 1991, **253**, 54–58.
47 D. Shortle and M. S. Ackerman, *Science*, 2001, **293**, 487–489.
48 Y. Xie, H. A. Lashuel, G. J. Miroy, S. Dikler and J. W. Kelly, *Protein Expr. Purif.*, 1998, **14**, 31–37.
49 M. S. Levin, B. Locke, N. C. Yang, E. Li and J. I. Gordon, *J. Biol. Chem.*, 1988, **263**, 17715–17723.
50 C. Reiner-Rozman, R. Hasler, J. Andersson, T. Rodrigues, A. Bozdogan, J. Bintinger and P. Aspermair, *Micro Nano Lett.*, 2021, **16**(8), 436–442.
51 C. Zhao, K. M. Cheung, I. W. Huang, H. Yang, N. Nakatsuka, W. Liu, Y. Cao, T. Man, P. S. Weiss, H. G. Monbouquette and A. M. Andrews, *Sci. Adv.*, 2021, **7**, 25–27.
52 B. Thakur, G. Zhou, J. Chang, H. Pu, B. Jin, X. Sui, X. Yuan, C.-H. Yang, M. Magruder and J. Chen, *Biosens. Bioelectron.*, 2018, **110**, 16–22.
53 N. Nakatsuka, K.-A. Yang, J. M. Abendroth, K. M. Cheung, X. Xu, H. Yang, C. Zhao, B. Zhu, Y. S. Rim, Y. Yang, P. S. Weiss, M. N. Stojanović and A. M. Andrews, *Science*, 2018, **362**, 319–324.
54 S. M. Majd, A. Salimi and F. Ghasemi, *Biosens. Bioelectron.*, 2018, **105**, 6–13.
55 T.-Y. Chen, P. T.-K. Loan, C.-L. Hsu, Y.-H. Lee, J. Tse-Wei Wang, K.-H. Wei, C.-T. Lin and L.-J. Li, *Biosens. Bioelectron.*, 2013, **41**, 103–109.
56 J. M. Fernández-Real, J. M. Moreno and W. Ricart, *Diabetes*, 2008, **57**, 1918–1925.
57 J. L. Su, B. S. Youn, W. P. Ji, J. H. Niazi, S. K. Yeon and B. G. Man, *Anal. Chem.*, 2008, **80**, 2867–2873.

Electronic Supplementary Material (ESI) for Nanoscale Horizons.

Supporting Information

Polyclonal aptamer libraries as binding entities on a graphene FET based biosensor for the discrimination of apo- and holo- retinol binding protein 4

Ann-Kathrin Kissmann‡[a], Jakob Andersson‡*[b], Anil Bozdogan‡[c], Valerie Amann[a], Markus Krämer[a], Hu Xing[a], Heinz Fabian Raber[a], Dennis H. Kubiczek[a], Patrik Aspermair[b], Wolfgang Knoll[b] and Frank Rosenau*[a][d]

Abstract: Oligonucleotide DNA aptamers represent an emergently important class of binding entities towards as different analytes as small molecules or even whole cells. Without the canonical isolation of individual aptamers following the SELEX process already the focused polyclonal libraries prepared by this *in vitro* evolution and selection can directly be used to label their dedicated analytes and to serve as binding molecules on surfaces. Here we report the first instance of a sensor able to discriminate between loaded and unloaded retinol binding protein 4 (RBP4), an important biomarker for the prediction of diabetes and kidney disease. The sensor relies purely on two aptamer libraries tuned such that they discriminate between the protein isoforms, requiring no further sample labelling to detect RBP4 in both states. The evolution, binding properties of the libraries and the functionalization of graphene FET sensor chips are presented as well as the functionality of the resulting biosensor.

Table of Contents

Experimental Procedures

Materials.

Acetic acid, agarose, ampicillin, boric acid, bromophenol blue, $CaCl_2$, isobutanol, K_2HPO_4, KCl, KOH, KH_2PO_4, LB medium, HCl, NaCl, Span® 80, Tris, triton X-100, tween® 80 and urea were ordered from Roth (Carl Roth GmbH and Co. KG, Karlsruhe, Germany). All*trans*-retinal, bovine serum albumin, coomassie brillant blue G-250, ethanol, N-hydroxysuccinimide, sodiumdodecyl sulfate (SDS) and tRNA were purchased from Sigma Aldrich (St. Louis, Missouri, USA). EDTA, Dulbecco's Phosphate-Buffered Saline (1x), Dynabeads® M 280 tosyl-activated were obtained from Thermo Fisher Scientific (Waltham, Massachusetts, USA). BioMag® Streptavidin was ordered from QIAGEN (Venlo, Netherlands) and human serum was obtained from Merck KgaA (Darmstadt, Germany) (Product Number H4522-20ML),

Recombinant RBP4 production in *E. coli* and purification from inclusion bodies.

Chemical competent *E. coli* BL21 (DE3) Tuner™ (200 µL) (Merck Millipore, Darmstadt, Germany) were transformed using 1 µL pET22b-rRBP4 (191 ng/µL). The RBP4 gene was gained from pET302-rBBP4 (Thermo Fisher Scientific, Darmstadt, Germany) and it was cloned into a pET22b vector, previously. Cells were incubated at 4 °C for 45 min, followed by heat shock treatment for 90 sec at 42 °C and subsequent incubation for 2 min at 4 °C. Then, 800 µL pre-warmed lysogeny broth (LB) medium was added and incubated at 37 °C for 1 h to regenerate the cells. After regeneration cells were plated on selective LB-amp (100 µg/mL) agar plates and incubated overnight at 37 °C. To produce RBP4, one clone of freshly transformed *E. coli* BL21 (DE3) was used to inoculate 25 mL selective LB-amp (100 µg/mL) medium containing 0.4 % glucose and cultivated overnight at 37 °C and 150 rpm. Expression cultures were inoculated with an optical density (OD) of 0.1 at 600 nm in 250 mL LB medium (0.4 % glucose, 100 µg/mL ampicillin) in 1 L Erlenmeyer flasks without chicanes. Induction of cultures was performed using 1 mM isopropyl-β-D-thiogalactoside (IPTG) after growth to an OD_{600} of 0.6 and as control, a non-induced culture was cultivated similarly. After induction, the expression cultures were further cultivated for 1 h at 37 °C, followed by a temperature shift to 30 °C for 4 h. After cultivation, the cells were harvested by transferring them to 50 mL tubes followed by centrifugation (4000 xg, 20 min, 4 °C). Then, the supernatants were discarded and the cell pellets were washed with 5 mL 1x PBS, combined, and centrifuged (4000 xg, 20 min, 4 °C). Afterwards, supernatants were discarded, and the cell pellets were frozen at -80 °C overnight. SDS-polyacrylamide gel electrophoresis was performed to verify the production process.[1]

Frozen cell pellets were thawed on ice, suspended in 15 mL lysis buffer (50 mM Tris, 2 mM EDTA, 0.1 % Triton X-100, pH 7.5) and sonicated on ice for 12 min in 6 cycles at 40 % intensity. The *E. coli* lysate was then centrifuged (14 000 xg, 45 min, 4 °C) and the pellets containing the insoluble inclusion bodies were dissolved in 15 mL denaturation buffer (50 mM Tris-HCl, pH 8, 2 mM EDTA, 0.1 % (v/v) Triton X-100, 8 M Urea). The protein solution was centrifuged (13 000 rpm, 30 min, 4 °C) and the collected supernatant was diluted 1:14 with renaturation buffer (50 mM Tris-HCl, pH 8, 5 mM EDTA, 1 % (v/v) Triton X-100, 0.8 M Urea) and incubated at 4 °C overnight. Afterwards, the protein solution was concentrated using Vivaspin 20 centrifugal concentrators (molecular weight

cut-off 10 kDa) (Sartorius, Göttingen, Germany) at 4000 xg in 1 h intervals at 4 °C, buffer exchange was performed by washing three times with 20 mL 1x PBS.

Purification of *E. coli*-derived recombinant RBP4 isolated from inclusion bodies[2] was performed by size-exclusion chromatography using the NGC™ chromatography system (Bio-Rad Laboratories, Inc., Hercules, California, USA) with ChromLab Software and SuperdexTM 200 Increase 10/300 GL (GE Healthcare Bio-Sciences AB, Danderyd, Sweden). First, the column and the chromatography system were rinsed with 36 mL (1.5 column volumes) filtered dH_2O at a flow rate of 0.5 mL/min and then equilibrated with 36 mL filtered 1x PBS using a flow rate of 0.75 mL/min, a 1 mL loop was rinsed with 3 mL 1x PBS prior to sample injection. After the sample was applied, UV detection was performed at 280 nm and fractionation was started after a retention volume of ~7.5 mL, 200 µL fractions were collected stepwise in a 96-well-microplate. Afterwards, the system and column were rinsed with 36 mL filtered dH_2O using a flow rate of 0.75 mL/min and then with 36 mL 20% ethanol at a flow rate of 0.5 mL/min. Fractions of purified RBP4 were analyzed by SDS PAGE and stored at -20 °C. Concentrations were calculated by the ChromLab Software for fractions obtained from SEC.

All-*trans*-retinal binding properties of apo-RBP4.

Quenching of intrinsic protein fluorescence was analyzed to determine RBP4 activity by adding increasing all-*trans*-retinal amounts. Working solutions were prepared by diluting retinal and apo-RBP4 in DPBS. After the addition of increasing amounts of retinal (0 - 2.125 µM) to a constant apo-RBP4 amount of 0.425 µM, the mixture was incubated at 25 °C for 90 min under exclusion of light in a Lumox® multiwell 384 well-plate. Then, the fluorescence emission was measured using a Spark® multimode microplate reader, the emission was monitored at 340 nm with an excitation wavelength of 280 nm.

***In vitro* selection of aptamer libraries against apo- and holo-RBP4.**

The selection of aptamer libraries was based on the FluMag-SELEX procedure using tosyl-activated magnetic Dynabeads M-280.[3] Immobilization of proteins was performed by covalent coupling of the p-toluenesulphonyl (tosyl) groups on the surface of the magnetic beads with primary amino groups of RBP4. The magnetic beads were coated as described by the manufacturer and aliquoted into 200 µL aliquots containing 0.68 mg beads, respectively. To gain holo-RBP4-coated beads, beads coated with apo-RBP4 were incubated with 3x excess all-*trans*-retinal for 90 min at 25 °C with the exclusion of light on a rotator. Thereafter, the beads were washed twice with 1 mL 1x DPBS, pH 7.4, containing 0.1 % (w/v) BSA, resuspended, and aliquoted into 200 µL samples (0.68 mg beads per aliquot) and stored at 4 °C. In counter selection steps naked beads were used which were treated similarly prior to usage.

The commercial library (TriLink BioTechnologies, Inc, San Diego, California, USA) with approximately $6x10^{14}$ individual aptamers contained a central random 40-nucleotide (nt) region flanked on both sides by 23 nt primer binding sites. The selection of aptamers was carried out using primers with the following sequences: Cyanine 5-labeled forward primer (Cy5 FW): 5'-[Cy 5]T AGG GAA GAG AAG GAC ATA TGA T-3' and biotin-labelled reverse primer (Bio RW): 5'-[BI O]T CAA GTG GTC ATG TAC TAG TCA A-3' (Eurofins Genomics, Ebersberg, Germany). Prior to each SELEX round, coated magnetic beads were washed three times with 500 µL binding buffer (100 mM NaCl, 20 mM Tris-HCl, 2 mM $MgCl_2$, 5 mM KCl, 1 mM $CaCl_2$, 0.02 % (v/v) Tween 20, pH 7.6). For aptamer activation, the ssDNA library was heated to 90 °C for 10 min, immediately cooled, and kept at 4 °C for 15 min, followed by incubation at 25 °C for 7 min. Counter selections against naked beads were performed prior to selection rounds 1 – 6 and twofold counter selections were conducted prior to selection rounds 7 and 8. In the first selection round, naked beads were suspended in 500 µL DPBS containing 1 nmol of random ssDNA library and incubated at 25 °C for 30 min under rotation in the dark. Afterwards, the supernatant containing unbound aptamers was mixed with 600 pmol BSA (100 mg/mL) and 600 pmol tRNA (10 mg/mL), transferred to either washed apo-RBP4-coated beads or holo-RBP4-coated beads and incubated again. Unbound aptamers were removed by washing with 500 µL binding buffer and elution of bound aptamers from apo- or holo-RBP4-coated magnetic beads was performed by incubating the beads in 200 µL DPBS at 95 °C for 5 min, followed by magnetic separation for 2 min. After elution 40 µL of the aptamer solutions were analyzed by monitoring the fluorescence intensity using a Tecan infinite F200 Microplate Reader (Tecan Group AG, Männedorf, Suisse) at an excitation wavelength of 635 nm and an emission wavelength of 670 nm. After each SELEX round, the eluted ssDNA aptamers were amplified by emulsion polymerase chain reaction (ePCR).[4] Therefore, 200 µL aqueous phase (40 µL 5x Herculase II reaction buffer, 5 µL dNTPs (10 mM, 2.5 mM each), 0.5 µL Cy5 FW and 0.5 µL Bio RW, 1 µL Herculase II Fusion DNA Polymerase (Agilent Technologies, Santa Clara, California, USA), 20 µL BSA (100 mg/mL), 113 µL Water HPLC Plus and 20 µL ssDNA aptamers) were mixed with 400 µL of the oil-surfactant mixture (4.5 % (vol/vol) Span® 80, 0.4 % (vol/vol) Tween® 80, 0.05 % (vol/vol) Triton X-100, 95.05 % (vol/vol) mineral oil) and incubated for 10 min on a vortexer.

Afterwards, the emulsion was transferred into PCR reaction tubes as aliquots of 50 µL and then overlaid with 50 µL mineral oil. The amplification conditions were 2 min at 80 °C, 2 min at 85 °C, 2 min at 90 °C, 3 min at 94 °C and 25 cycles of 30 sec at 94 °, 30 sec at 49.1 °C, 30 sec at 72 °C, then 2 min at 72 °C after the last cycle. After ePCR run, the emulsified PCR reactions were pooled in a microcentrifuge tube (2 mL), mixed with 1 mL isobutanol, centrifuged at 13 000 rpm for 1 min at 25 °C, and then the upper phase was discarded. Afterwards, the PCR products were cleaned using the QIAquick PCR Purification Kit (QIAGEN, Venlo, Netherlands) and analyzed on a 2 % agarose gel by agarose gel electrophoresis. In order to separate the relevant DNA strands from the double-stranded PCR products, streptavidin-coated magnetic beads were used in alkaline strand separation. Therefore, 50 µL streptavidin beads were washed three times with 1 mL DPBS by magnetic separation, resuspended in the PCR product, and then incubated for 16 h at 25 °C under rotation without light exposure. Afterwards, unbound DNA was separated and removed, and the streptavidin beads were washed with 1 mL DPBS. Then, 50 µL NaOH (100 mM, pH 13) was added, incubated for 4 min in total and after 2 min the microcentrifuge tubes were placed in a magnetic separator. In the next step, 45 µL of the NaOH solution were added to 126 µL DPBS in a new microcentrifuge tube, followed by subsequent addition of 34.4 µL 100 mM NaH_2PO_4. The remaining 5 µL of NaOH solution were analyzed on a 2% agarose gel to monitor successful separation and the correct size of the ssDNA fragments, and the concentration of the ssDNA was measured using a NanoPhotometer (IMPLEN, Munich, Germany). After the first selection round, 30 pmol ssDNA from the previous round was used in the SELEX rounds 2 – 6, 10 pmol ssDNA was used in rounds 7 and 8. All rounds started with binding to naked magnetic beads with increasing incubation times, followed by selection with increasing amounts of tRNA and BSA and washing steps with binding buffer. In selection round 6 a reciprocal washing step containing RBP4 was performed in addition. There, apo-RBP4 coated beads were washed with 13.6 µg holo-RBP4 diluted in binding buffer, and the holo-RBP4 magnetic beads were washed with 13.6 µg apo-RBP4 bevor elution.

Specificity analysis of RBP4 aptamer libraries.

The enrichment of specific ssDNA aptamers over the FluMag-SELEX process was verified in a binding assay. Therefore, the aptamer libraries from each round were bound to either apo- or holo RBP4-coated magnetic beads, incubated and quantified by fluorescence measurement afterwards. In the first step, 10 pmol of each aptamer library were activated as described earlier and then the libraries against apo-RBP4 were incubated for 30 min at 25 °C with apo-RBP4-coated magnetic beads and the holo-RBP4 libraries with holo-RBP4-coated beads. The supernatants were separated by magnetic separation, the beads were washed with 500 µL binding buffer and resuspended in 200 µL DPBS. After elution (95 °C, 5 min), 40 µL of the aptamer solutions were analyzed by measuring the fluorescence emission using a Tecan infinite F200 microplate reader, the emission was monitored at 670 nm with an excitation wavelength of 635 nm. In addition, the selectivity of the aptamer libraries was analyzed in a characterization assay. Similar to the binding assay, 10 pmol of activated aptamer libraries were used and incubated for 30 min at 25 °C with apo- and holo-RBP4-coated magnetic beads as well as with naked magnetic beads. Then, the supernatants were separated by magnetic separation and the beads were washed with 500 µL binding buffer and resuspended in 200 µL DPBS. After elution (95 °C, 5 min), 40 µL of the aptamer solutions were analyzed by monitoring the fluorescence emission at 670 nm using a Tecan infinite F200 microplate reader with an excitation wavelength of 635 nm. Experiments were conducted in triplicates.

Fluorescence microscopy.

In order to visualize the specific target binding of both final aptamer libraries they were submitted to fluorescence microscopic analysis. Therefore, 30 pmol of each aptamer library were activated as described earlier and then the libraries were incubated for 30 min at 25 °C with apo- and holo-RBP4-coated magnetic beads as well as with naked beads. Afterwards, 100 µL of each reaction mixture were transferred to a 96-well microplate and fluorescence microscopy was performed using a Leica DMi8 coded (Leica Microsystems CMS GmbH, Wetzlar, Germany) at x40 magnitude under transmitted light and using the Y5 filter (excitation: 590-650 nm and emission: 662-738 nm) for fluorescence imaging.

Immobilization of aptamer libraries on rGO-FETs.

Prior to aptamer immobilization on the rGO-FETs a PCR, was performed to introduce an amine at the 5'-end of the relevant strands. Therefore, a special amino forward primer (Amino-FW) was used: 5'-[AC 6]T AGG GAA GAG AAG GAC ATA TGA T-3' (Eurofins Genomics, Ebersberg, Germany). The rGO-FETs (fabrication method as reported previously[5]) were immersed into a 2.5 mL mixture of 500 µM PyPEG (blocking agent polyethylene glycol was pre-conjugated with PBSE linker) containing 50 µM 1-pyrenecarboxylic acid (PCA) in DMSO and incubated for 12 h at 25 °C. Afterwards, they were rinsed thoroughly with DMSO and then with dH_2O. In the following step, the carboxyl groups were activated by immersion of the rGO-FETs into a solution of 15 mM EDC/15 mM NHS in

0.1 M PBS (pH 7.4) for 30 min at 25 °C, followed by covalent coupling of the 5′-NH_2-modified apo- or holo-RBP4 aptamer libraries (15 µL, 100 nM in DNase-free water) by incubation for 40 min at 25 °C and subsequent washing with PBS for three times.

Results and Discussion

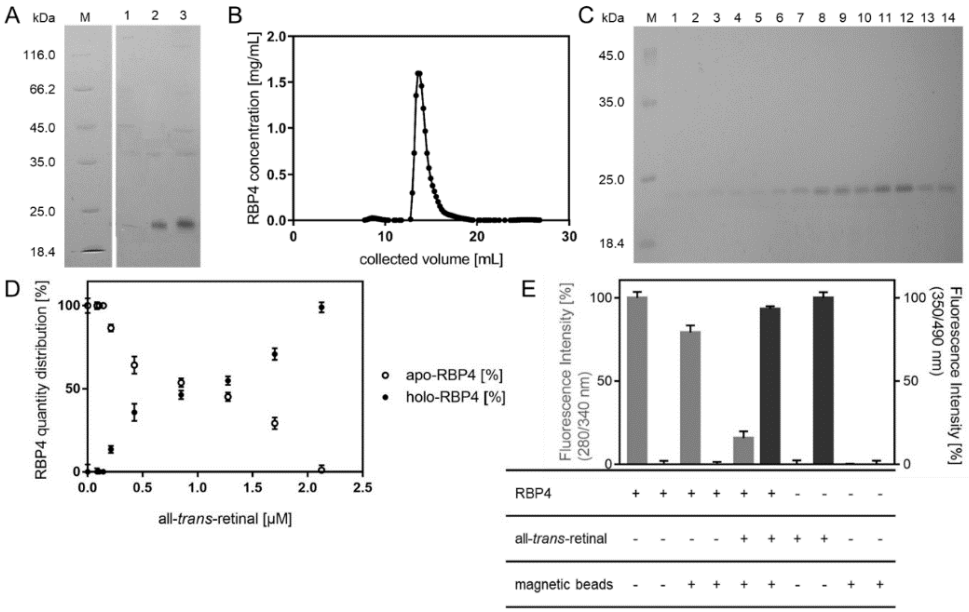

Supplementary Figure S1. Expression, purification and characterization of *E. coli* BL21 (DE3)-derived RBP4. A) SDS-PAGE analysis of renaturation of *E. coli* BL21 (DE3)-produced RBP4. Separation through a polyacrylamide gel containing 0.1 % SDS, the gel was stained using Coomassie Brillant Blue G-250. Lane M, Pierce™ unstained protein molecular weight marker; lane 1, harvested cell lysate supernatant; lane 2, insoluble protein fraction after addition of 8 M urea; lane 3, harvested RBP4 from inclusion bodies after renaturation through incubation with buffer containing 0.8 M urea in excess. B) Concentration determination of purified RBP4. Concentrations were calculated by the ChromLab Software for fractions obtained from size exclusion chromatography using a NGC™ Chromatography System (Bio-Rad Laboratories, Inc., Hercules, California, USA) and Superdex 200 Increase 10/300 GL (GE Healthcare, Chicago, Illinois, USA) with the extinction coefficient 77400 M^{-1} cm^{-1} and the molecular weight of 21 kDa for RBP4. C) Fractions obtained from size exclusion chromatography were analyzed by electrophoresis through a polyacrylamide gel containing 0.1 % SDS. Lane M, Pierce™ unstained protein molecular weight marker; lanes 1-14, Superdex 200 Increase 10/300 GL fractions containing purified apo-RBP4. The gel was stained with Coomassie Brillant Blue G-250. D) Binding of all-*trans*-retinal to *E. coli*-derived apo-RBP4 and formation of holo-RBP4. After addition of increasing amounts of all-*trans*-retinal to apo-RBP4, the fluorescence emission was measured using a Spark® multimode microplate reader (Tecan Trading AG, Männedorf, Switzerland). Emission was monitored at 340 nm with an excitation wavelength of 280 nm. The amount of *E. coli*-derived apo-RBP4 was kept constant at 0.425 µM, while the all-*trans*-retinal concentration was varied between 0 and 2.125 µM. Error bars symbolize standard deviations of measurements conducted in triplicates. E) Verification of coating of Dynabeads M-280 tosyl-activated with apo-RBP4 and holo-RBP4. Left y-axis: Intrinsic protein fluorescence measurement. Signals of single apo-RBP4, apo-RBP4 and holo-RBP4 coated beads (grey bars). Quenching of holo-RBP4 fluorescence after complexation of apo-RBP4 with all-trans-retinal. Emission was monitored at 340 nm with an excitation wavelength of 280 nm. Error bars symbolize standard deviations of measurements conducted in triplicates. Right y-axis: Fluorescence measurement of all-*trans*-retinal, signals of retinal and holo-RBP4 coated beads (black bars). Emission was monitored at 490 nm with an excitation wavelength of **350** nm. Error bars symbolize standard deviations of measurements conducted in triplicates.

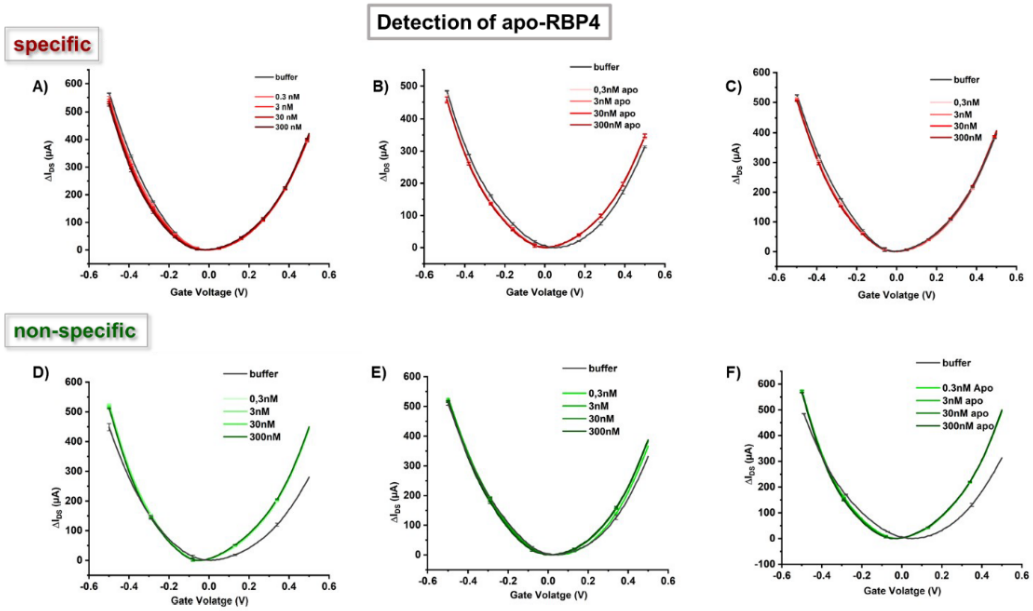

Supplementary Figure S2. I_DV_G characterization of sensing devices obtained by sweeping the gate voltage from -0.5V to 0.5V. A, B and C show 3 specific interactions between apo-RBP4 and the corresponding aptamer library immobilized on the channel. D, E and F show the holo-RBP4 interaction with the same aptamer library that should have no affinity for holo-RBP4. Conditions and parameters were identical in each experiment. Each individual curve is an average of three measurements. Error bars indicate the standard deviation. Incubation time for each concentration was 20 minutes followed by rinsing with 1X PBS buffer (pH 7.4).

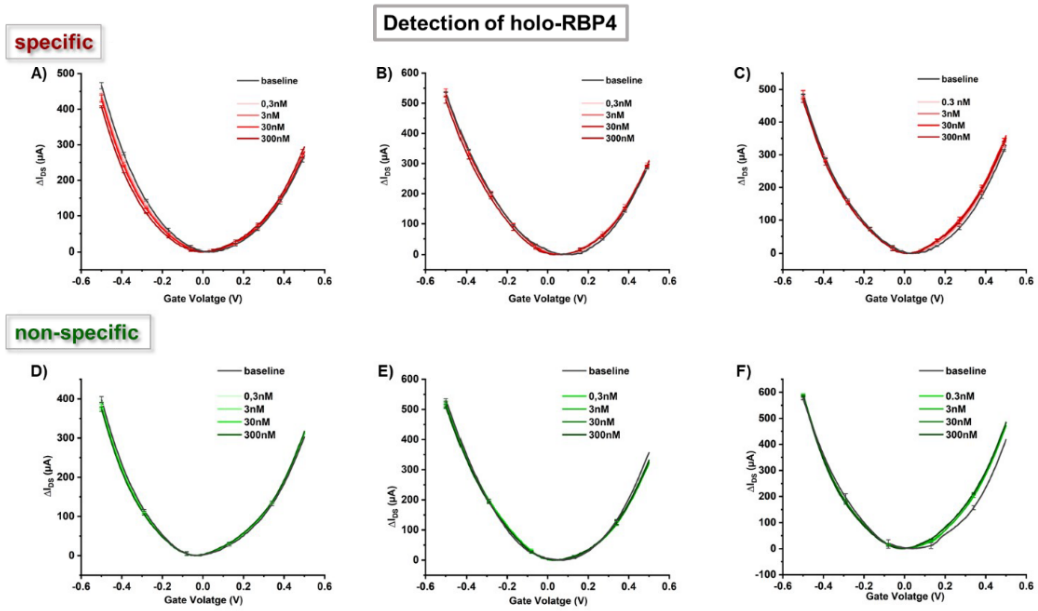

Supplementary Figure S3. I_DV_G characterization of sensing devices obtained by sweeping the gate voltage from -0.5V to 0.5V. A, B and C show 3 specific interactions between holo-RBP4 and the corresponding aptamer library immobilized on the channel. D, E and F show the apo-RBP4 interaction with the same aptamer library that should have no affinity for apo-RBP4. Conditions and parameters were identical in each experiment. Each individual curve is an average of three measurements. Error bars

indicate the standard deviation. Incubation time for each concentration was 20 minutes followed by rinsing with 1X PBS buffer (pH 7.4).

6

Supplementary Figure S4. Real-time sensing of RBP4 on gFET-devices recording I_{DS} at a gate voltage of 400 mV. A) Titration with holo-RBP4 (control), B) titration with apo-RBP4 in real time. C) Titration with apo-RBP4 (control) and D) titration with holo-RBP4.

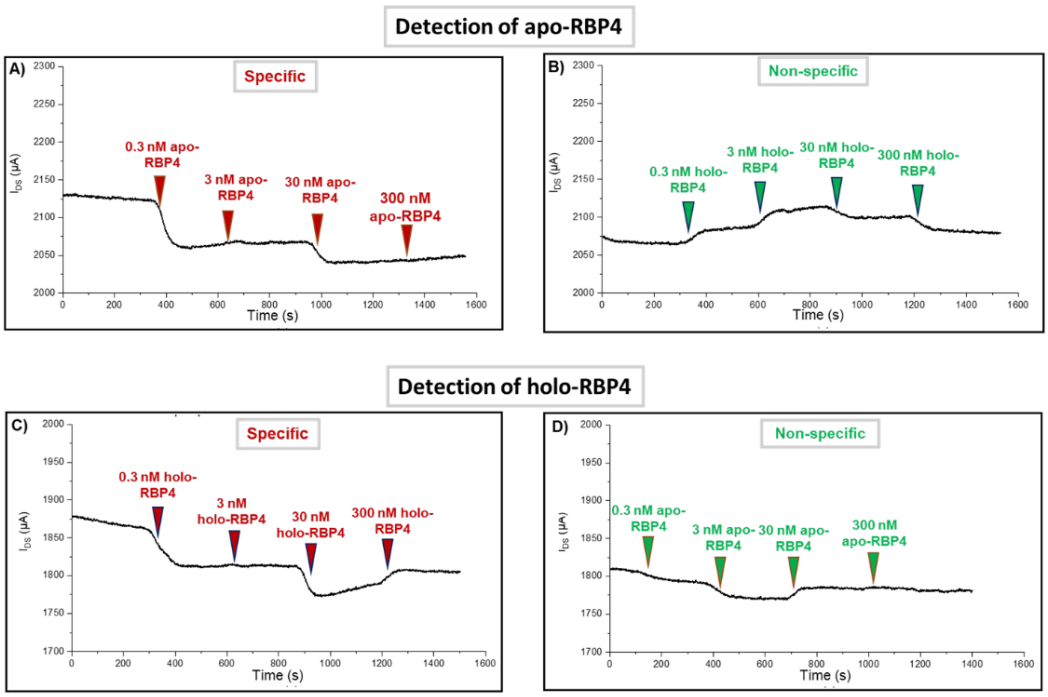

7

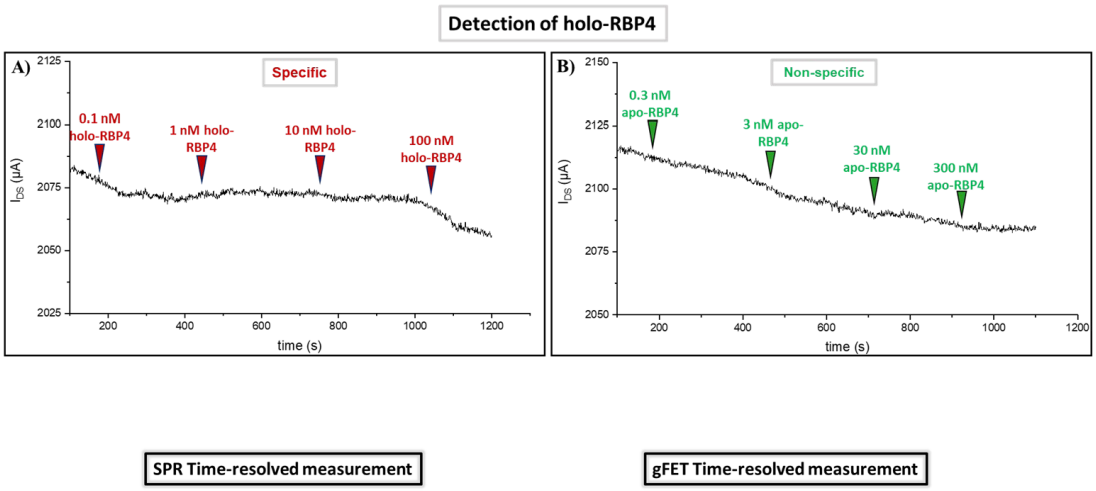

Supplementary Figure S5. It was possible to detect 100 pM holo-RBP4 with some devices, but further optimization is required to reliably reach this sensitivity. A) specific detection of holo-RBP4, B), non-specific interactions with apo-RBP4

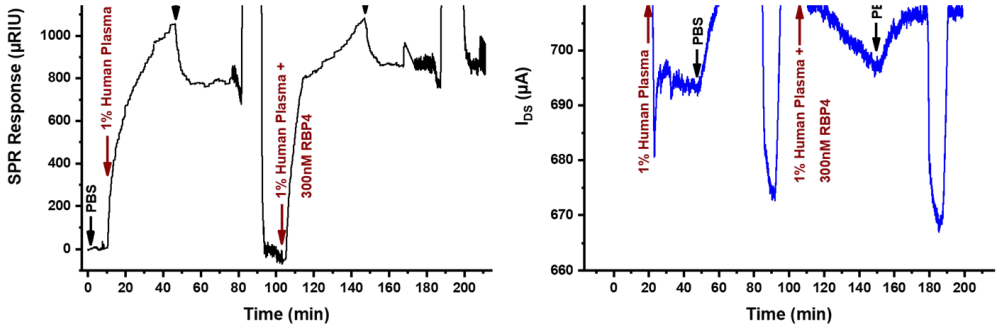

Supplementary Figure S6. Real-time kinetic measurement of holo RBP4 specific aptamer library fuctionalisied surface. A and B are the time resolved SPR and gFET read-out, respectively upon addition of 1% HBP and 1% HBP spiked with 300 nM holo-RBP4.

Passivation against non-specific interactions was tested with human blood plasma (HBP). Figure S7 shows SPR and gFET measurements with 1% human plasma and 300nM RBP4 spiked 1% human plasma to demonstrate that the presence of blood plasma does not prevent RBP4 binding to the sensor surface. For SPR measurements, a glass slide coated with 2 nm chromium and 50 nm gold was functionalised with the holo-aptamer library *via* amine coupling. As shown in Figure 6A, 1% human plasma resulted in mass binding to the surface in the SPR experiment and a decrease in I_{DS} on the gFET, but in both cases the signal returned to baseline after regeneration with 2M NaCl solution. Upon addition of 1% HBP spiked with 300 nM RBP4, the signal did not return to baseline after regeneration which indicates that in the presence of HBP, RBP4 still preferentially binds to the aptamer library.

References

1 U. K. Laemmli, 1970, **227**, 680–685.

2 T. T. Y. Wang, K. C. Lewis and J. M. Phang, *Gene*, 1993, **133**, 291–294.

3 R. Stoltenburg, C. Reinemann and B. Strehlitz, *Anal. Bioanal. Chem.*, 2005, **383**, 83–91.

4 R. Williams, S. G. Peisajovich, O. J. Miller, S. Magdassi, D. S. Tawfik and A. D. Griffiths, 2006, **3**, 545–550.

5 C. Reiner-Rozman, R. Hasler, J. Andersson, T. Rodrigues, A. Bozdogan, J. Bintinger and P. Aspermair, *Micro Nano Lett.*, , DOI:https://doi.org/10.1049/mna2.12070.

8

Author Contributions

Conceptualization, F. Rosenau; methodology, A.-K. Kissmann, J. Andersson; validation, A.-K. Kissmann, J. Andersson and A. Bozdogan; formal analysis, A.-K. Kissmann, J. Andersson, H. F. Raber, M. Krämer, H. Xing, D. H. Kubiczek. P. Aspermair, A. Bozdogan; investigation, A.-K. Kissmann, J. Andersson, A. Bozdogan, V. Amann, M. H. F. Raber, M. Krämer, H. Xing, D. H. Kubiczek. P. Aspermair,; resources, F. Rosenau and W. Knoll; data curation, A.-K. Kissmann, J. Andersson, A. Bozdogan; writing—original draft preparation, A.-K. Kissmann, J. Andersson. F. Rosenau; writing—review and editing, A.-K. Kissmann, J. Andersson, A. Bozdogan, V. Amann, F. Rosenau, W. Knoll; visualization, A.-K. Kissmann, J. Andersson and A. Bozdogan; project administration, F. Rosenau; funding acquisition, F. Rosenau and W. Knoll. All authors have read and agreed to the published version of the manuscript.

A.-K. Kissmann, J. Andersson and A. Bozdogan contributed equally.

Funding Sources

Jakob Andersson was supported by the project Ultra-robust_Lipid_Membrane-based_Nanopore_Sensors (project number LSC19-026) funded by the Gesellschaft für Forschungsförderung Niederösterreich m.b.H. This work was supported by the in the framework of “Bioinspired Material Synthesis”, the Ministry of Science, Research and Arts of the state of Baden-Württemberg (MWK; Förderkennzeichen: 7533-10-5-186A and 7533-10-5-190) in the framework of the Ph.D. program: pharmaceutical biotechnology, the Federal Ministry of Education and Research (BMBF), Biotechnologie 2020+ Basistechnologien: Projekt SeleKomM), the European Union project “Horizon 2020” (No. 686271) in the framework “AD-gut”. We also acknowledge the support by the Baden-Württemberg Stiftung in the project Nano-Mem-To-Tech (BiofMO_005).

7 Summary and Outlook

In recent years, biosensors have emerged as a powerful tool for clinical diagnostics due to their sensitivity, specificity, and ease of use. The studies discussed here present significant advances in the development of biosensors for clinical diagnostics, addressing various aspects of biosensor development, including the deposition protocol for rGO on silica-based substrates, the use of monoclonal antibodies for immunoassays, the employment of polyclonal aptamer libraries, and the selection of detection concepts for clinical applications.

The first study presents an optimized deposition protocol for rGO on silica-based substrates through spin coating with a 214 µg/mL GO solution at 1800 rpm. Developed after examining surface morphology and considering the effects of graphitic structures and intercalation, this protocol significantly improves the reproducibility and stability of electronic devices. When tested for stability regarding baseline drift, these devices demonstrated superior performance compared to drop-casted FETs using the same materials. This optimized deposition protocol provides a guideline for the scientific community, facilitating easier handling and fabrication of GO- or rGO-based sensing devices, particularly biosensors or electronic circuit switches, which can also be fabricated on flexible substrates.

The second study centers on the development of a troponin cTnI immunoassay using a single monoclonal antibody and surface plasmon field-enhanced spectroscopy (SPFS) detection. While the regular SPR biosensor principle did not offer sufficient sensitivity for cTnI analysis at clinically relevant concentrations, the study found that operating the same instrument in SPFS mode significantly improved sensitivity through an inhibition-competitive immunoassay. Crucial to this assay format is the careful selection of cTnI epitope and respective monoclonal antibody based on experimental trials and theoretical modeling. The resulting assay achieved a limit of detection (LoD) of 19 pM within a 45-minute detection time, providing a reliable diagnostic tool for detecting cTnI at clinically relevant concentrations.

The third study examines the use of cTnI as a reference system extensively utilized by biosensor developers to calibrate a broad range of transducer concepts and experimental setups. Although the range of LoD values reported in the literature spans nine orders of magnitude, many papers are only of historical value, as today's cut-off requirements for

clinical applications are at the level of 26 pg/mL, ensuring the monitoring of even healthy patients. Therefore, practitioners seeking an effective detection concept for cTnI must consider other factors, such as ease of operation, test kit robustness, and cost. As a result, it is expected that new proposals and reports on improved detection concepts targeting these factors will continue to emerge in the foreseeable future.

Lastly, the fourth study highlights the use of focused polyclonal aptamer libraries as a promising strategy in diagnostics and sensor technology. Larger sequence spaces enable a diverse and specialized range of binding aptamers, allowing for multiple target recognition and generating enhanced versatility and improved performance in sensing and quantification of target molecules. The wide biotechnological availability of polyclonal aptamer libraries contributes to the rapid, cost-effective, and straightforward development of novel, highly specific electronic sensors for use as powerful tools in clinical diagnostics. By functionalizing the channel of an rGO-FET device, the study successfully discriminated between RBP4 isoforms at physiologically relevant concentrations between 0.3 and 30 nM. The findings suggest that these devices may pave the way for developing biosensors that enable rapid and reliable measurement of RBP4 isoform concentrations as a novel diagnostic marker.

Taken together, these studies represent significant contributions to the development of novel, sensitive, and cost-effective biosensors for clinical diagnostics. The optimized deposition protocol for rGO on silica-based substrates, the use of monoclonal antibodies and SPFS detection for troponin cTnI immunoassays, and the use of focused polyclonal aptamer libraries demonstrate the potential for improving the sensitivity and specificity of biosensors. Furthermore, the selection of appropriate detection concepts for clinical applications, such as considering factors beyond LoD, highlights the importance of considering practical aspects when developing biosensors for clinical use. In conclusion, these studies offer promising avenues for further research and development in the field of biosensors for clinical diagnostics, ultimately contributing to improved patient care and outcomes.

References

1. S. Neethirajan, The role of sensors, big data and machine learning in modern animal farming. *Sens. Bio-Sens. Res.* **29**, 100367 (2020).

2. M. Javaid, A. Haleem, S. Rab, R. P. Singh, R. Suman, Sensors for daily life: A review. *Sens. Int.* **2**, 100121 (2021).

3. P. R. N. Childs, "6 - Rolling element bearings" in *Mechanical Design Engineering Handbook (Second Edition)*, P. R. N. Childs, Ed. (Butterworth-Heinemann, Second Edition., 2019; https://www.sciencedirect.com/science/article/pii/B9780081023679000068), pp. 231–294.

4. S. Bagno, Ultrasonic motion detector. *Issued Aug*. **7** (1958).

5. R. Narayanaswamy, O. S. Wolfbeis, *Optical sensors: industrial, environmental and diagnostic applications* (Springer, Berlin, 2004), vol. 1.

6. H. Huang, V. Agafonov, H. Yu, Molecular Electric Transducers as Motion Sensors: A Review. *Sensors*. **13**, 4581–4597 (2013).

7. T. Hübert, L. Boon-Brett, G. Black, Hydrogen sensors – A review. *Sens. Actuators B Chem.* **157**, 329–352 (2011).

8. S. Paprocki, M. Qassem, P. A. Kyriacou, Review of Ethanol Intoxication Sensing Technologies and Techniques. *Sensors*. **22** (2022), doi:10.3390/s22186819.

9. A. Galli, R. J. H. Montree, S. Que, E. Peri, R. Vullings, An Overview of the Sensors for Heart Rate Monitoring Used in Extramural Applications. **22** (2022), p. 4035.

10. J. Yick, B. Mukherjee, D. Ghosal, Wireless sensor network survey. *Comput. Netw.* **52**, 2292–2330 (2008).

11. P. Mehrotra, Biosensors and their applications – A review. *J. Oral Biol. Craniofacial Res.* **6, (2**, 153–159 (2016).

12. N. Bhalla, P. Jolly, N. Formisano, P. Estrela, Introduction to biosensors. *Essays Biochem*. **60**, 1–8 (2016).

13. J. Dostálek, C. J. Huang, W. Knoll, Surface plasmon resonance-based biosensors, 17.

14. H. Chen, J. Li, Q. Zhang, Graphene-based biosensors: progress and prospects. *Biosens. Bioelectron.* **173**, 112803 (2021).

15. J. Wang, Electrochemical biosensors: towards point-of-care cancer diagnostics. *Biosens. Bioelectron.* **21**, 1887–1892 (2008).

16. H. Altug, S.-H. Oh, S. A. Maier, J. Homola, Advances and applications of nanophotonic biosensors. *Nat. Nanotechnol.* **17**, 5–16 (2022).

17. N. Bhalla, *Opportunities and challenges for biosensors and nanoscale analytical tools for pandemics: COVID-19* (ACS Nano, 2020), vol. 14.

18. J. J. BelBruno, D. A. Spivak, *Biosensors: from construction to application* (Springer, 2011).

19. D. Kotlarek, F. Curti, M. Vorobii, R. Corradini, M. Careri, W. Knoll, C. Rodriguez-Emmenegger, J. Dostálek, Surface plasmon resonance-based aptasensor for direct monitoring of thrombin in a minimally processed human blood. *Sens. Actuators B Chem.* **320**, 128380 (2020).

20. L. Chen, Y. Bao, J. Denstedt, J. Zhang, Nanostructured bioluminescent sensor for rapidly detecting thrombin. *Biosens. Bioelectron.* **77**, 83-89, (2016).

21. R. Hasler, C. Reiner-Rozman, S. Fossati, P. Aspermair, J. Dostalek, S. Lee, M. Ibáñez, J. Bintinger, W. Knoll, Field-Effect Transistor with a Plasmonic Fiber Optic Gate Electrode as a Multivariable Biosensor Device. *ACS Sens.* **7**, 504–512 (2022).

22. Y. Zhang, Q. Wu, M. Sun, J. Zhang, S. Mo, J. Wang, X. Wei, J. Bai, Magneticassisted aptamer-based fluorescent assay for allergen detection in food matrix, Sens. *Actuators B Chem*. **263**, 43-49, (2018).

23. J. P. Chambers, B. P. Arulanandam, L. L. Matta, A. Weis, J. J. Valdes, Biosensor recognition elements. *Curr. Issues Mol. Biol.* **10**, 1-2 , 1–12 (2008).

24. E. G. Griffin, J. M. Nelson, THE INFLUENCE OF CERTAIN SUBSTANCES ON THE ACTIVITY OF INVERTASE. *J. Am. Chem. Soc.* **38**, 722–730 (1916).

25. J. M. Nelson, E. G. Griffin, ADSORPTION OF INVERTASE. *J. Am. Chem. Soc.* **38**, 1109–1115 (1916).

26. L. C. Clark, R. Wolf, D. Granger, Z. Taylor, Continuous Recording of Blood Oxygen Tensions by Polarography. *J. Appl. Physiol.* **6**, 189–193 (1953).

27. Varnakavi. Naresh, N. Lee, A Review on Biosensors and Recent Development of Nanostructured Materials-Enabled Biosensors. *Sensors*. **21** (2021), doi:10.3390/s21041109.

28. P. Damborský, J. Švitel, J. Katrlík, Optical biosensors. *Essays Biochem.* **60, (1**, 91–100 (2016).

29. X. Fan, I. M. White, S. I. Shopova, H. Zhu, J. D. Suter, Y. Sun, Sensitive optical biosensors for unlabeled targets: a review. *Anal. Chim. Acta*. **620**, 8-26, (2008).

30. D.-K. Kim, K. Kerman, H. M. Hiep, M. Saito, S. Yamamura, Y. Takamura, Y.-S. Kwon, E. Tamiya, Label-free optical detection of aptamer–protein interactions using gold-capped oxide nanostructures. *Anal. Biochem.* **379**, 1-7, (2008).

31. K. Sergelen, B. Liedberg, W. Knoll, J. Dostálek, A surface plasmon field-enhanced fluorescence reversible split aptamer biosensor. *The Analyst*. **142**, 2995–3001 (2017).

32. N. T. Kalyani, H. Swart, S. J. Dhoble, "Chapter 1 - Luminescence: Basic Principles and Applications" in *Principles and Applications of Organic Light Emitting Diodes (OLEDs)*, N. T. Kalyani, H. Swart, S. J. Dhoble, Eds. (Woodhead Publishing, 2017; https://www.sciencedirect.com/science/article/pii/B9780081012130000011), pp. 1–37.

33. J. X. J. Zhang, K. Hoshino, "Chapter 5 - Optical Transducers: Optical Molecular Sensors and Optical Spectroscopy" in *Molecular Sensors and Nanodevices*, J. X. J. Zhang, K. Hoshino, Eds. (William Andrew Publishing, Oxford, 2014; https://www.sciencedirect.com/science/article/pii/B9781455776313000053), pp. 233–320.

34. A. Bozdogan, S. Hageneder, J. Dostalek, "Chapter Nineteen - Plasmonic biosensors relying on biomolecular conformational changes: Case of odorant binding proteins" in *Odorant Binding and*

Chemosensory Proteins, P. Pelosi, W. Knoll, Eds. (Academic Press, 2020; https://www.sciencedirect.com/science/article/pii/S007668792030207X), vol. 642 of *Methods in Enzymology*, pp. 469–493.

35. S. Hageneder, S. Fossati, N.-G. Ferrer, B. Güngörmez, S. K. Auer, J. Dostalek, Multi-diffractive grating for surface plasmon biosensors with direct back-side excitation. *Opt Express*. **28**, 39770–39780 (2020).

36. J. L. Bigman, K. A. Reinhardt, "Chapter 11 - Monitoring of Chemicals and Water" in *Handbook of Silicon Wafer Cleaning Technology (Third Edition)*, K. A. Reinhardt, W. Kern, Eds. (William Andrew Publishing, 2018; https://www.sciencedirect.com/science/article/pii/B9780323510844000113), pp. 619–657.

37. M. Hussain, J. Zou, H. Zhang, R. Zhang, Z. Chen, Y. Tang, Recent Progress in Spectroscopic Methods for the Detection of Foodborne Pathogenic Bacteria. *Biosensors*. **12** (2022), doi:10.3390/bios12100869.

38. J. Homola, S. S. Yee, G. Gauglitz, Surface plasmon resonance sensors: review. *Sens. Actuators B Chem.* **54, (1**, 3–15 (1999).

39. E. Kretschmann, H., Reather Radiative decay of nonradiative surface plasmon excited by light. *Z.Naturf.* **23A**, 2135–2136 (1968).

40. E. Kretschmann, Die Bestimmung optischer Konstanten von Metallen durch Anregung von Oberflachenplasmaschwingugnen. *Z Phys*. **241**, 313–324 (1971).

41. P. Aspermair, U. Ramach, C. Reiner-Rozman, S. Fossati, B. Lechner, S. E. Moya, O. Azzaroni, J. Dostalek, S. Szunerits, W. Knoll, J. Bintinger, Dual Monitoring of Surface Reactions in Real Time by Combined Surface-Plasmon Resonance and Field-Effect Transistor Interrogation. *J Am Chem Soc*. **142**, 11709–11716 (2020).

42. B. Liedberg, C. Nylander, I. Lunström, Surface plasmon resonance for gas detection and biosensing. *Sens. Actuators*. **4**, 299–304 (1983).

43. I. Pockrand, J. D. Swalen, J. G. Gordon, Surface plasmon spectroscopy of organic monolayer assemblies (1978).

44. K. A. Peterlinz, R., Georgiadis Two-color approach for determination of thickness and dielectric constant of thin films using surface plasmon resonance. *Opt.Commun*. **130**, 260–266 (1996).

45. B. Liedberg, I. Lundstrom, E., Stenberg Principles of biosensing with an extended coupling matrix and surface plasmon resonance. *Sens. Actuators B*. **11**, 63–72 (1993).

46. L. Zhang, D., Uttamchandani Optical chemical sensing employing surface plasmon resonance. *Electron Lett*. **23**, 1469–1470 (1988).

47. C. Striebel, A. Brecht, G., Gauglitz Characterization of biomembranes by spectral elipsometry, surface plasmon resonance and interferometry with regard to biosensor application. *Biosens.Bioelectron*. **9**, 139–146 (1994).

48. R. B. M. Schasfoort, "Introduction to Surface Plasmon Resonance" in *Handbook of Surface Plasmon Resonance*, R. B. M. Schasfoort, Ed. (The Royal Society of Chemistry, 2017; https://doi.org/10.1039/9781788010283-00001), p. 0.

49. J. Dostalek, C. J. Huang, W., Weinheim, Ed., Knoll, in Chapter 1.3: Surface plasmon resonance-based biosensor in Advanced surface design for biomaterial and life science applications (Wiley-VCH (2009).

50. P. A. S. P. R. Merwe, (2003).

51. K. Nagata, H., Handa Rela-Time Analysis of Biomelecular Interactions (2000).

52. J. Homola, Surface Plasmon Resonance Sensors for Detection of Chemical and Biological Species. *Chem. Rev.* **108**, 462–493 (2008).

53. D. Kotlarek, M. Vorobii, W. Ogieglo, W. Knoll, C. Rodriguez-Emmenegger, J. Dostálek, Compact Grating-Coupled Biosensor for the Analysis of Thrombin. *ACS Sens*. **4**, 2109–16 (2019).

54. M. Beseničar, P. Maček, J. H. Lakey, G. Anderluh, Surface plasmon resonance in protein–membrane interactions. *Chem. Phys. Lipids*. **141**, 169–178 (2006).

55. P. R. Schuckannu, Biophys. *Biomol Struct*, 541–566 (1997).

56. P. W. Atkins, Physical Chemistry (1998), pp. 858–859.

57. A. K. Geim, K., Novoselov "The Rise of Graphene. *Nat. Mater.* **6**, 183-191, (2007).

58. P. Shapira, A. Gök, F. Salehi, Graphene enterprise: Mapping innovation and business development in a strategic emerging technology. *J. Nanoparticle Res.* **18** (2016), doi:10.1007/s11051-016-3572-1.

59. Y.-M. Lin, A. Valdes-Garcia, S.-J. Han, D. B. Farmer, I. Meric, Y. Sun, Y. Wu, C. Dimitrakopoulos, A. Grill, P. Avouris, K. A. Jenkins, Wafer-scale graphene integrated circuit. *Science*. **332**, 1294-1297, (2011).

60. A. A. Balandin, S. Ghosh, W. Bao, I. Calizo, D. Teweldebrhan, F. Miao, C. N, Lau "Superior thermal conductivity of single-layer graphene. *Nano Lett.* **8**, 902-907, (2008).

61. L. Schubnikow, W. J. Haas, "Magnetische Widerstandsvergrösserung in Einkristallen von Wismut bei tiefen Temperaturen" [Magnetic resistance increase in single crystals of bismuth at low temperatures" in *Proceedings of the Royal Netherlands Academy of Arts and Science (in German* (1930), vol. 33, pp. 130–133.

62. K. I. Bolotin, F. Ghahari, M. D. Shulman, H. L. Stormer, P. Kim, Observation of the fractional quantum hall effect in graphene. *Nature*. **462**, 196-199, (2009).

63. C. Berger, Z. Song, T. Li, X. Li, A. Y. Ogbazghi, R. Feng, Z. Dai, A. N. Marchenkov, E. H. Conrad, P. N. First, W. A. Heer, *J. Phys. Chem. B*, in press.

64. L. M. Viculis, J. J. Mack, R. B. Kaner, A chemical route to carbon nanoscrolls. *Science*. **299**, 1361–1361 (2003).

65. S. Radic, N. K. Geitner, R. Podila, A. Kakinen, P. Y. Chen, P. C. Ke, F. Ding, Competitive Binding of Natural Amphiphiles with Graphene Derivatives. *Sci. Rep.* **3** (2013), doi:10.1038/srep02273.

66. A. N. Obraztsov, CHEMICAL VAPOUR DEPOSITION Making graphene on a large scale. *Nat. Nanotechnol.* **4**, 212–213 (2009).

67. S. F. Pei, H. M. Cheng, The reduction of graphene oxide. *Carbon*. **50**, 3210–3228 (2012).

68. J.-H. Chen, C. Jang, S. Xiao, M. F. Ishigami, M. S, Intrinsic and extrinsic performance limits of graphene devices on SiO2. *Nat. Nanotech*. **3**, 206–209 (2008).

69. F. Xia, D. B. Farmer, Y.-M. Lin, P. Avouris, Graphene Feld-efect transistors with high on/off current ratio and large transport band gap at room temperature.". *Nano Lett.* **10**, 7158, (2010).

70. J. Wang, D. Ye, Q. Meng, C. Di, D. Zhu, Advances in Organic Transistor-Based Biosensors. *Adv Mater Technol*. **5**, 2000218 (2020).

71. K. Maehashi, Y. Sofue, S. Okamoto, Y. Ohno, K. Inoue, K. Matsumoto, Selective ion sensors based on ionophore-modified graphene field-effect transistors". *Sens Actuators B Chem.* **187**, 45-49, (2013).

72. E. D. Minot, A. M. Janssens, I. Heller, H. A. Heering, C. Dekker, S. G. Lemay, Carbon nanotube biosensors: The critical role of the reference electrode". *Appl Phys Lett*. **91, 9**, 093507, (2007).

73. C. Yu, X. Chang, J. Liu, L. Ding, J. Peng, Y. Fang, Creation of Reduced Graphene Oxide Based Field Effect Transistors and Their Utilization in the Detection and Discrimination of Nucleoside Triphosphates". *ACS Appl Mater Interfaces*. **7**, 10718-10726, (2015).

74. M. A. Gebbie, A. M. Smith, H. A. Dobbs, A. Lee, G. G. Warr, X. Banquy, M. Valtiner, M. W. Rutland, J. N. Israelachvili, S. Perkin, R. Atkin, Long range electrostatic forces in ionic liquids". *Chem Commun*. **53**, 1214-1224, (2017).

75. F. Chen, Q. Qing, J. Xia, N. Tao, Graphene Field-Effect Transistors: Electrochemical Gating, Interfacial Capacitance and Biosensing Applications". *Chem-Asian J*. **5**, 2144-2153, (2010).

76. R. Zheng, B. W. Park, D. S. Kim, B. D. Cameron, Development of a highly specific amine-terminated aptamer functionalized surface plasmon resonance biosensor for blood protein detection. *Biomed. Opt. Express*. **2**, 2731-2740, (2011).

77. X. Zhu, T. G. Mason, Separating Nanoparticles by Surface Charge Group Using pH-Controlled Passivated Gel Electrophoresis. *Soft Mater*. **14**, 204–209 (2016).

78. L. Zuccaro, C. Tesauro, T. Kurkina, P. Fiorani, H. K. Yu, B. R. Knudsen, K. Kern, A. Desideri, K. Balasubramanian, Real-Time Label-Free Direct Electronic Monitoring of Topoisomerase Enzyme Binding Kinetics on Graphene". *ACS Nano*. **9**, 11166-11176, (2015).

79. Z. Wang, K. Yi, Q. Lin, L. Yang, X. Chen, H. Chen, Y. Liu, D. Wei, Free radical sensors based on inner-cutting graphene field-effect transistors". *Nat Commun*. **10**, 1544, (2019).

80. S. Farid, X. Meshik, M. Choi, S. Mukherjee, Y. Lan, D. Parikh, S. Poduri, U. Baterdene, C. E. Huang, Y. Y. Wang, P. Burke, M. Dutta, M. A. Stroscio, Detection of Interferon gamma using graphene and aptamer based FET-like electrochemical biosensor". *Biosens Bioelectron*. **71**, 294-299, (2015).

81. S. K. Sia, G. M. Whitesides, Microfluidic devices fabricated in poly(dimethylsiloxane) for biological studies". *Electrophoresis*. **24**, 3563-3576, (2003).

82. D. Qin, Y. Xia, G. M. Whitesides, Soft lithography for micro- and nanoscale patterning". *Nat Protoc*. **5**, 491-502, (2010).

83. R. L. Calabro, D.-S. Yang, D. Y. Kim, Liquid-phase laser ablation synthesis of graphene quantum dots from carbon nano-onions: Comparison with chemical oxidation. *J Colloid Interf Sci*. **527**, 132–140 (2018).

84. C. Reiner-Rozman, R. Hasler, J. Andersson, T. Rodrigues, A. Bozdogan, J. Bintinger, P. Aspermair, *Micro Amp Nano Lett.*, in press, doi:10.1049/mna2.12070.

85. B. G. Streerman, *Solid State Electronic Devices* (Prentice Hall, 4th edn., 1997).

86. Y. Zhang, J. Tang, Graphene-based biosensors for detection of biomolecules: a review. *J. Anal. Methods Chem.*, 4036167 (2019).

87. J. G. Champlain, A first principles theoretical examination of graphene- based field effect transistors". *J Appl Phys*. **109**, 084515, (2011).

88. W. Fu, L. Jiang, E. P. v Geest, L. M. C. Lima, G. F. Schneider, Sensing at the surface of graphene field-effect transistors". *Adv Mater*. **29, 1603610** (2017).

89. J. S. Moon, M. Antcliffe, H. C. Seo, D. Curtis, S. Lin, A. Schmitz, I. Milosavljevic, A. A. Kiselev, R. S. Ross, D. K. Gaskill, P. M. Campbell, R. C. Fitch, K. M. Lee, P. Asbeck, Ultra-low resistance ohmic contacts in graphene field effect transistors". *Appl Phys Lett*. **100, 203512** (2012).

90. N. Vandecasteele, A. Barreiro, M. Lazzeri, A. Bachtold, F. Mauri, Current-voltage characteristics of graphene devices: Interplay between Zener-Klein tunneling and defects". *Phys Rev B Condens Matter Mater Phys*. **82**, 045416, (2010).

91. S. Mao, G. Lu, K. Yu, Z. Bo, J. Chen, Specific protein detection using thermally reduced graphene oxide sheet decorated with gold nanoparticle- antibody conjugates". *Adv Mater*. **22**, 3521-3526, (2010).

92. D. Kwong Hong Tsang, T. J. Lieberthal, C. Watts, I. E. Dunlop, S. Ramadan, A. E. Rio Hernandez, N. Klein, Chemically Functionalised Graphene FET Biosensor for the Label-free Sensing of Exosomes". *Sci Rep*. **9**, 1-10, (2019).

93. C. Kotlowski, P. Aspermair, H. U. Khan, C. Reiner-Rozman, J. Breu, S. Szunerits, J.-J. Kim, Z. Bao, C. Kleber, P. Pelosi, W. Knoll, Electronic biosensing with flexible organic transistor devices. *Flex Print Electron*. **3**, 034003 (2018).

94. H. G. Sudibya, Q. He, H. Zhang, P. Chen, Electrical Detection of Metal Ions Using Field-Effect Transistors Based on Micropatterned Reduced Graphene Oxide Films". *ACS Nano*. **5**, 1990-1994, (2011).

95. G. Saltzgaber, P. M. Wojcik, T. Sharf, M. R. Leyden, J. L. Wardini, C. A. Heist, A. A. Adenuga, V. T. Remcho, E. D. Minot, Scalable graphene field-effect sensors for specific protein detection". *Nanotechnology*. **24, 355502** (2013).

96. R. Robinson, R. Stokes, *Electrolyte Solutions* (Dover Publications, Incorporated, Second Revised., 2012), *ser. Dover Books on Chemistry Series*.

97. A. Stogryn, Equations for calculating the dielectric constant of saline water (correspondence. *Microw. Theory Tech. IEEE Trans. On*. **19**, 733-736, (1971).

98. D. Gadani, V. Rana, S. Bhatnagar, A. Prajapati, A. Vyas, Effect of salinity on the dielectric properties of water. *Indian J. Pure Appl. Phys.* **50**, 405-410, (2012).

99. E. Stern, R. Wagner, F. J. Sigworth, R. Breaker, T. M. Fahmy, M. A. Reed, Importance of the Debye Screening Length on Nanowire Field Effect Transistor Sensors. *Nano Lett.* **7**, 3405-3409, (2007).

100. D. N. Petsev, F. van Swol, L. J. D. Frink, *Molecular Theory of Electric Double Layers* (IOP Publishing, 2021; https://dx.doi.org/10.1088/978-0-7503-2276-8), *2053-2563*.

101. G. Sposito, "Gouy-Chapman Theory" in *Encyclopedia of Geochemistry: A Comprehensive Reference Source on the Chemistry of the Earth*, W. M. White, Ed. (Springer International Publishing, Cham, 2018; https://doi.org/10.1007/978-3-319-39312-4_50), pp. 623–628.

102. M. A. Brown, G. V. Bossa, S. May, Emergence of a Stern Layer from the Incorporation of Hydration Interactions into the Gouy–Chapman Model of the Electrical Double Layer. *Langmuir*. **31**, 11477–11483 (2015).

103. D. C. Grahame, The electrical double layer and the theory of electrocapillar- ity. *Chem. Rev.* **41**, 441-501, (1947).

104. G. Sauerbrey, Verwendung von Schwingquarzen zur Wägung dünner Schichten und zur Mikrowägung. *Z. Für Phys.* **155**, 206–222 (1959).

105. M. Piliarik, J. Homola, Surface plasmon resonance (SPR) sensors: approaching their limits? *Opt. Quantum Electron.* **41**, 321–341 (2009).

106. G. T. Hermanson, *Bioconjugate techniques* (Academic Press, 2013).

107. I. Lundström, Antibody engineering-current achievements and future prospects. *Drug Discov. Today*. **7**, 552–558 (2002).

108. N. M. Green, Avidin and streptavidin. *Methods Enzymol.* **34**, 51–65 (1975).

109. K. E. Sapsford, K. M. Tyner, B. J. Dair, Advances in surface plasmon resonance biosensor analysis. *Curr. Opin. Biotechnol.* **17**, 400–407 (2006).

110. R. Wilson, A. P. Turner, Glucose oxidase: an ideal enzyme. *Biosens. Bioelectron.* **7**, 165–185 (1992).

111. G. Kohler, C. Milstein, Continuous cultures of fused cells secreting antibody of predefined specificity. *Nature*. **256**, 495–497 (1975).

112. K. H. Lee, J. H. Oh, Recent advances in graphene-based biosensors. *Sensors*. **18**, 3219 (2018).

113. A. Roda, M. Mirasoli, E. Michelini, Immunochemical strategies for environmental analysis and monitoring: a review. *Talanta*. **69**, 288–301 (2006).

114. R. Burger, H. Pick, Immunoassays in pharmaceutical analysis. *TrAC Trends Anal. Chem.* **101**, 150–158 (2018).

115. K. Mosbach, Molecular imprinting. *Top. Curr. Chem.* **325**, 1–21 (2012).

116. M. Giannoglou, E. Benito-Peña, C. Pérez-Conde, Nucleic acid aptamers: applications in biomedicine and biosensing. *Sensors*. **18**, 1092 (2018).

117. C. Lu, H. Yang, C. L. Zhu, X. Chen, G. N. Chen, A graphene platform for sensing biomolecules. *Angew. Chem. Int. Ed.* **48**, 4785–4787 (2009).

118. J. Wu, B. C. Yin, L. Guo, A. L. Liu, Recent advances in graphene-based biosensors. *Anal. Bioanal. Chem.* **406**, 6885–6902 (2014).

119. S. Seo, M. Kim, H. Lee, Y. Kim, Graphene-based field-effect transistor biosensors: a review. *Appl. Sci.* **8**, 229 (2018).

120. Y. Chen, H. Qi, B. Zhang, Z. Cheng, H. Wang, Graphene-based biosensors: from in vitro to in vivo. *Micromachines*. **9**, 324 (2018).

121. M. Bariya, H. Y. Y. Nyein, A. Javey, G. A. Weiss, Recent advances in sensing technology for detection of biomolecules, cells, and tissues. *Adv. Drug Deliv. Rev.* **125**, 78–93 (2018).

122. W. J. Cho, Y. T. Kim, C. Chung, Y. K. Kim, Protein immobilization strategies for protein biochips. *J. Appl. Biol. Chem.* **61**, 87–99 (2018).

123. L. Wu, X. Chen, J. Fan, P. Wang, J. Zhang, S. Wang, A highly sensitive and selective graphene field-effect transistor biosensor for detection of DNA oligon (2019).

124. Z. Guo, S. Chakraborty, F. A. Monikh, D.-D. Varsou, A. J. Chetwynd, A. Afantitis, I. Lynch, P. Zhang, Surface Functionalization of Graphene-Based Materials: Biological Behavior, Toxicology, and Safe-By-Design Aspects. *Adv. Biol.* **5**, 2100637 (2021).

125. A. P. Turner, Biosensors: sense and sensibility. *Chem. Soc. Rev.* **42**, 3184–3196 (2013).

126. H. Shi, C. Liu, S. Jiang, V. A. Roy, Y. Wang, Graphene-based sensors for biomedical applications. *J. Mater. Chem. B*. **4**, 3313–3330 (2016).